



TECHNISCHE
UNIVERSITÄT
WIEN
Vienna University of Technology

Diese Dissertation haben begutachtet:

.....

DISSERTATION

**Low Coherence Tissue Interferometry
for the Depth-Resolved Measurement of
Ocular Fundus Pulsations**

ausgeführt zum Zwecke der Erlangung des akademischen Grades eines
Doktors der technischen Wissenschaften

unter der Leitung von

Ao.Univ.Prof. Dipl.-Ing. Dr.techn. Martin Gröschl
Institut für Angewandte Physik (E134)
Technische Universität Wien

und

Ao.Univ.Prof. Dipl.-Ing. Dr.techn. Leopold Schmetterer
Zentrum für Medizinische Physik und Biomedizinische Technik
Medizinische Universität Wien

eingereicht an der Technischen Universität Wien
Fakultät für Physik

von

Dipl.-Ing. Nikolaus Dragostinoff
Matrikelnummer: 9625327
Schellenseegasse 5A/2207
1230 Wien

Wien, im September 2010

Unterschrift

Abstract

In this dissertation a new technique called low coherence tissue interferometry (LCTI) is introduced, which allows for the measurement of ocular fundus pulsations (i.e., distance variations between the anterior surface of the cornea and the ocular fundus) at pre-selected axial positions of the subject's eye. Unlike previously presented systems, which only allow for observation of the strongest reflecting retinal layer, this system enables the measurement of fundus pulsations at a pre-selected ocular layer. For this purpose the sample is illuminated by light of low temporal coherence. The layer is then selected by positioning one mirror of a Michelson interferometer according to the depth of the layer. The device contains a length measurement system based on partial coherence interferometry (PCI) and a line scan CCD camera for recording and online inspection of the fringe system.

In vivo measurements in healthy humans at different angles to the axis of vision were performed during this work and algorithms for the enhancement of the recorded images were developed. In all subjects, fundus pulsations were measurable in various reflective layers at the posterior pole of the eye, especially in the inner limiting membrane and the retinal pigment epithelium. The contrast of the observed interference fringes was evaluated *in vitro* for different positions of the measurement mirror and calculated for various distances from the front surface of the cornea. This enabled, firstly, for determination of the plane of highest contrast, and, secondly, for estimation of the maximum observable fundus pulsation amplitude. Furthermore, usability of a diffractive optical element (DOE) for enhancement of the signal to noise ratio was studied, and fringe contrast and spacing for a system with DOE was calculated. In one subject, comprehensive measurements of the fundus pulsation amplitudes were performed at horizontal angles ranging from -2° temporal to 19° nasal to the axis of vision, resulting in an overview graph of the topographic (lateral and axial) distribution of the fundus pulsation amplitude. Particularly in the surroundings of the optic nerve head, the ability of LCTI to measure fundus pulsations at well-defined axial positions is valuable and can provide new insight into the biomechanical properties of the eye, especially in glaucoma patients. Further applications of the technique developed in this work include assessment of eye elongation during myopia development and blood flow related changes in intraocular volume.

Deutsche Kurzfassung der Dissertation

Im Rahmen dieser Dissertation wurde ein neuartiges Gerät entwickelt, das die tiefenaufgelöste Messung okulärer Funduspulsationen (d.h. durch den Herzrhythmus hervorgerufene Abstandsänderungen zwischen der Vorderseite der Hornhaut und der Netzhaut des Auges) ermöglicht. Die diesem System zugrundeliegende Technik wird als *Kurzkohärenzgewebeinterferometrie (low coherence tissue interferometry, LCTI)* bezeichnet. Während bisher eingesetzte Systeme langkohärente Lichtquellen verwenden und lediglich die Beobachtung der Bewegung der am stärksten reflektierenden Schicht der Netzhaut erlauben, ermöglicht das hier vorgestellte Gerät die Messung von Funduspulsationen an beliebigen, ausgewählten Schichten der Netzhaut des Auges mittels kurzkohärentem Licht.

Um Funduspulsationen an bestimmten, reflektierenden Schichten der Netzhaut messen zu können, ist die Bestimmung der axialen Positionen dieser Schichten erforderlich. Zu diesem Zweck wird eine Längenmessung mittels zweistrahliger partieller Kohärenzinterferometrie (PCI) durchgeführt. Dabei wird Licht geringer zeitlicher Kohärenz in ein Michelson-Interferometer eingeleitet, dessen einer Spiegel fest montiert ist, während der andere Spiegel an einem Schrittmotor angebracht ist. Die beiden das Interferometer verlassenden Strahlen haben eine Wegdifferenz, die dem doppelten der eingestellten Wegdifferenz der beiden Spiegel entspricht. Die Strahlen treffen danach auf das Auge, wobei Reflexionen an der Hornhaut und an verschiedenen Strukturen der Netzhaut auftreten, welche wiederum mittels einer Avalanche Photodiode (APD) gemessen werden. Entspricht der Abstand der Spiegel des Michelson-Interferometers der optischen Distanz zweier Strukturen innerhalb des Auges, tritt eine mit der APD meßbare Intensität auf. Auf diese Weise lassen sich – durch Bewegungen des am Schrittmotor angebrachten Spiegels über eine bestimmte Strecke – die Augenlänge bzw. die Positionen verschiedener Schichten der Netzhaut des Auges bestimmen. Das mit dieser Methode erzeugte Tiefenprofil wird als *optischer A-Scan* bezeichnet. In diesem A-Scan wird eine Stelle, die einer reflektierenden Struktur im Augenhintergrund entspricht, ausgewählt, und der Schrittmotor wird an diese Position gefahren.

Das an der Hornhaut reflektierte Licht hat annähernd die Form einer Kugelwelle, während der durch das optische System des Auges gehende und an der Netzhaut reflektierte Strahl einer ebenen Welle entspricht. Durch Überlagerung dieser beiden Wellenfronten entsteht ein Interferenzmuster aus konzentrischen Kreisen, das in dem hier vorgestellten Gerät auf eine CCD-Zeilenkamera abgebildet wird. Das Signal der Kamera wird mittels eines PCs aufgezeichnet und zur laufenden Beobachtung dargestellt. Durch Zählen der Interferenzringe, die sich durch einen fixen Punkt bewegen, lässt sich der zeitliche Verlauf bzw. die Amplitude der Funduspulsationen bestimmen. Da bei LCTI eine kurzkohärente Lichtquelle verwendet wird, sind die Pulsationen jener Schicht zu sehen, die – wie bereits beschrieben – durch Positionie-

rung des Schrittmotorspiegels ausgewählt wurde. Befindet sich der Spiegel an einer Position, die keiner reflektierenden Struktur entspricht, ist kein Interferenzmuster zu beobachten.

Es wurden während dieser Arbeit *in vivo*-Messungen an gesunden Probanden bei verschiedenen Sichtwinkeln durchgeführt. Bei allen Probanden konnten Funduspulsationen in mehreren Schichten der Netzhaut gemessen werden, insbesondere in der inneren Grenzmembran und im retinalen Pigmentepithel. Weiters wurden Algorithmen zur Verbesserung der Darstellungsqualität der aufgenommenen Interferogramme entwickelt. Der Kontrast des Interferenzmusters wurde für verschiedene Schrittmotorpositionen an einem künstlichen Auge gemessen und in Abhängigkeit von der Entfernung zur Hornhaut berechnet, was einerseits die Bestimmung der Ebene des höchsten Kontrasts ermöglichte und andererseits die Abschätzung der maximal meßbaren Pulsationsamplitude erlaubte. Es wurde die Verwendbarkeit eines diffraktiven optischen Elements (DOE) zur Erhöhung der gemessenen Signalintensität getestet und für ein System mit DOE der Kontrast des Interferenzmusters sowie der Abstand der Interferenzringe berechnet.

An einem Probanden wurde eine umfassende Serie von Pulsationsmessungen bei horizontalen Sichtwinkeln von -2° temporal bis 19° nasal durchgeführt. Dadurch konnte erstmals ein topographischer (axial und lateral aufgelöster) Übersichtsgraph der Funduspulsationen erstellt werden. Speziell in der Umgebung des Sehnervs ist die Fähigkeit von LCTI, Pulsationen an genau definierten Tiefenpositionen zu messen, von Bedeutung und kann neue Einblicke in die Biomechanik des Auges geben, insbesondere bei Glaukompatienten, da es hier zu Veränderungen in den mechanischen Eigenschaften des Augenhintergrundes kommt. Ein anderer Anwendungsbereich ist die tiefenaufgelöste Pulsationsmessung bei Patienten mit Makulaödem, bei denen eine deutlich nicht-parallele Bewegung der einzelnen Schichten der Netzhaut zu erwarten ist. Weitere Anwendungsmöglichkeiten von LCTI liegen im Bereich der Tiermodelle, etwa die Erfassung des Augenlängenwachstums beim Entstehen von Kurzsichtigkeit sowie die Messung von pulsatilen Volumensänderungen des Auges durch Beobachtung der Sclera (Lederhaut).

Acknowledgements

I would like to express my greatest thanks to my supervisor Prof. Leopold Schmetterer from the Center of Medical Physics and Biomedical Engineering at the Medical University of Vienna, who shared his wide knowledge in physics and ophthalmology with me. Without his encouragement and support this work would not have been possible.

My honest gratitude to Prof. Martin Gröschl from the Institute of Applied Physics at the Vienna University of Technology for his support and advice during this work.

A special thank to René Werkmeister for many fruitful discussions on optics, sports and the style of life in Vienna and his assistance with the setup and adjustment of the system.

I also wish to thank Branislav Grajciar, Michael Pircher, Bernhard Baumann and all other members of the institute. It has been a great experience working with all of you.

Furthermore, I would like to acknowledge the contribution of Harald Sattmann from the electronics laboratory, and Christoph Wölfl and Leopold Schachinger from the mechanic workshop.

Finally, I would like to thank my parents Lisa and Georg Dragostinoff and all my family for all their love and support and especially for believing in me.

Contents

1	Introduction	1
1.1	Motivation	1
1.2	Overview of LCTI	2
2	Medical Aspects	5
2.1	Anatomy of the Eye	5
2.2	Ocular Blood Supply	9
2.3	Ocular Diseases	10
2.3.1	Glaucoma	10
2.3.2	Age-related Macular Degeneration	11
2.3.3	Diabetic Retinopathy	12
2.4	Measurement of Ocular Blood Flow	13
2.4.1	Color Doppler Imaging	13
2.4.2	Angiographic Techniques	13
2.4.3	Blue Field Entoptic Technique	14
2.4.4	Laser Doppler Velocimetry	14
2.4.5	Laser Doppler Flowmetry	14
2.4.6	Laser Speckle Technique	14
2.4.7	Pulsatile Ocular Blood Flow	15
2.4.8	Optical Doppler Tomography	15
2.5	Applications of the Fundus Pulsation Interferometer	15
2.5.1	Fundus Pulsations and Ocular Blood Flow	15
2.5.2	Measurements in Healthy Subjects	16
2.5.3	Measurements in Glaucoma	18

2.5.4	Measurements in Age-related Macular Degeneration	20
2.5.5	Measurements in Diabetic Retinopathy	20
2.5.6	Applications of LCTI	21
3	Principles of LCTI	22
3.1	Interference of Two Monochromatic Waves	22
3.2	Interference of Two Partially Coherent Beams	25
3.3	Coherence Time and Coherence Length	29
3.4	Partial Coherence Interferometry	31
3.4.1	Basic Principles of Partial Coherence Interferometry	31
3.4.2	Dual Beam Partial Coherence Interferometry	34
3.4.3	Laser Doppler Partial Coherence Interferometry	35
3.4.4	Optical Coherence Tomography	35
3.5	Measurement of Ocular Fundus Pulsations	37
3.5.1	The Fundus Pulsation Interferometer	37
3.5.2	Low Coherence Tissue Interferometry	39
4	Optical Setup	40
4.1	Overview	40
4.2	Digital Filtering	43
4.3	Laser Safety	43
5	Application of DOE	45
5.1	Gullstrand's Eye Model	45
5.2	Calculation of Fringe Contrast and Spacing with DOE	46
5.2.1	Ray Transfer Matrix Analysis	46
5.2.2	Fringe Contrast	47
5.2.3	Fringe Spacing	53
5.3	Measurements with DOE	54
6	Fringe Contrast	55
6.1	Influence of Distance from Cornea	55
6.2	Influence of Partial Coherence	56

<i>CONTENTS</i>	viii
7 In vivo Measurements	59
7.1 Measurements at 0° and 7°	59
7.2 Measurements from -2° to 19°	62
8 Digital Image Enhancement	65
8.1 Introduction	65
8.1.1 Removal of Local Irregularities	65
8.1.2 Flat Fielding	65
8.2 Fast Background Subtraction for Online Inspection	66
9 Conclusion	67
Appendix	69
Publications and Conference Proceedings	71
Bibliography	72
Abbreviations and Acronyms	78
List of Figures	81
List of Tables	83
Curriculum Vitæ	84

Chapter 1

Introduction

In this chapter the motivation for developing the low coherence tissue interferometer and the principles of the system are briefly explained.

1.1 Motivation

The measurement of fundus pulsations (i.e., distance variations between cornea and retina during the cardiac cycle) has become an important tool for the study of various ocular diseases, which are associated with alterations in choroidal blood flow, such as age-related macular degeneration (AMD), glaucoma, and diabetic retinopathy, and for the study of the influence of several vasoactive drugs on ocular blood circulation [1–7]. Choroidal blood vessels are difficult to access because they are located behind the outer retina (see chapter 2). Different techniques were proposed to gain insight into choroidal blood flow based on angiography [8], laser Doppler flowmetry [9], pneumotometry [10], and color Doppler imaging of the posterior ciliary arteries [11]. Fundus pulsation measurement based on a laser interferometric method has been introduced by Fercher [12] and Schmetterer [13]. In these systems, the eye is illuminated by a collimated laser beam of long coherence length. Part of the light is reflected at the front surface of the cornea, another part at the fundus. Due to a phenomenon called fundus pulsation, which is described in detail later, the distance between the front surface of the cornea and the retina changes with the heart cycle. The two reflected waves generate concentric circular interference fringes, which are imaged onto a linear CCD array (see Fig. 1.1). The signal of the CCD array is recorded over time, resulting in a so-called *synthetic interferogram* covering information on the time course of changes in corneo-retinal distance. The maximum distance change during the cardiac cycle is called fundus pulsation amplitude (FPA). The reflection from the posterior segment most likely occurs from the retinal pigment epithelium (RPE) or Bruch's membrane [5]. Only the interferogram resulting from the strongest reflection of the posterior pole is visible. Other interferogram systems, which may arise from other retinal interfaces, cannot be observed by this method.

Based on this approach it has been shown that the phenomenon of fundus pulsation results from the rhythmic filling of the choroid during the cardiac cycle. During systole the blood flow entering the eye exceeds the blood flow leaving the eye through the ocular veins. Hence, the choroid engorges, associated with a slight protrusion of the retinal structures toward the cornea and an outward movement of the sclera due to an increase in intraocular volume. Whereas the former can be measured with laser interferometry, the latter cannot be quantified

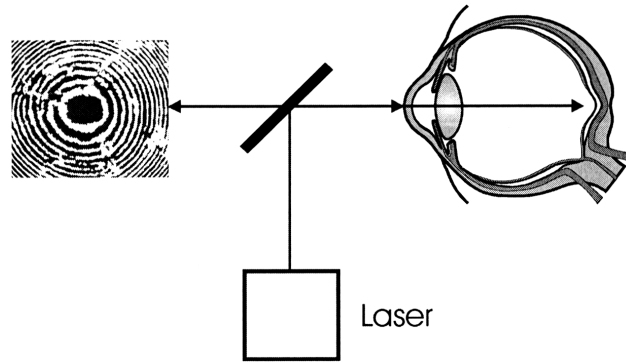


Figure 1.1: Interference fringes generated by reflections from the front surface of the cornea and the retina (from [14]).

by any previously presented method. Relying on a mathematical model of the choroid, realistic measures of choroidal blood flow in humans based on FPA measurements have been obtained [15]. The change in ocular volume during the cardiac cycle is associated with a change in intraocular pressure [10]. It has been shown that there is a high degree of correlation between the pulse amplitude of this intraocular pressure change and the FPA in healthy young emmetropic subjects [5, 16, 17]. In addition, it has been shown that there is an association between FPA and the pulsatile ocular blood flow (POBF), as calculated from the time course of the intraocular pressure changes [5, 16, 17]. One problem with the calculation of POBF from laser interferometric data is associated with the fact that distance changes between the anterior surface of the cornea and the submacular sclera cannot be measured [15]. In this work, an approach called low coherence tissue interferometry (LCTI), which allows to measure distance changes between the cornea and pre-selected reflecting interfaces at the posterior pole of the eye, such as different retinal and choroidal layers or structures in the optic nerve head (ONH), is introduced.

1.2 Overview of LCTI

The use of short coherent light for imaging purposes has gained wide application in ophthalmology. The measurement of the eye length as well as the determination of intraocular distances are based on partial coherence interferometry (PCI) using light of high spatial coherence, but low temporal coherence [18–21]. Applications of this technique *in vivo* have been reported for measuring the length of the human eye [22, 23]. This technique forms the basis of the commercially available IOL master (Zeiss, Jena, Germany) for the measurement of axial eye length.

For illumination, an superluminescent diode (SLD) with short coherence length l_c is used. The beam is split by an external Michelson interferometer with unequal arm lengths into two components, which have a path difference equal to twice the arm length difference of the interferometer. This dual beam illuminates the eye and is reflected at the cornea and at the various layers of the fundus. If one of the intraocular distances equals (within l_c) the path difference, the beams reflected at the respective interfaces will interfere.

One of the mirrors of the Michelson interferometer is mounted on a stepper motor and moved at a constant speed v . The Doppler shift of the corresponding beam due to this movement is $f_D = 2v/\lambda$. Thus, the superposition of the two beams is modulated by f_D . The beams

are focused onto a photodetector (avalanche photo diode (APD)). This signal is amplified and filtered by a bandpass filter with a central frequency of f_D . The envelope of the signal is recorded by a data acquisition card (DAC) as a function of the position of the stepper motor (which corresponds to the arm length difference d of the Michelson interferometer), resulting in a curve called an *optical A-scan*. From the positions of the signal peaks in an A-scan, the respective optical intraocular distances can be obtained directly. The resolution that can be achieved by this technique is of the order of l_c . For a Gaussian-shaped spectrum, the coherence length (in air) can be calculated by

$$l_c = \frac{2 \ln 2}{\pi} \frac{\lambda_0^2}{\Delta\lambda}, \quad (1.1)$$

where λ_0 is the central wavelength and $\Delta\lambda$ the full width at half maximum (FWHM) bandwidth of the light source. The advantage of the dual-beam PCI technique for the measurement of axial eye length is the elimination of the effects of longitudinal eye motions [18–21].

The basic idea of LCTI is to combine the principles of PCI and fundus pulsation measurement. In the previously presented approach to measure fundus pulsations [13], the eye is illuminated by a collimated laser beam of high coherence length with a wavelength of 783 nm. The beam is reflected at the front surface of the cornea and at the retina. The wave originating from the front surface of the cornea is close to spherical, while the wave reflected from the fundus is plane. Therefore, the two waves generate nonlocalized concentric circular interference fringes [5]. The maximum contrast of the interference pattern arises approximately 30 to 40 mm in front of the eye, depending on the test subject. A distance variation between cornea and retina causes a change in interference order $\Delta N(t)$, which can be determined by counting the fringes moving through a fixed point. The change in optical distance $\Delta L(t)$ can then be calculated by $\Delta L(t) = \Delta N(t) \cdot \lambda/2$, allowing for the calculation of the FPA.

The plane of maximum contrast is imaged by a lens onto a linear CCD, which is positioned in the center of the interference fringes. Each readout of the CCD array is captured by a personal computer (PC) and plotted along the time axis, resulting in a synthetic interferogram. By counting the fringes moving inward and outward, the change of interference order ΔN can be drawn as a function of time resulting in a contraction-dilatation graph.

To allow for measurements of time-resolved distance changes between the front surface of the cornea and pre-selected retinal layers, the following approach is employed. LCTI comprises a PCI system for the measurement of axial eye length. In the detection arm, an additional beamsplitter is introduced and part of the light is directed toward a CCD array, whereas the other part of the light is directed toward the APD for the measurement of intraocular distances. This allows for real-time assessment of tissue pulsations as long as the optical distances between the two interferometer arms and the optical distance between the two ocular surfaces are within the coherence length of the light source. Hence, the corresponding layer is pre-selected by the position of the mirrors within the Michelson interferometer.

The measurement process comprises two steps. First, an eye length measurement is performed on the test subject. The peak positions (corresponding to intraocular layers) of the signal curve are determined automatically by a search algorithm, and are displayed on the front panel of the graphical programming interface LabView, starting with the strongest reflecting layer. By selecting any of the peaks, the stepper motor is driven to that position. In the second step, the flip mirror is turned out of the optical path, and the plane ≈ 30 mm in front of the eye is imaged onto the linear CCD array (LCCD). The signal from the LCCD is recorded by a PC and displayed in LabView. Since the relative movement between the

retinal layers and the cornea is smaller than the coherence length, time resolved recording is possible.

Chapter 2

Medical Aspects

This chapter introduces the application of fundus pulsation measurement and LCTI in ophthalmology. For this purpose, first the anatomy of the eye is briefly described. In the subsequent sections, several ocular diseases, which are hypothesized to be related to alterations in ocular blood flow, as well as different methods for the measurement of ocular blood flow are illustrated. Then the applications of the pulsation interferometer and of LCTI in healthy subjects as well as in ocular pathologies are explained.

2.1 Anatomy of the Eye

A cross section diagram of the human eye with indication of the main parts is given in Fig. 2.1. The eye ball is nearly spherical with an average diameter of approximately 24 mm. The outer layer of the eye ball is the intransparent *sclera*, which is on the front side connected to the transparent *cornea*. The latter has a bulging shape with an average radius of curvature of 7.8 mm, an average thickness of 0.5 mm [24] and plays an important role in the image-forming process by refracting the incident light. Attached to the sclera is the highly vascular *choroid*, which has the main function of providing nutrients to the photosensitive layer. Moreover, the choroid contains a pigment absorbing excess light and, thus, preventing blurred vision. In the anterior segment of the eye the choroid is attached to the *ciliary muscle*, which controls the shape of the flexible lens by contraction and relaxation, and to the *iris*, a diaphragm of variable size, which has the function of adjusting the size of the pupil and, thus, regulating the amount of light admitted into the eye. Between cornea and iris lies the *anterior chamber of the eye*, which is filled by a watery fluid called *aqueous humour*. This has the function of maintaining the intraocular pressure of the eye and providing nutrition to lens and cornea. The aqueous humour is produced by the ciliary capillaries and drained via the *trabecular meshwork* and *Schlemm's canal* into the blood system. A detailed diagram of the anterior segment of the eye is shown in Fig. 2.2. The chamber behind the lens of the eye is filled by the *vitreous humour* (also called *vitreous body*), a transparent jelly-like fluid that occupies about 80 per cent of the eye ball. In the posterior segment of the eye the vitreous body is circumscribed by the *retina*, which contains the photosensitive elements (*rods* and *cones*). The retina is described in detail in the next paragraph. While cornea and lens have the main influence on the image-forming process, the focal length of the eye is also determined by the aqueous humour and the vitreous humour. The refractive indices of the transparent parts of the eye are given in table 2.1 [24–27]. When calculating the average index of refraction,

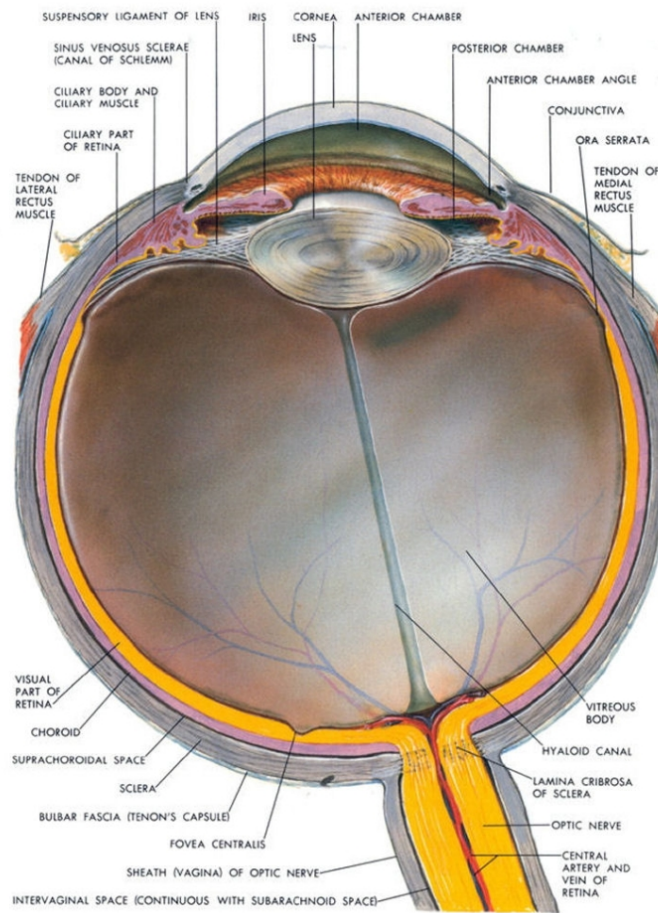


Figure 2.1: Cross section diagram of the human eye with indication of the main parts (from: cibavision.com).

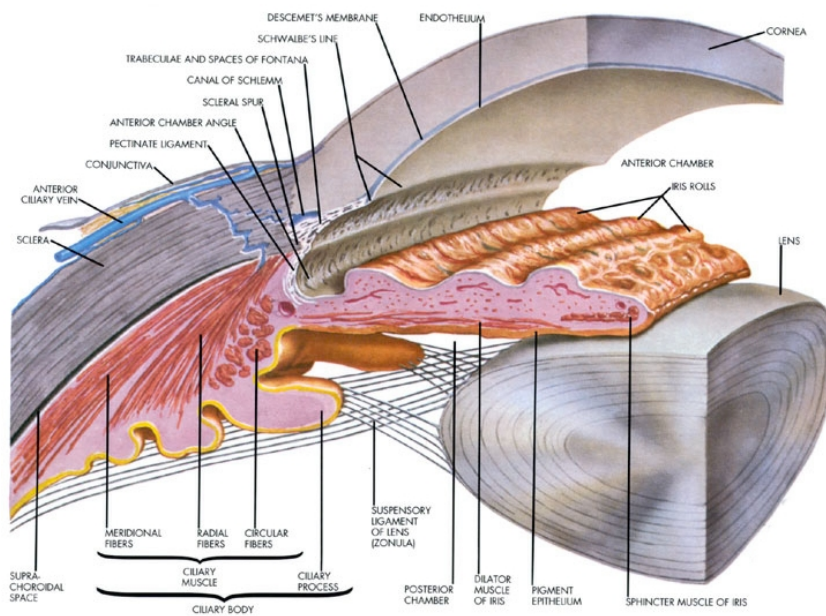


Figure 2.2: Cross section diagram of the anterior segment of the human eye (from: cibavision.com).

Table 2.1: Refractive indices of the transparent parts of the eye

part	refractive index
tear film	1.336 - 1.357
cornea	1.38
aqueous humour	1.34
lens	1.41
vitreous humour	1.336
retina	1.4
average	1.336

one has to take into account the various (optical) path lengths that the beam passes before entering the retina. For this reason, the vitreous humour contributes most to the calculation of this average.

A schematic diagram of the retina can be seen in Fig. 2.3(b) together with the location of the fovea in a cross section diagram of the eye in Fig. 2.3(a). The retina has an average

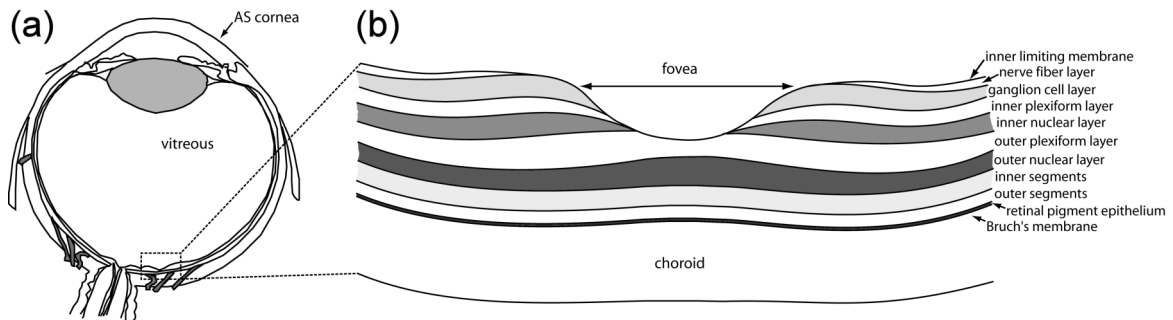


Figure 2.3: Schematic diagram of (a) the human eye with (b) the main layers in the posterior segment of the eye. AS, anterior surface of the cornea.

thickness of 0.24-0.27 mm (0.15 mm in the foveal region) [28, 29] and contains several layers. The anatomy of the retinal layers and the retinal cells is depicted in Fig. 2.4.

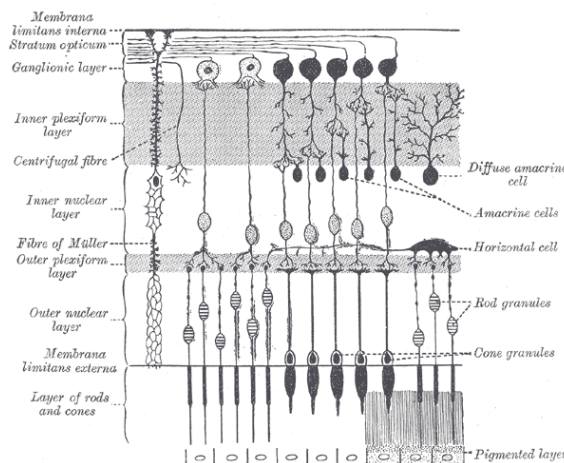


Figure 2.4: Plan of retinal layers and nerve cells (from: Gray's Anatomy).

The *inner limiting membrane (ILM)* forms the boundary between the vitreous body and the retina and contains the *Müller cells*, which protect and supply the surrounding nerve cells

(*ganglion cells*). Recently it has been shown that Müller cells also work as light conductors funneling light to the photoreceptor cells [30], which is necessary because of the counter-intuitive arrangement of the retina: Light must first pass through the ganglion cells and through the thickness of the retina before reaching the visual cells. The *retinal nerve fiber layer (RNFL)* consists of nerve fibers (*axones*) of the ganglion cells, which have the function of carrying the information collected by the photosensitive elements (rods and cones) via the optic nerve to the visual cortex of the brain. Located in the *ganglion cell layer (GCL)* are the cellular bodies of the ganglion cells. Attached to the GCL is the *inner plexiform layer (IPL)*, in which the vertical-information-carrying *bipolar cells* are connected to the ganglion cells. The IPL plays an important role in the processing of the image obtained by the photoreceptors: Since the number of photoreceptors in the retina is about 100 times larger than the number of ganglion cells in the optic nerve, the image information is compressed (spatially encoded) in the nerve cell network of the IPL before being transmitted to the visual cortex. The *inner nuclear layer (INL)* contains the bodies of the bipolar cells, the *amacrine cells*, and the *horizontal cells*. While the bipolar cells transmit the signals from the photoreceptors to the ganglion cells, the *amacrine cells* serve to integrate and modulate the visual signal. The *horizontal cells* regulate the input from the photoreceptor cells and, thereby, adjust the eye to both bright and dim light conditions. Much thinner than the IPL is the *outer plexiform layer (OPL)*, in which the endings of rods and cones are connected via synapses to horizontal and bipolar cells. Adjacent to the OPL lies the *outer nuclear layer (ONL)*, which contains the rod and cone granules. The rod granules are spherically shaped and lie at different vertical positions in the ONL. Much less numerous than the rod granules are the cone granules (except in the macula), which are situated close to the *external limiting membrane (ELM)* in a single row. The ELM separates the cell bodies of the rods and cones from their *inner* and *outer segments*, which lie in the *photoreceptor layer*, also referred to as *layer of rods and cones*. Lying on the *RPE* and pointed toward the back of the eye, the outer segments consist of many stacked disks, which contain the light absorbing materials (visual pigments such as rhodopsin or color pigment). The organelles (mitochondria, ribosomes and membranes, where the pigments are assembled) are located in the inner segments. The RPE, which is firmly attached to the photoreceptor cells and to the underlying choroid, has the function of supplying the visual cells with nutrients. Placed directly below the RPE lies *Bruch's membrane*, which plays an important role in the transport of metabolic waste products from the photoreceptors to the choroid.

The spot where the ganglion cell axones exit the eye to form the optic nerve is called *optic disc* or *optic nerve head*. It is a circular to oval white area that measures approximately 2 mm and is located 3-4 mm to the nasal side of the fovea. No light sensitive rods or cones are located in the optic disc, which leads to a break in the visual field referred to as *blind spot*. Located centrally in the optic disc is a depression called *optic cup*. From the center of the optic nerve radiate the large blood vessels of the retina. Most important is the *central retinal artery*, which carries the retinal blood flow and nourishes the inner retinal layers. The retinal circulation accounts for approximately 5-10 per cent of total ocular blood flow [31]. The central retinal artery normally has 4 main branches, curved towards and running around the fovea. The outer retinal layers, particularly the photoreceptors, are supplied by the choroid. The choroid, in turn, is supplied by the ciliary arteries (see section 2.2). Based on a study in monkey eyes and assuming that monkeys and humans have a similar physiology of the eye, a ratio of choroidal to retinal blood flow of 10:1 was found [32].

The *macula* or *macula lutea* is an oval-shaped highly pigmented yellow spot that has a diameter of 5 mm. Located close to the center of the macula is the *fovea*, a small pit that contains the largest concentration of cone cells in the eye. Responsible for central vision, the

fovea has the highest visual acuity of all retinal structures. Around the fovea extends the cone-dominated *central retina* for about 6 mm, then the *peripheral retina*, which is dominated by rods. Overall, the retina contains about 7 million cones and 100 million rods. The yellow pigments that give the macula its color are *lutein* and *zeaxanthin*. These pigments act as short wavelength filter, thereby protecting the eye from ultraviolet irradiation.

2.2 Ocular Blood Supply

The eye and other structures in the orbit (extraocular muscles, several nasal muscles, etc.) are supplied by the *ophthalmic artery*, which is a branch of the *internal carotid artery* and enters the orbit together with the optic nerve through the *optic canal* (see Fig. 2.5). The

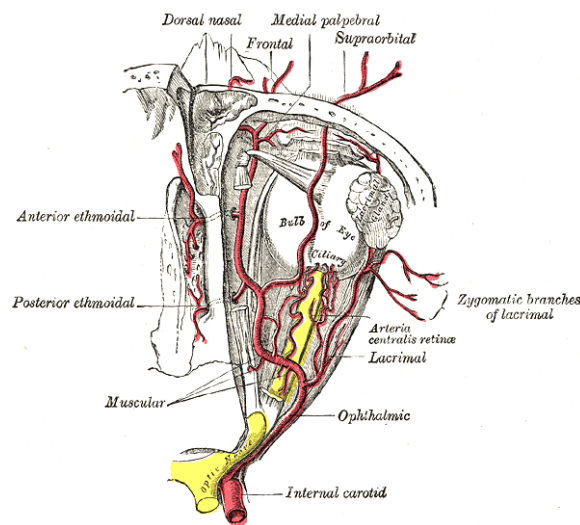


Figure 2.5: The ophthalmic artery and its branches (from: Gray's Anatomy).

central retinal artery arises from the ophthalmic artery, piercing the optic nerve close to the eye ball and, as mentioned before, sending branches over the inner surface of the retina. It supplies the inner retinal layers, in particular the nerve fibers, including those that reach over the fovea. However, the area around the fovea and the fovea itself are not supplied by the central retinal artery or its branches, but by the choroid, which also nourishes the outer retinal layers. Also from the ophthalmic artery arise the *ciliary arteries*, which divide into two *long posterior ciliary arteries* and up to 12 *short posterior ciliary arteries* that enter the eye immediately adjacent and around the optic nerve. While the short posterior ciliary arteries directly supply the choroid, the long posterior ciliary arteries supply the choroid from the inner side via recurrent branches. Moreover, the short posterior ciliary arteries provide blood supply to the ONH and the *lamina cribrosa*, which is a mesh-like structure formed by collagen fibers that are connected to the scleral wall. The nerve fibers of the ONH run through the pores of this collagen structure. The lamina cribrosa maintains the pressure gradient between the inside of the eye and the adjacent tissue. Due to the intraocular pressure (IOP) it bulges slightly outwards. Since the lamina cribrosa is much thinner than the sclera, it is more sensitive to pressure changes and tends to be deformed by increased IOP. Alterations in the biomechanical properties of the lamina cribrosa are assumed to play an important role in the development of glaucoma (see subsection 2.3.1).

After running through the larger vessels of the choroid and the *choriocapillaris* (the innermost

layer of the choroid), the blood drains into the *vortex veins*, which are branches of the *superior* and *inferior ophthalmic veins*. The *central retinal vein* runs through the optic nerve and drains blood from the retinal capillaries into the larger veins outside the eye.

2.3 Ocular Diseases

Several ocular diseases, including glaucoma, age-related macular degeneration and diabetic retinopathy are hypothesized to be related with alterations in ocular blood flow. A short overview of the pathophysiology and pathogenesis of these diseases is given in the following section.

2.3.1 Glaucoma

In glaucoma the optic nerve is damaged, leading to irreversible loss of vision. Although increased IOP is a risk factor, people with normal levels of IOP can be affected by this disease as well (normal tension glaucoma (NTG)). In early stages of glaucoma, no symptoms may occur. However, if untreated, glaucoma leads to permanent damage of the optic nerve and, thus, to a loss of visual field or blindness. The disease can occur as *open angle glaucoma* or *angle closure glaucoma*. While open angle (chronic) glaucoma develops slowly, angle closure glaucoma appears abruptly and leads to a quick vision loss. However, due to the sudden discomfort of angle closure glaucoma most patients seek medical attention before the optic nerve is gravely damaged. While anyone can be affected by glaucoma, the risk is much greater for people over the age of 60. Also, people of African descent and people with a family history of glaucoma have an increased risk for this disease. In some cases, which are referred to as *secondary glaucomas*, other diseases or external events trigger or contribute to increased IOP, for example continuous use of steroids, ocular trauma or severe diabetic retinopathy. Testing for glaucoma usually includes measurement of IOP via tonometry, visual field test, examination of the anterior chamber, and examination of the optic nerve via optical coherence tomography (OCT) or scanning laser ophthalmoscopy (SLO). Measurement of IOP via tonometry should always be augmented by assessment of central corneal thickness (CCT), since deviations from average corneal thickness lead to errors in tonometric IOP measurement.

The most common form is primary open angle glaucoma (POAG). The increased pressure is caused by a blockage of the trabecular network, which has the function of draining the aqueous humour into the blood system. This form of the disease develops slowly and leads to imperceptible gradual vision loss. First, peripheral vision is affected, but entire vision will be lost if the glaucoma is untreated. It can be treated by drugs that decrease formation of aqueous humour or open up the passage and, thus, increase trabecular outflow.

Angle closure glaucoma, which is also known as *acute glaucoma*, is – in caucasians – much more rare than open angle glaucoma. In this form of the disease the IOP usually rises abruptly, leading to a quick progress of vision loss. The reason for the sudden increase in IOP is a blocking of the drainage canal of the anterior chamber by the outer edge of the iris, which is pushed forward against the drainage system by an (already) increased IOP. Angle closure glaucoma is usually treated surgically by removing a small portion of the outer edge of the iris, and, thereby, creating new channels for fluid to flow from behind the iris.

It is hypothesized that the biomechanical properties of the ONH, the lamina cribrosa and the sclera play a role in the development of glaucoma. A topical study indicates increased

ocular rigidity in patients with POAG based on measurements of IOP amplitude with pneumotometry and FPA by laser interferometry [7]. The study is described in detail in section 2.5.3. The findings are compatible with several previous animal experiments and support the hypothesis that the biomechanical properties of ocular tissue are relevant in the diseases process. Furthermore, there is evidence that altered ONH blood flow plays a role in the development of glaucoma. In a recent study employing laser Doppler flowmetry (LDF) and laser interferometric measurement of FPA, reduced ONH and choroidal blood flow as well as an abnormal association between systemic blood pressure and ocular perfusion was found in patients with POAG or ocular hypertension (OHT) [33]. Thus, vascular dysregulation seems to be related to the development of glaucoma.

2.3.2 Age-related Macular Degeneration

Age-related macular degeneration (AMD) is the most common cause of blindness in Western countries. It usually affects older adults, resulting in a loss of vision in the center of the visual field because of damage to the central retina (macula lutea) [2, 34]. Due to the blurring of central vision, AMD can make it impossible to read or recognize faces, although usually enough peripheral vision remains for other activities of daily life. AMD occurs in *dry* and *wet* forms.

Dry AMD is associated with small, yellow deposits of extracellular material (*drusen*) close to Bruch's membrane. Although the presence of some small drusen is normal with advancing age, larger and more numerous drusen are an early sign of dry AMD. Due to their location between the RPE and its vascular supply (choriocapillaris), it is assumed that drusen deprive the RPE and photoreceptors of oxygen and nutrients, leading to a loss of cone and rod cells. Furthermore, drusen can lead to a detachment of the retina. Currently there is no treatment for dry AMD. However, the *Age-Related Eye Disease Study (AREDS)*, initiated by the National Eye Institute, Bethesda, MD) has shown that high doses of antioxidants (vitamins A and C and beta carotene) and zinc slow the progression of dry AMD and, in some patients, improve visual acuity. A current study indicates that the antioxidative AREDS medication reduces oxidative stress-induced endothelial dysfunction by eliminating reactive oxygen species (ROS), which are free radicals that contain the oxygen atom [35].

The more severe and rapid form of AMD is wet AMD, accounting for approximately 15 per cent of all cases of this disease. It causes loss of vision due to abnormal blood vessel growth (*choroidal neovascularization*) from the choriocapillaris through Bruch's membrane, leading to blood leakage below the macula. Eventually, these neovascularizations cause irreversible damage to the photoreceptors and – in some cases – detachment of the retina. Wet AMD can be treated by photodynamic therapy (laser coagulation) of the abnormal blood vessels. Furthermore, new drugs, so-called *anti-vascular endothelial growth factor (anti-VEGF) agents*, which are directly injected into the vitreous humour, can cause regression of neovascularizations and improvement of vision.

In recent years, the understanding of the pathogenesis and pathophysiology of AMD has improved significantly. Most importantly, several studies have revealed that this disease has a strong genetic component [34]. These findings indicate that the innate immune system is implicated in the mechanisms leading to AMD. However, other factors appearing to play a part in the development of the disease have been found as well: Recently, it has been discovered that dysfunctional ocular microcirculation seems to be contributing to AMD pathophysiology [36, 37]. This model assumes an increase in choroidal vascular resistance due to a

decreased ocular compliance induced by progressive infiltration with lipid. This reduction in choroidal perfusion hampers the processing of outer segment lipid by the RPE, leading to the clinical characteristics of the disease, including drusen and choroidal neovascularization [38]. This hypothesis has gained support from a number of studies indicating abnormalities in the choroidal vasculature as well as dysfunctional choroidal blood flow in AMD [8, 39].

2.3.3 Diabetic Retinopathy

Diabetic retinopathy is – besides AMD – one of the two leading causes of blindness in adults in the industrialized nations [34]. It affects patients with diabetes mellitus in type I (insulin-dependent) and type II (non-insulin-dependent). Diabetic retinopathy can cause vision loss in two ways: First, it can lead to fluid and protein deposits under or on the macula, causing it to swell. This condition, which is referred to as *macular edema*, often causes blurred vision, making it hard to do things like drive or read. Furthermore, in *proliferative diabetic retinopathy (PDR)*, which is the most advanced stage of the disease, fragile, abnormal blood vessels develop at the back of the eye. These vessels often leak blood into the center of the eye, thus blurring vision. About 50 per cent of the patients with PDR also have macular edema. There are effective treatments for diabetic retinopathy, which can reduce vision loss even in advanced stages of the disease, when applied before the retina is severely damaged. Vascular proliferation in PDR is treated with laser surgery (photocoagulation) and anti-VEGF agents, which reduce vessel growth. Intravitreal injection of *triamcinolone acetonide* (a long-term steroid) decreases macular edema and improves visual acuity. In patients with larger amounts of blood in the vitreous, *vitrectomy* is used to restore vision by removing the cloudy vitreous and replacing it with saline solution.

The mechanisms underlying the development of diabetic retinopathy are still not fully understood. It is assumed that elevated glucose levels lead to vascular abnormalities in the retina and to progression of the disease. However, there are still different hypotheses about the processes taking place until pathologic changes in the retina become visible, including pericyte loss, oxidative stress, thickening of the capillary basement membrane, genetic factors, and hemodynamic factors. Some of the mechanisms leading to vascular proliferation in advanced diabetic retinopathy have been identified in recent years [34].

Recent studies measuring retinal blood flow in different stages of diabetic retinopathy with laser Doppler devices (see section 2.4) observed unaltered [40] or slightly increased [41] retinal blood flow in diabetics with no, or minimal, retinopathy, compared with healthy control subjects. However, retinal blood flow appears to increase in the later stages of the disease and to decrease again in PDR, while venous and arterial vessel diameters seem to be increased in most cases.

The role of choroidal blood flow in diabetic retinopathy is yet unclear. Results of studies using pneumotometry (see section 2.4) for the observation of pulsatile choroidal blood flow are ambiguous. With fundus pulsation interferometry, a small reduction in pulsatile choroidal blood flow in PDR but no change in early diabetes was found [42] as well as an increase with the progression of nonproliferative diabetic retinopathy [43]. Additionally, autoregulation of choroidal and retinal blood flow in response to different stimuli (elevation of ocular perfusion pressure, increased blood pressure and hyperoxia) was found to be disturbed in patients with diabetes [34]. The exact mechanisms that finally lead to irreversible defects of the retina still need to be proved in future studies.

2.4 Measurement of Ocular Blood Flow

Abnormalities in ocular blood flow, which is measured as blood flow velocity multiplied by cross sectional area, are assumed to play a significant role in the development of several ocular diseases including AMD, diabetic retinopathy, and glaucoma. Thus, the non-invasive assessment of ocular blood flow has become an important tool for the study of these diseases. The different techniques available for this purpose are briefly explained in the following sections.

2.4.1 Color Doppler Imaging

In color Doppler imaging (CDI) two-dimensional tomograms (B-scans) are generated by an ultrasound technique [3,6]. The velocity information is obtained from the Doppler shift of the moving erythrocytes and is displayed color-encoded together with the B-scan. With CDI blood velocities in the retrobulbar (i.e., *larger extraocular*) vessels can be assessed, in particular the peak systolic velocity (PSV) and the end diastolic velocity (EDV). The mean flow velocity (MFV) is calculated as the time mean of the spectral outline. Since no quantitative information on vessel diameter is obtained by CDI, the total blood flow cannot be calculated with this method. Hence it is often difficult to decide whether an increase in blood velocities is related to an increase in arterial blood flow or a constriction of the vessel.

2.4.2 Angiographic Techniques

Fluorescein angiography – originally introduced by Novotny and Alvis [44] – has become an important tool for the qualitative assessment of retinal blood flow [3,6]. Angiography allows for the visualization of anatomic structures by the passage of a fluorescent dye. For this purpose the dye (usually sodium fluorescein) is injected into the arm vein of the patient. On illumination with blue light the dye starts to fluoresce. When recorded by a video camera (*videoangiography*) the concentration of the fluorescent dye can be measured over time. For the assessment of retinal blood velocity the time required for the dye to pass through the retinal circulation is measured. The *mean retinal circulation time* (i.e., the time difference between venous and arterial times) is inversely proportional to the retinal blood velocity. If the retinal vessel diameters are measured additionally, the retinal blood flow can be estimated. Alternatively to the mean retinal circulation time the *arterio-venous passage time*, defined as the time between the first appearance of the dye in a retinal artery and in the corresponding vein, can be used for the assessment of retinal haemodynamics.

When applying fluorescence angiography to clinical or experimental studies, several limitations of this method have to be considered. Most importantly, the technique assumes that all the blood of an area supplied by a specific artery is drained by the corresponding vein, which may not hold true in all cases, especially in patients with vascular disorders. Secondly, it is assumed that the sum of all vessel diameters is directly related to retinal blood volume. However, in patients with diabetic retinopathy, where areas of retinal non-perfusion exist, this relation seems improbable. Another problem is the leakage of fluorescein from retinal vessels in patients with later stages of diabetic retinopathy.

Choroidal blood flow can be visualized by indocyanine green (ICG) angiography, which applies near infrared light for triggering fluorescence, and, thus, has a better penetration through the pigmented ocular structures. This technique is used in combination with scanning laser ophthalmoscopy to calculate choroidal blood flow.

2.4.3 Blue Field Entoptic Technique

This technique for the investigation of leucocyte dynamics makes use of the blue field entoptic phenomenon, which occurs when looking into blue light with a narrow optical spectrum at a wavelength of approximately 430 nm [3, 6]. Under these conditions many tiny corpuscles can be seen by the patient around an area at the center of the fovea. The most probable reason for this phenomenon is that erythrocytes, but not leucocytes absorb short wavelength light. Thus, the passage of a white blood cell is perceived as a flying corpuscle. To extract quantitative information, a simulated particle field is shown to the subject under study. By adjusting particle number, mean flow velocity, and pulsatility of motion, subjects can bring the simulated field into accordance with their own entoptic observation. From the parameters selected by the patient the retinal blood flow and flow pulsatility can be calculated. The main disadvantages of this technique are its subjective nature and, thus, its poor reproducibility.

2.4.4 Laser Doppler Velocimetry

In laser Doppler velocimetry (LDV) a retinal vessel is illuminated by a high coherent laser beam. The beam is reflected and scattered on the vessel wall as well as the moving erythrocytes. Hence the back-scattered light consists of a mixture of shifted and unshifted frequencies. The Doppler shift power spectrum (DSPS) therefore consists of a range of frequencies, where the maximum frequency shift corresponds to the maximum center velocity occurring in the vessel under study. Bidirectional LDV, which detects the Doppler frequencies from two different, well-known directions allows for absolute measurement of the maximum blood flow velocity. When the retinal vessel diameter is measured additionally, the volumetric blood flow can be determined. However, quantitative information on the velocity profile in retinal arteries and veins cannot be extracted from the DSPS. Thus, for quantification of total blood flow a theoretical relation between maximum center velocity and mean flow velocity within a vessel has to be employed.

2.4.5 Laser Doppler Flowmetry

In this technique the laser beam is not directed towards a retinal vessel but on vascularised tissue with no larger vessels [6]. Based on a theory formulated by Bonner and Nossal [45], which describes scattering of light in tissue assuming a complete randomization of light directions impinging on the erythrocytes, relative measures of the mean blood flow velocities and blood volume can be obtained. Due to variations in vascular density and vessel orientation in the relatively small volumes of tissue sampled by LDF there is a considerable variation in scattering properties between different subjects, which makes it difficult to compare interindividual LDF data. However, since the intraindividual reproducibility is quite high, LDF has considerable potential to investigate the reactivity of the ocular vasculature to different physiological and pharmacological stimuli.

2.4.6 Laser Speckle Technique

This technique makes use of the laser speckle phenomenon, which occurs when the ocular fundus is illuminated by a coherent laser beam [6]. The light backscattered from the rough surface of the fundus exposes a rapidly varying pattern. The rate of variation of this pattern

gives an estimate of blood cell velocity and, thus, can be used for the quantification of retinal blood flow [46]. Based on this technique, instruments for the assessment of retinal blood flow and of choroidal and ONH blood flow have been developed. Since no information about vessel diameters is available, these instruments are capable of the measurement of the blood flow velocities only.

2.4.7 Pulsatile Ocular Blood Flow

Two different approaches have been proposed for the assessment of POBF. The *pneumotonometric* approach is based on the fact that IOP changes during the cardiac cycle. The maximum IOP change during the cardiac cycle is called *pulse amplitude* and can be used to calculate POBF based on a theoretical model [47,48]. More recently, a modified pneumotonometer connected to a PC has been used to record the ocular pulse wave and to calculate POBF. In a different approach, POBF is assessed by measuring distance changes between cornea and retina during the cardiac cycle by the fundus pulsation interferometer [13,49]. The maximum distance change during the heart cycle is called fundus pulsation amplitude (FPA) and has been shown to be strongly correlated to POBF. An advantage of the interferometric measurement of fundus pulsations is the high topographic resolution of this method, which is of clinical importance since ischaemic or inflammatory choroidal lesions are typically localised. The main limitation of these methods is the lack of information on the non-pulsatile (constant) component of the ocular blood flow.

2.4.8 Optical Doppler Tomography

A novel approach for the measurement of ocular blood flow is optical Doppler tomography. It combines the principles of laser Doppler and OCT (see subsection 3.4.4). Instruments for the assessment of velocity profiles in retinal arteries and veins have been realized using time-domain [50,51] and frequency-domain approaches [52,53]. Recently, a device for the measurement of absolute blood flow velocities in retinal vessels using bidirectional optical Doppler tomography has been presented [54].

2.5 Applications of the Fundus Pulsation Interferometer

2.5.1 Fundus Pulsations and Ocular Blood Flow

Both LCTI and the fundus pulsation interferometer presented by Schmetterer [5,13] measure distance variations between the cornea and the fundus that are caused by the rhythmic filling of the ocular vessels during the cardiac cycle. The maximum distance change (i.e., the FPA) is a point measure of ocular volume change $\Delta V(t)$ during the heart cycle assuming an infinitely small beam diameter at the fundus. The ocular volume $V(t)$ increases when the pulsatile inflow through the arteries $F_{in}(t)$ exceeds the outflow through the veins F_{out} . The outflow can be assumed to be steady, i.e., nonpulsatile [55]. Thus, the volume change at a time t can be written as:

$$V(t) - V(t_0) = \Delta V(t) = \int_{t_0}^t F_{in}(t') dt' - F_{out} \cdot (t - t_0). \quad (2.1)$$

The inflow over a pulse stroke period T equals the outflow,

$$\int_0^T F_{in}(t') dt' = F_{out} \cdot T, \quad (2.2)$$

assuming the beginning of the pulse period to be at $t_0 = 0$. Schmetterer and Wolzt studied the association between the FPA measured by the pulsation interferometer and the blood flow velocities in the posterior ciliary arteries assessed by CDI [2]. Multiplication of the time course of the blood flow velocity $v(t)$ with the cross sectional area of the vessels Q yields the blood flow through the respective vessels. Using Eq. 2.1, and assuming constant vessel diameters, leads to a volume change $\Delta V(t)$ of:

$$\Delta V(t) = Q \int_{t_0}^t v(t') dt' - F_{out} \cdot (t - t_0). \quad (2.3)$$

The vessel diameters of the posterior ciliary arteries cannot be determined *in vivo*. However, it is possible to compare the time course of the integrated velocity curve as assessed with CDI to the time course of the fundus pulsation obtained by laser interferometric measurement. The high association between the curves assessed with the two described methods supports the hypothesis that fundus pulsations are predominantly caused by the pulsatile inflow of blood through the posterior ciliary arteries (i.e., the pulsatile choroidal blood flow). This is in accordance with the fact that typically observed pulsatile ocular volume changes are in the order of 900 $\mu\text{l}/\text{min}$, while total retinal blood flows in healthy subjects assessed by LDV are usually much smaller (approximately 40 $\mu\text{l}/\text{min}$) [16].

By the described laser interferometric methods only the pulsatile part of the blood flow can be assessed. The relative fraction of the pulsatile component has not yet been determined. Estimates vary between 80 and 50 per cent [16]. A theoretical model developed by Krakau predicts steady inflow of similar magnitude to the pulsatile one and steady outflow in healthy subjects [56].

2.5.2 Measurements in Healthy Subjects

Schmetterer et al. investigated the association between laser interferometric measurements of fundus pulsations and pneumotometric measurements of IOP pulse and POBF in healthy subjects [16]. An additional aim of the study presented in [16] was to determine the topographic distribution of fundus pulsations.

One study was performed on 28 healthy emmetropic subjects to investigate the association between pneumotometric parameters and FPA. For the laser interferometric assessment of FPA, a high-coherence laser beam with a wavelength of 780 nm was used for illumination of the subject's eye. The pulsation interferometer was coupled to a fundus camera, allowing for real-time inspection of the measurement point on the fundus [13]. POBF was determined using a commercially available pneumotometric blood flow measurement system. This system measures changes in IOP, which are caused by the rhythmic filling of the intraocular vessels, with a pneumatic applanation tonometer. The maximum change in IOP during the heart cycle is called pulse amplitude (PA). The POBF is calculated from the time course of the IOP based on a theoretical model eye [10, 48]. In this model it is assumed that venous outflow is non-pulsatile and that ocular volume changes can be estimated from changes in IOP based on a standard ocular rigidity function. Association between the FPA measured by the pulsation interferometer and pneumotometric parameters was investigated with linear

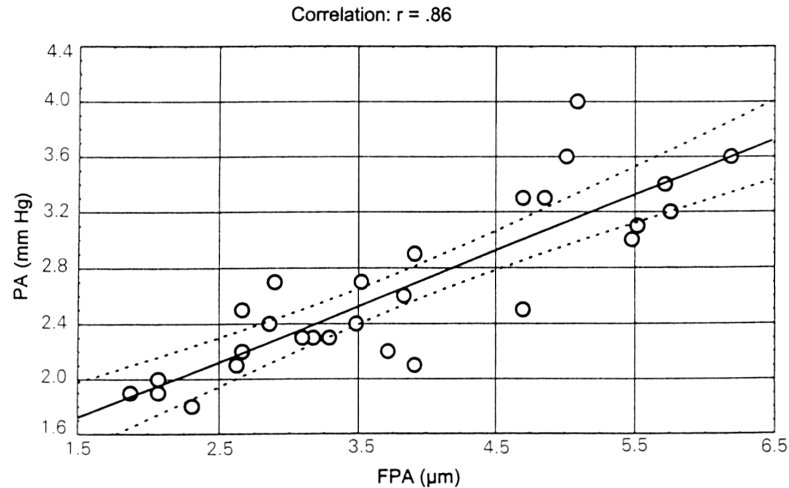


Figure 2.6: Linear correlation ($n = 28$) between FPA and PA in healthy subjects. The regression lines and the 95% confidence intervals are shown.

correlation. The association between FPA and PA is shown in Fig. 2.6. A similar correlation was found for FPA and POBF. The association was highly significant for both parameters. However, the correlation coefficient was higher for FPA versus PA ($r = 0.86$) than for FPA versus POBF ($r = 0.70$). Deviations from a perfect correlation between FPA and PA are caused by several reasons: First, the two parameters are related by the so-called ocular pressure-volume relationship. Changes in ocular volume, which are caused by the pulsatile inflow of blood during systole, cause changes in IOP. For small pressure changes the relation can be expressed as (see also section 2.5.3):

$$E = \frac{\Delta\text{IOP}}{\Delta V}, \quad (2.4)$$

where E is the ocular rigidity, ΔIOP is the change in IOP, and ΔV is the corresponding change in intraocular volume. In this situation, ΔIOP corresponds to PA. FPA, on the other hand, is a measure of ΔV . From Eq. 2.4 it can be seen that the relation between FPA and PA depends on ocular rigidity E . As E varies between different subjects, identical changes in blood volume ΔV do not necessarily lead to identical changes in IOP. Another reason for deviations from the linear correlation between FPA and PA is that FPA is a point measure of the volume change during the heart cycle. For calculation of E using Eq. 2.4 one would need to know the total change in ocular volume, which cannot be estimated from a single-point FPA measurement, since the measured value in the macula depends on the local architecture of the vessels and, moreover, the scleral movement is unknown. Additionally, the FPA in the macula only represents the choroidal circulation, since the retina lacks any vasculature in this region. However, retinal blood flow has only minor influence on the IOP pulse. As mentioned earlier, the association between POBF and FPA was weaker than the association between PA and FPA. The POBF depends not only on PA but also on pulse rate and the time course of the IOP, which in fact may be responsible for the weaker correlation between FPA and POBF. However, FPA can be taken as relative measure of POBF in studies where only minor changes in pulse rate and in the time course of the IOP are to be expected.

Other studies were performed to investigate the topographic distribution of fundus pulsation in a region between 15° nasal and 15° temporal and 10° superior and 10° inferior of the macula (in steps of 5°) as well as in 8 pre-selected points in the region of the optic cup and the neuroretinal rim. A fixation light with adjustable angle was shown to the subject's eye to

measure the FPA at the different pre-selected points. The results of the regional distribution of FPA measurements are shown in Fig. 2.7. FPA was higher in the macula ($3.4 \mu\text{m}$) than

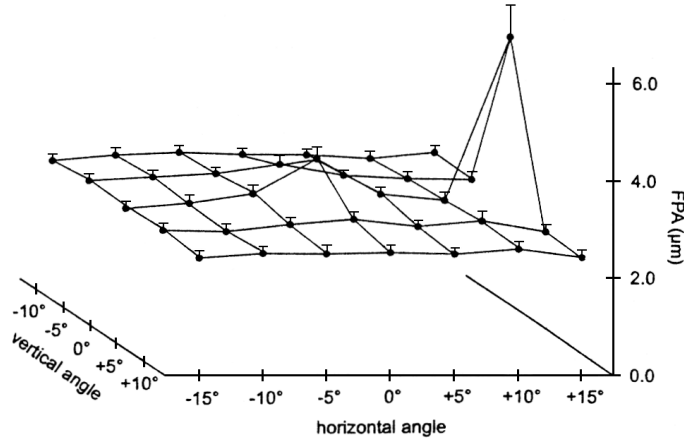


Figure 2.7: Fundus pulsation amplitudes at different angles of vision obtained from 18 subjects and presented as means \pm standard error of mean.

at the surrounding measurement points ($2.6 \mu\text{m}$). The reason for this observation could be related to the fact that the ratio of arteries to veins is higher in the submacular choroid than in the surrounding regions, or to a local irregularity in scleral rigidity.

In the optic disc, which corresponds to the measurement point at $(+15^\circ, 0^\circ)$, the FPA was more than twice as high as at the other measurement points. The FPA values at the 8 pre-selected measurement sites in the optic disc varied between $5.1 \mu\text{m}$ and $13.4 \mu\text{m}$, showing a high within-subject variability of the results obtained at the cup and the neuroretinal rim. The high FPA values that were observed at the disc can firstly be attributed to the fact that the large blood vessels enter the eye in this region and, secondly, to the elastic properties of the ONH, which are still to be studied. LCTI can be an important tool for the investigation of these properties, since it enables, contrary to previous methods, for observation of the movement of structures at various selected and well-defined axial depths. The results of LCTI measurements in the optic disc of a healthy subject at several depth positions corresponding to reflecting interfaces are presented in chapter 7.

2.5.3 Measurements in Glaucoma

As mentioned in section 2.3.1, there is evidence from animal studies and theoretical models that the biomechanical properties of the ONH and the sclera play a role in the development of glaucoma. In a recent study, ocular rigidity was assessed in 70 patients with POAG and in 70 healthy subjects based on measurements of IOP amplitude and FPA [7]. Ocular PA and POBF were assessed with pneumotometry, while the FPA was measured by laser interferometry. The patients with POAG and the healthy control subjects matched for age, sex, IOP and systemic blood pressure.

One approach to gaining insight into the biomechanical properties of the eye is based on the calculation of ocular rigidity E by the Friedenwald equation [57]:

$$E = (\log IOP_1 - \log IOP_2) / \Delta V, \quad (2.5)$$

where IOP_1 and IOP_2 are the highest IOP during systole and the lowest IOP during diastole, respectively, and ΔV is the ocular volume change during the cardiac cycle. E is a measure of

combined structural stiffness of the sclera, choroid, Bruch's membrane, retina, and cornea. In a biomechanical context, ocular tissues can become stiffer, because they become more robust (e.g., thicker) or their extracellular matrix changes in a way that they are individually or together stiffer. In this study, it was supposed that scleral stiffness is the main component of E . However, only the overall behavior of the ocular tissues can be assessed. The volume change ΔV was assumed to be proportional to the FPA, which enabled for calculation of a factor E_1 as measure of the mechanical properties of the eyeball based on the Friedenwald equation:

$$E_1 = (\log IOP_1 - \log IOP_2)/FPA. \quad (2.6)$$

This factor was calculated for all subjects and compared between the patients and the control group.

In the group of patients with POAG, FPA was lower ($3.21 \pm 0.98 \mu\text{m}$) than in the healthy control group ($3.99 \pm 0.94 \mu\text{m}$), which is in good agreement with the results of previous studies [1]. Also, the values of PA and POBF were lower in the patients than in the control subjects. The factor of structural stiffness E_1 , as calculated from FPA and PA, was significantly higher in the patients with POAG (0.0454 ± 0.0085) than in the control group (0.0427 ± 0.0058). In both study groups, E_1 was found to be independent of age, sex, systemic blood pressure and pulse rate.

The abnormally elevated factor E_1 found in this study indicates an increased ocular rigidity in patients with POAG. Theoretical calculations based on finite element modeling suggest that the mechanical properties of ocular tissues contribute to the susceptibility to alterations in IOP in different subjects [58]. Similar results were found in animal studies. In monkeys with glaucomatous damage induced by an experimental increase in IOP, altered biomechanical properties (increased scleral stiffnesses) were found compared with nonglaucomatous monkey eyes [59]. This means that an increase in IOP is less counterregulated by an increase in ocular volume, that leads, in turn, to a reduction in IOP. However, whether the increase in ocular structural stiffness is a primary contributing factor to glaucomatous ganglion cell damage or is a secondary effect of this damage has to be determined in future longitudinal studies.

Besides changes in ocular rigidity, also alterations in ocular blood flow, especially in the region of the ONH, are assumed to be involved in the pathogenesis of glaucoma. In one study, 90 patients with open angle glaucoma and 61 healthy subjects were evaluated [1]. Flow in the optic disk was assessed with scanning LDF. FPAs in the optic cup and the macula were assessed with the fundus pulsation interferometer. Blood flow in the optic cup (-46 per cent) and the neuroretinal rim (-18 per cent) was found to be considerably lower in patients with POAG than in the healthy control subjects. Also the measured FPA was lower in patients with glaucoma (-33 per cent in the optic cup and -24 per cent in the macula). A statistically significant correlation was found between blood flow in the cup as assessed with scanning LDF and FPAs at the same measurement site as assessed with the pulsation interferometer ($r = 0.55$ in glaucoma patients and $r = 0.52$ in healthy controls). Also an association was observed between the mean defect of the visual field and ocular hemodynamic parameters ($r = 0.46$ for blood flow and $r = 0.45$ for FPA at the cup). Hence, this study indicates not only a considerably reduced optic disk perfusion in patients with open-angle glaucoma, but, moreover, that the observed reduced blood flow is linked to visual field changes. Whether the compromised optic disk blood flow contributes to glaucomatous damage of this region or is a secondary phenomenon has still to be clarified. A more recent study also revealed an abnormal association between blood pressure and ocular perfusion in glaucoma patients, which indicates disturbed autoregulation of ocular blood flow in this disease [33].

2.5.4 Measurements in Age-related Macular Degeneration

In section 2.3.2 it has been mentioned that reduced blood flow in the choroid seems to be associated with the development of AMD. This hypothesis has gained support by studies using a wide variety of techniques for the assessment of choroidal perfusion. Friedman et al. found reduced flow velocities as assessed by CDI in the central retinal artery and the posterior ciliary arteries in patients with AMD compared to healthy controls [39]. Using ICG angiography, Ciulla et al. showed delayed and heterogenous filling of the choroid of patients with AMD [60]. A decrease in choroidal blood flow has also been found in studies based on LDF [61]. Furthermore, reduced POBF as assessed with pneumotonometry has been found.

Schmetterer et al. investigated local fundus pulsations in 12 AMD patients with subretinal neovascular membranes using the pulsation interferometer [2]. FPAs were measured directly on the membranes and adjacent to the membranes, referred to as 'inside' and 'outside' locations. Selection of the locations was based on fundus photographs and fluorescein angiographs. Furthermore, FPA measurements were performed in 12 healthy subjects at similar posterior pole positions. In AMD patients, FPAs were found to be significantly lower at the inside points (-26 per cent) than at the outside points. In healthy subjects, however, FPAs were considerably higher at the measurement sites corresponding to inside points (15 per cent). This means that in the healthy control group FPAs were higher in the macula than in peripheral parts of the fundus, which is in keeping with the results of previous studies [13]. The mechanism leading to reduced FPA at the membrane in AMD patients is not yet clear. In healthy subjects the predominant reflection at the posterior pole of the eye occurs most likely at Bruch's membrane. However, when measurements are performed in AMD patients directly at the neovascular membranes, changes in the fundus layers have to be taken into account. Breaks in Bruch's membrane caused by neovascularizations could strongly influence the ratio of re-emitted light from different fundus layers. Further studies are required to investigate if the reduced FPAs reflect a truly reduced pulsatile blood flow or may be attributed to changes in layer structure. Moreover, it has to be clarified if the ratio of pulsatile to non-pulsatile blood flow changes in neovascular membranes.

2.5.5 Measurements in Diabetic Retinopathy

In section 2.3.3 studies regarding retinal and choroidal blood flow in patients with diabetic retinopathy have been described. The current section focuses on the assessment of pulsatile choroidal blood flow in this disease via laser interferometric measurement of fundus pulsation.

Schmetterer et al. measured 214 eyes divided into four groups: (1) no retinopathy (control group), (2) background (not sight-threatening) retinopathy, (3) moderate to severe retinopathy, and (4) proliferative retinopathy [42]. Measurements were performed in the fovea, where the retina lacks vasculature and the FPA is only influenced by pulsatile choroidal blood flow. Between group 1 and 2 no considerable differences in FPA were found. In group 3 there was a tendency toward higher FPAs, which did not reach statistical significance, but, however, is in accordance with the results of a more recent study [43]. In patients with proliferative retinopathy (group 4) FPAs were significantly smaller than in all other study groups. These results suggest decreased choroidal blood flow in late stages of diabetic retinopathy, which is in good agreement with previous studies based on pneumotonometry [62]. The reduction in choroidal blood flow could be a factor in the development of neovascular proliferation due to a decreased oxygenation of the outer retina. All POBF studies in patients with diabetes are, however, hampered because flow pulsatility is possibly altered in the diabetic choroid [3].

2.5.6 Applications of LCTI

With the fundus pulsation interferometer introduced by Schmetterer the distance change between the front side of the cornea and the strongest reflecting structure at the posterior pole of the eye can be observed [13]. The predominant reflection in the retina of healthy subjects occurs – most likely – at Bruch’s membrane or the RPE. In several diseases, however, the layer structure can be disturbed. The origin of the strongest reflected wave is unclear in these cases. Moreover, in the region of the ONH it is very difficult to determine a single structure that can be associated with a predominant reflection. In contrast, LCTI enables for observation of the movement of reflective interfaces at well-defined and pre-selected axial positions. This can be helpful in patients where alterations in the layer structure of the retina are suspected, or where pulsations in the ONH region have to be observed. Also in healthy subjects, the depth-resolved LCTI measurements could give new insight into the biomechanics of the ocular tissues.

In healthy eyes the different retinal layers are assumed to move in parallel. With LCTI, one could proof if this hypothesis is true or if there are slight differences in the fundus pulsations of the retinal interfaces, e.g., due to retinal blood flow or differences in the elastic properties. This technique could also be used in clinical studies of ocular pathologies, e.g., in patients with macular edema, where a clear non-parallelism of the movement of the retinal layers is expected.

In humans, pulsations of the sclera are difficult to measure due to the high blood volume within the choroid. However, in experimental animals a scleral peak can be observed [63]. Measurement of the sclera with LCTI might, on the one hand, enable for observation of eye elongation during myopia development, and, on the other hand, be used to gain insight into POBF, since measurement of corneo-scleral distance can enable for more accurate estimation of changes in ocular volume due to the pulsatile inflow of blood.

Chapter 3

Principles of LCTI

In this chapter, first the basic principles of partial coherence interferometry (PCI) are explained. For this purpose, the interference of monochromatic and polychromatic light is described. In a next step, the application of interference of polychromatic light for the measurement of the eye length is explained. Then, the fundus pulsation interferometer, a technique for the laser interferometric observation of distance variations between the cornea and the strongest reflecting site of the ocular fundus, is presented. Eventually, based on dual beam PCI for the measurement of the eye length and on the pulsation interferometer, low coherence tissue interferometry (LCTI) is introduced as a technique for the assessment of distance changes between the cornea and pre-selected ocular layers.

3.1 Interference of Two Monochromatic Waves

The electric vector \mathbf{E} of a monochromatic field is represented by

$$\mathbf{E}(\mathbf{r}, t) = \text{Re}\{\mathbf{A}(\mathbf{r})e^{-i\omega t}\} = \frac{1}{2}[\mathbf{A}(\mathbf{r})e^{-i\omega t} + \mathbf{A}^*(\mathbf{r})e^{i\omega t}] \quad [64]. \quad (3.1)$$

Here the Cartesian components of \mathbf{A} are

$$A_x = a_1(\mathbf{r})e^{ig_1(\mathbf{r})}, \quad A_y = a_2(\mathbf{r})e^{ig_2(\mathbf{r})}, \quad A_z = a_3(\mathbf{r})e^{ig_3(\mathbf{r})}, \quad (3.2)$$

where a_j and g_j are real functions. For a plane wave the amplitudes a_j are constant, while the phase functions g_j are given by $g_j(\mathbf{r}) = \mathbf{k} \cdot \mathbf{r} - \delta_j$. \mathbf{k} is the propagation vector which points into the direction of the energy flow, the δ_j 's are the phase constants which determine the polarization state of the electromagnetic wave.

The intensity I of light is defined as the time average of the amount of energy that crosses a unit area in unit time perpendicular to the direction of propagation

$$I = v \langle w \rangle, \quad (3.3)$$

where v is the propagation velocity of the electromagnetic field and w is the energy density. Since the energy density is given by

$$w = \frac{\varepsilon}{4\pi} \mathbf{E}^2 = \frac{\mu}{4\pi} \mathbf{H}^2, \quad (3.4)$$

and the propagation velocity is given by

$$v = \frac{c}{\sqrt{\varepsilon\mu}}, \quad (3.5)$$

the intensity can be expressed as

$$I = \frac{c}{4\pi} \sqrt{\frac{\varepsilon}{\mu}} \langle \mathbf{E}^2 \rangle = \frac{c}{4\pi} \sqrt{\frac{\mu}{\varepsilon}} \langle \mathbf{H}^2 \rangle. \quad (3.6)$$

From 3.1,

$$\mathbf{E}^2 = \frac{1}{4} [\mathbf{A}^2 e^{-2i\omega t} + \mathbf{A}^{*2} e^{2i\omega t} + 2\mathbf{A} \cdot \mathbf{A}^*], \quad (3.7)$$

when taking the time average over an interval large compared with the period $T = 2\pi/\omega$,

$$\langle \mathbf{E}^2 \rangle = \frac{1}{2} \mathbf{A} \cdot \mathbf{A}^* = \frac{1}{2} [|A_x|^2 + |A_y|^2 + |A_z|^2] = \frac{1}{2} [a_1^2 + a_2^2 + a_3^2]. \quad (3.8)$$

When two monochromatic waves \mathbf{E}_1 and \mathbf{E}_2 are superposed at some point P , the total electric field at this point is

$$\mathbf{E} = \mathbf{E}_1 + \mathbf{E}_2, \quad (3.9)$$

and

$$\mathbf{E}^2 = \mathbf{E}_1^2 + \mathbf{E}_2^2 + 2\mathbf{E}_1 \cdot \mathbf{E}_2. \quad (3.10)$$

Defining

$$I_1 = \langle \mathbf{E}_1^2 \rangle, \quad I_2 = \langle \mathbf{E}_2^2 \rangle, \quad \text{and} \quad J_{12} = 2\langle \mathbf{E}_1 \cdot \mathbf{E}_2 \rangle, \quad (3.11)$$

the total intensity at P is

$$I = I_1 + I_2 + J_{12}. \quad (3.12)$$

J_{12} is called *interference term*. Let \mathbf{A} and \mathbf{B} be the complex amplitudes of the two waves \mathbf{E}_1 and \mathbf{E}_2 , respectively, where

$$A_x = a_1 e^{ig_1}, \text{ etc.}, \quad B_x = b_1 e^{ih_1}, \text{ etc.} \quad (3.13)$$

The phases g_j and h_j of the two waves will in general be different, since the waves travelled different paths to the point P . If in an experimental setup the same *phase difference* δ is introduced between the corresponding components, we have

$$g_1 - h_1 = g_2 - h_2 = g_3 - h_3 = \delta = \frac{2\pi}{\lambda_0} \Delta S, \quad (3.14)$$

where ΔS is the optical path length difference for the two waves, and λ_0 is the wavelength in vacuum. Expressing $\mathbf{E}_1 \cdot \mathbf{E}_2$ in terms of the complex amplitudes \mathbf{A} and \mathbf{B} yields

$$\begin{aligned} \mathbf{E}_1 \cdot \mathbf{E}_2 &= \frac{1}{4} [\mathbf{A} e^{-i\omega t} + \mathbf{A}^* e^{i\omega t}] \cdot [\mathbf{B} e^{-i\omega t} + \mathbf{B}^* e^{i\omega t}] \\ &= \frac{1}{4} [\mathbf{A} \cdot \mathbf{B} e^{-2i\omega t} + \mathbf{A}^* \cdot \mathbf{B}^* e^{2i\omega t} + \mathbf{A} \cdot \mathbf{B}^* + \mathbf{A}^* \cdot \mathbf{B}]. \end{aligned} \quad (3.15)$$

Thus, the interference term can be expressed as

$$\begin{aligned} J_{12} &= 2\langle \mathbf{E}_1 \cdot \mathbf{E}_2 \rangle = \frac{1}{2} [\mathbf{A} \cdot \mathbf{B}^* + \mathbf{A}^* \cdot \mathbf{B}] \\ &= a_1 b_1 \cos(g_1 - h_1) + a_2 b_2 \cos(g_2 - h_2) + a_3 b_3 \cos(g_3 - h_3) \\ &= (a_1 b_1 + a_2 b_2 + a_3 b_3) \cos \delta. \end{aligned} \quad (3.16)$$

It can be seen that the interference term depends on the amplitude components and on the phase difference of the two waves.

Two light beams polarized at right angles do not interfere, which can easily be verified from 3.16. Assuming the z -direction as propagation direction, the electric vector of the first wave to be in the x, z -plane, and that of the second wave in the y, z -plane, leads to

$$a_2 = 0, \quad b_1 = 0, \quad (3.17)$$

and, since we know from electromagnetic theory that light waves are transverse,

$$a_3 = 0, \quad b_3 = 0. \quad (3.18)$$

Thus, the interference term is 0 for the case of two orthogonally polarized waves.

In a next step we will calculate the intensity resulting from the superposition of two waves which are propagated in the z -direction, and are linearly polarized with the \mathbf{E} vectors in the x -direction. Inserting

$$a_2 = b_2 = a_3 = b_3 = 0 \quad (3.19)$$

into 3.8, 3.11 and 3.16 leads to

$$I_1 = \frac{1}{2}a_1^2, \quad I_2 = \frac{1}{2}b_1^2, \quad \text{and} \quad J_{12} = a_1b_1 \cos \delta = 2\sqrt{I_1I_2} \cos \delta. \quad (3.20)$$

Inserting into 3.12 yields the total intensity

$$I = I_1 + I_2 + 2\sqrt{I_1I_2} \cos \delta. \quad (3.21)$$

The maxima of intensity

$$I_{\max} = I_1 + I_2 + 2\sqrt{I_1I_2} \quad (3.22)$$

occur at

$$|\delta| = 0, 2\pi, 4\pi, \text{ etc.}, \quad (3.23)$$

the minima of intensity

$$I_{\min} = I_1 + I_2 - 2\sqrt{I_1I_2} \quad (3.24)$$

at

$$|\delta| = \pi, 3\pi, \text{ etc.} \quad (3.25)$$

In the case of $I_1 = I_2$, the total intensity is given as

$$I = 2I_1(1 + \cos \delta). \quad (3.26)$$

Using the addition theorem for $\cos(\alpha + \beta)$ with $\alpha = \beta$,

$$\cos(2\alpha) = \cos^2 \alpha - \sin^2 \alpha = 2 \cos^2 \alpha - 1, \quad (3.27)$$

leads to

$$I = 4I_1 \cos^2 \frac{\delta}{2}. \quad (3.28)$$

This expression shows that the intensity varies between $I_{\max} = 4I_1$ and $I_{\min} = 0$ for the case $I_1 = I_2$.

The same formulae can be used for the calculation of interference of natural unpolarized light, since the latter may be represented as a superposition of two incoherent beams linearly polarized at right angles to each other. The interference between the x - and y -components is then considered separately.

3.2 Interference of Two Partially Coherent Beams

In section 3.1 the interference of monochromatic light produced by a point source was treated. Light from a real physical source is never strictly monochromatic and such a source always has a finite extension, consisting of many elementary radiators (atoms). However, the field produced by a physical source can be expressed as the sum of strictly monochromatic waves. The concept of *coherence* is then introduced to measure the correlation that exists between the electromagnetic vibrations at different points P_1 and P_2 in the field. This measure of correlation must be related to the sharpness of interference fringes which would result when combining the vibrations from the two points, expecting sharp fringes when the correlation is high (*coherent* situation) and no fringes at all in the absence of correlation (*incoherent* situation). Usually neither of these situations is realized and the vibrations are called *partially coherent*.

In formula 3.1 we described the wave function of a monochromatic field as the real part of an associated complex wave function. Here we will again employ a complex representation for the description of polychromatic fields. In the following a real disturbance, e.g., a Cartesian component of the electric vector, at a certain point P in space is represented by the function $V^{(r)}(P, t)$. With $V^{(r)}(P, t)$ we associate the complex function

$$V(P, t) = \int_0^\infty a(P, \nu) e^{i[\phi(P, \nu) - 2\pi\nu t]} d\nu, \quad (3.29)$$

with $V^{(r)}(P, t) = \text{Re}\{V(P, t)\}$. For the study of the correlation between the vibrations at two arbitrary points in the wave field we analyse a two-beam interference experiment, where the light is produced by an extended polychromatic source σ (Fig. 3.1).

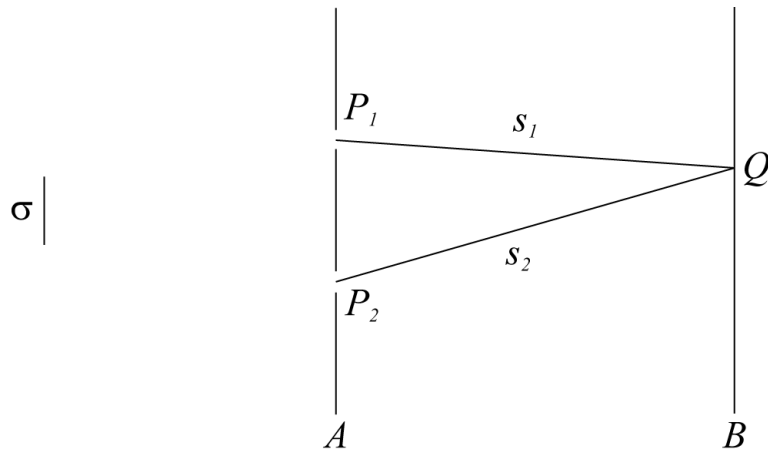


Figure 3.1: An interference experiment with polychromatic light from an extended source σ .

The observable intensity $I(P)$ is, apart from an inessential constant, equal to the mean value of $V^{(r)2}(P, t)$:

$$I(P) = 2\langle V^{(r)2}(P, t) \rangle \stackrel{\text{(see [64])}}{=} \langle V(P, t)V^*(P, t) \rangle. \quad (3.30)$$

For determining the interference effects arising on superposition of the vibrations from the points P_1 and P_2 we imagine an opaque screen A with pinholes at the respective points, and consider the intensity distribution on a second screen B in some distance from A , on the side

opposite the source. We assume the refractive index of the medium between the two screens as 1. The complex disturbance $V(Q, t)$ at the point Q is given by

$$V(Q, t) = K_1 V(P_1, t - t_1) + K_2 V(P_2, t - t_2). \quad (3.31)$$

The times t_1 and t_2 , which the light needs to travel from P_1 to Q and from P_2 to Q respectively, are

$$t_1 = \frac{s_1}{c}, \quad \text{and} \quad t_2 = \frac{s_2}{c}. \quad (3.32)$$

K_1 and K_2 are inversely proportional to s_1 and s_2 , and depend also on the size of the openings and the geometry of the setup. From the formulae 3.30 and 3.31 it follows that the intensity at Q is given by

$$I(Q) = K_1 K_1^* \langle V_1(t - t_1) V_1^*(t - t_1) \rangle + K_2 K_2^* \langle V_2(t - t_2) V_2^*(t - t_2) \rangle \\ + K_1 K_2^* \langle V_1(t - t_1) V_2^*(t - t_2) \rangle + K_2 K_1^* \langle V_2(t - t_2) V_1^*(t - t_1) \rangle, \quad (3.33)$$

where we employed the abbreviations $V_1(t) = V(P_1, t)$, etc. Assuming a stationary field allows us to shift the origin of time in all expressions in 3.33, e.g.,

$$\langle V_1(t - t_1) V_1^*(t - t_1) \rangle = \langle V_1(t) V_1^*(t) \rangle = I_1, \quad \text{etc.} \quad (3.34)$$

Thus, Eq. 3.33 can be simplified to

$$I(Q) = |K_1|^2 I_1 + |K_2|^2 I_2 + 2|K_1 K_2| \Gamma_{12}^{(r)} \left(\frac{s_2 - s_1}{c} \right), \quad (3.35)$$

where $\Gamma_{12}^{(r)}(\tau)$ is the real part of the function

$$\Gamma_{12}(\tau) = \langle V_1(t + \tau) V_2^*(t) \rangle. \quad (3.36)$$

$\Gamma_{12}(\tau)$ is called the *mutual coherence function* of the wave field. When the two points coincide ($P_1 = P_2$) we obtain

$$\Gamma_{11}(\tau) = \langle V_1(t + \tau) V_1^*(t) \rangle, \quad (3.37)$$

which is called the *self-coherence function* of the electromagnetic vibrations at P_1 .

$|K_1|^2 I_1$ is the intensity which would be observed at Q if the pinhole at P_1 alone were open; a similar interpretation holds true for $|K_2|^2 I_2$. Thus, in the following we will use the abbreviations

$$I^{(1)}(Q) = |K_1|^2 I_1 = |K_1|^2 \Gamma_{11}(0), \quad \text{and} \quad I^{(2)}(Q) = |K_2|^2 I_2 = |K_2|^2 \Gamma_{22}(0). \quad (3.38)$$

We also introduce the *complex degree of coherence* $\gamma_{12}(\tau)$ as:

$$\gamma_{12}(\tau) = \frac{\Gamma_{12}(\tau)}{\sqrt{\Gamma_{11}(0)} \sqrt{\Gamma_{22}(0)}} = \frac{\Gamma_{12}(\tau)}{\sqrt{I_1} \sqrt{I_2}}. \quad (3.39)$$

With the help of 3.38 and 3.39, the formula 3.35 can finally be written in the form

$$I(Q) = I^{(1)}(Q) + I^{(2)}(Q) + 2\sqrt{I^{(1)}(Q)} \sqrt{I^{(2)}(Q)} \gamma_{12}^{(r)} \left(\frac{s_2 - s_1}{c} \right), \quad (3.40)$$

where $\gamma_{12}^{(r)}$ is the real part of γ_{12} .

The formula 3.40 is the *general interference law for stationary optical fields*. According to this law, we must know the intensity of each beam and the value of the real part of the complex

degree of coherence in order to determine the intensity arising from the superposition of two beams. 3.40 also holds when the two interfering beams are derived from a primary beam, not by 'wave-front division' at P_1 and P_2 , but by 'amplitude division' close to a single point P_1 , for example in a Michelson interferometer. In this case $\gamma_{12}^{(r)}(\tau)$ is replaced by $\gamma_{11}^{(r)}(\tau)$.

The correlation functions $\gamma_{12}^{(r)}$ and $\Gamma_{12}^{(r)}$ can be determined from experiment. For this purpose one needs to measure the intensity $I(Q)$ as well as the intensities $I^{(1)}(Q)$ and $I^{(2)}(Q)$ from each pinhole separately. In terms of these observed values, $\gamma_{12}^{(r)}$ is, according to 3.40, given by

$$\gamma_{12}^{(r)} = \frac{I(Q) - I^{(1)}(Q) - I^{(2)}(Q)}{2\sqrt{I^{(1)}(Q)}\sqrt{I^{(2)}(Q)}}. \quad (3.41)$$

To determine $\Gamma_{12}^{(r)}$ one also has to measure the intensities $I(P_1)$ and $I(P_2)$ at each pinhole. $\Gamma_{12}^{(r)}$ is then given by

$$\Gamma_{12}^{(r)} = \sqrt{I(P_1)}\sqrt{I(P_2)}\gamma_{12}^{(r)} = \frac{1}{2}\sqrt{\frac{I(P_1)I(P_2)}{I^{(1)}(Q)I^{(2)}(Q)}}[I(Q) - I^{(1)}(Q) - I^{(2)}(Q)]. \quad (3.42)$$

To show the significance of γ_{12} we express 3.40 in a different way. We assume a mean frequency of the light $\bar{\nu}$ and write

$$\gamma_{12}(\tau) = |\gamma_{12}(\tau)|e^{i[2\pi\bar{\nu}\tau + \arg \gamma_{12}(\tau) - 2\pi\bar{\nu}\tau]} = |\gamma_{12}(\tau)|e^{i[\alpha_{12}(\tau) - 2\pi\bar{\nu}\tau]}, \quad (3.43)$$

where

$$\alpha_{12}(\tau) = 2\pi\bar{\nu}\tau + \arg \gamma_{12}(\tau). \quad (3.44)$$

Then Eq. 3.40 becomes

$$I(Q) = I^{(1)}(Q) + I^{(2)}(Q) + 2\sqrt{I^{(1)}(Q)}\sqrt{I^{(2)}(Q)}|\gamma_{12}(\tau)|\cos[\alpha_{12}(\tau) - \delta], \quad (3.45)$$

where the phase difference δ is given by

$$\delta = 2\pi\bar{\nu}\tau = \frac{2\pi}{\lambda}(s_2 - s_1). \quad (3.46)$$

The maximum value of $|\gamma_{12}(\tau)|$ is 1, in which case the intensity at Q is the same as would be obtained with strictly monochromatic light of wavelength $\bar{\lambda}$, and with a phase difference between the vibrations at P_1 and P_2 equal to $\alpha_{12}(\tau)$ (see Eq. 3.21). In this situation the vibrations at P_1 and P_2 are called *coherent*. If $|\gamma_{12}(\tau)|$ is zero, the last term in 3.45 is also zero, and the beams do not generate any interference effects. In this situation the vibrations are called *incoherent*. If $|\gamma_{12}(\tau)|$ lies between the two extreme values, i.e., if $0 < |\gamma_{12}(\tau)| < 1$, the vibrations are said to be *partially coherent*, $|\gamma_{12}(\tau)|$ representing their *degree of coherence*.

The intensity $I(Q)$ can also be represented in the form

$$I(Q) = |\gamma_{12}(\tau)|\{I^{(1)}(Q) + I^{(2)}(Q) + 2\sqrt{I^{(1)}(Q)}\sqrt{I^{(2)}(Q)}\cos[\alpha_{12}(\tau) - \delta]\} + [1 - |\gamma_{12}(\tau)|][I^{(1)}(Q) + I^{(2)}(Q)]. \quad (3.47)$$

Here, the terms in the first line may be considered to arise from *coherent* superposition of two beams of intensities $|\gamma_{12}(\tau)|I^{(1)}(Q)$ and $|\gamma_{12}(\tau)|I^{(2)}(Q)$ and of phase difference $\alpha_{12}(\tau) - \delta$, while those in the second line result from *incoherent* superposition of two beams of intensities

$[1 - |\gamma_{12}(\tau)|]I^{(1)}(Q)$ and $[1 - |\gamma_{12}(\tau)|]I^{(2)}(Q)$. The intensity at Q can therefore be regarded as a mixture of coherent and incoherent light, with intensities in the ratio

$$\frac{I_{\text{coh}}}{I_{\text{incoh}}} = \frac{|\gamma_{12}(\tau)|}{1 - |\gamma_{12}(\tau)|}, \quad (3.48)$$

or

$$\frac{I_{\text{coh}}}{I_{\text{tot}}} = |\gamma_{12}(\tau)|, \quad \text{with} \quad I_{\text{tot}} = I_{\text{coh}} + I_{\text{incoh}}. \quad (3.49)$$

The *fringe visibility* \mathcal{V} (contrast of the interference fringes) is defined as

$$\mathcal{V} = \frac{I_{\text{max}} - I_{\text{min}}}{I_{\text{max}} + I_{\text{min}}}. \quad (3.50)$$

From Eq. 3.45, the maximum and minimum intensities are

$$\begin{aligned} I_{\text{max}} &= I(Q) = I^{(1)}(Q) + I^{(2)}(Q) + 2\sqrt{I^{(1)}(Q)}\sqrt{I^{(2)}(Q)}|\gamma_{12}(\tau)|, \quad \text{and} \\ I_{\text{min}} &= I(Q) = I^{(1)}(Q) + I^{(2)}(Q) - 2\sqrt{I^{(1)}(Q)}\sqrt{I^{(2)}(Q)}|\gamma_{12}(\tau)|. \end{aligned} \quad (3.51)$$

Thus, if the two interfering waves have equal intensity, the fringe visibility \mathcal{V} in the corresponding interference pattern equals the degree of coherence:

$$\mathcal{V} = |\gamma_{12}(\tau)|. \quad (3.52)$$

The Wiener-Khintchine Theorem

The relation between the self-coherence function $\Gamma_{11}(\tau)$ of a light source and its *spectral density* $S(\nu)$, which is the contribution from the frequency range $(\nu, \nu + d\nu)$ to the intensity (also referred to as *power spectrum*), is obtained by the *Wiener-Khintchine theorem* [64], [65]. This theorem states that $\Gamma_{11}(\tau)$ and $S(\nu)$ form a Fourier transform pair:

$$S(\nu) = \text{FT}\{\Gamma_{11}(\tau)\} \quad \text{and} \quad \Gamma_{11}(\tau) = \text{FT}^{-1}\{S(\nu)\}. \quad (3.53)$$

Many light sources, including the sources usually employed in partial coherence interferometry, have an approximately Gaussian power spectrum,

$$S(\nu) \propto \exp\left[-4 \ln 2 \frac{(\nu - \nu_0)^2}{\Delta\nu^2}\right], \quad (3.54)$$

where $\Delta\nu$ is the FWHM. This is easily verified by calculating $S(\nu)$ at $\nu = \nu_0 \pm \frac{\Delta\nu}{2}$:

$$S(\nu_0 \pm \frac{\Delta\nu}{2}) \propto \exp\left[-4 \ln 2 \frac{(\nu_0 \pm \frac{\Delta\nu}{2} - \nu_0)^2}{\Delta\nu^2}\right] = e^{-\ln 2} = \frac{1}{2}. \quad (3.55)$$

The self-coherence function of such a light source is – according to the Wiener-Khintchine theorem – given by the inverse Fourier transform of the power spectrum,

$$\Gamma_{11}(\tau) = \int_{-\infty}^{\infty} S(\nu)e^{2\pi i\nu\tau} d\nu, \quad (3.56)$$

which leads to

$$\Gamma_{11}(\tau) \propto \exp\left[-\pi^2 \frac{\Delta\nu^2}{4 \ln 2} \tau^2 - 2\pi i\nu_0\tau\right]. \quad (3.57)$$

The *real envelope* $A(\tau)$ of the self-coherence function $\Gamma_{11}(\tau)$ is defined as $A(\tau) = 2|\Gamma_{11}(\tau)|$. For a light source with an approximately Gaussian power spectrum, the real envelope of the self-coherence function is

$$A(\tau) = 2|\Gamma_{11}| \propto \exp \left[- \left(\frac{\pi \Delta \nu}{2\sqrt{\ln 2}} \tau \right)^2 \right]. \quad (3.58)$$

3.3 Coherence Time and Coherence Length

In section 3.2, a physical light source was described as the sum of many elementary radiators (atoms). Light from such a source is made up of wave trains of finite length, of which a large number pass at random time intervals during the time required to make an observation. For simplicity, we assume in the following that all these wave trains are identical. If a wave train is split up into two trains, e.g., in a Michelson interferometer, and a path length difference is introduced between them, obviously only interference fringes can be observed due to pairs of wave trains derived from the *same* incident wave train. The wave trains derived from *different* incident wave trains arrive at random, and in rapid succession, and, thus, their contributions to the interference term average to zero over the relatively long time required to measure the intensity.

The light disturbance $F(t)$ due to a single wave train, at a point at time t , is – expressed as a Fourier integral – given by

$$F(t) = \int_{-\infty}^{\infty} f(\nu) e^{-2\pi i \nu t} d\nu, \quad (3.59)$$

where by the Fourier inversion theorem

$$f(\nu) = \int_{-\infty}^{\infty} F(t) e^{2\pi i \nu t} dt. \quad (3.60)$$

We assume F to be zero for $|t| \geq t_0$, so that the length of the wave train is $2t_0$. If N such wave trains pass the point during the time required to make an observation, the total light disturbance may be written as

$$V(t) = \sum_{n=1}^N F(t - t_n), \quad (3.61)$$

where the t_n 's are the times of arrival of the wave trains. The light intensity averaged over the time interval $2T$ required to make an observation is

$$I = \frac{1}{2T} \int_{-T}^T |V(t)|^2 dt \sim \frac{1}{2T} \int_{-\infty}^{\infty} |V(t)|^2 dt, \quad (3.62)$$

if T is large compared to the half-duration t_0 of each wave train. By using Eq. 3.61 and 3.62, it can be shown that the mean intensity is given by

$$I = \frac{N}{2T} \int_{-\infty}^{\infty} |f(\nu)|^2 d\nu, \quad (3.63)$$

i.e., it is proportional to the integral of the intensities $i(\nu) = |f(\nu)|^2$ (incoherent superposition) of the monochromatic components of which a single wave train is made up [64]. The relationship between the duration of the wave trains and the frequency range over which

the Fourier components have appreciable intensity can be illustrated by a simple example. Suppose a duration $\Delta t = 2t_0$ for each wave train, during which $F(t)$ is simply periodic with frequency ν_0 , i.e.,

$$F(t) = \begin{cases} f_0 e^{-2\pi i \nu_0 t} & \text{when } |t| \leq \frac{\Delta t}{2}, \\ 0 & \text{when } |t| > \frac{\Delta t}{2}, \end{cases} \quad (3.64)$$

where f_0 is constant. Inserting into Eq. 3.60 yields

$$\begin{aligned} f(\nu) &= f_0 \int_{-\frac{\Delta t}{2}}^{\frac{\Delta t}{2}} e^{2\pi i(\nu - \nu_0)t} dt \\ &= f_0 \Delta t \left[\frac{\sin \{ \pi(\nu - \nu_0)\Delta t \}}{\pi(\nu - \nu_0)\Delta t} \right]. \end{aligned} \quad (3.65)$$

The function $[\sin \{ \pi(\nu - \nu_0)\Delta t \} / \pi(\nu - \nu_0)\Delta t]^2$ (see Fig. 3.2) determines the intensity distribution of the Fourier components of 3.64. The frequency interval $\nu_0 \pm \Delta\nu/2$ over which the

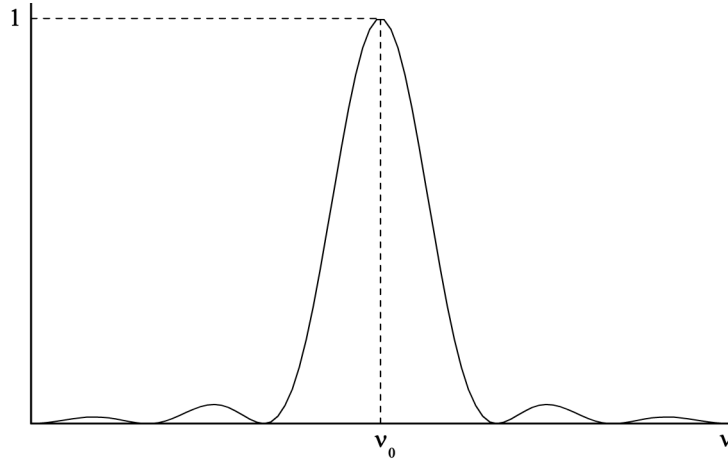


Figure 3.2: The function $\left[\frac{\sin \{ \pi(\nu - \nu_0)\Delta t \}}{\pi(\nu - \nu_0)\Delta t} \right]^2$.

intensity is appreciable can be estimated by finding the first zero of 3.65, which occurs at

$$\Delta\nu \sim \frac{1}{\Delta t}. \quad (3.66)$$

Thus, the effective frequency range of the Fourier spectrum is of the order of the reciprocal of the duration of a single wave train.

In real light sources the wave trains are not identical and of simple form as in 3.64. The loss of energy by atoms during emission results in damping of the wave trains. Furthermore, the thermal motion of the atoms leads to Doppler shifts in the observed spectra. However, it can be shown that a similar relation between Δt and $\Delta\nu$ holds true for light from physical sources:

$$\Delta t \Delta\nu \sim \frac{1}{4\pi}. \quad (3.67)$$

The time Δt is called the *coherence time* of the light. The *coherence length* Δl is defined by

$$\Delta l = c\Delta t \sim \frac{c}{\Delta\nu} = \frac{\bar{\lambda}_0^2}{\Delta\lambda_0}, \quad (3.68)$$

where $\bar{\lambda}_0$ is the mean wavelength and $\Delta\lambda_0$ is the FWHM bandwidth of the light source. For the observation of interference fringes the path difference between two beams (e.g., in

a Michelson interferometer) must be smaller than the coherence length of the light. When the difference of optical path is greater than the coherence length, interference effects are no longer appreciable.

For a Gaussian-shaped spectrum the coherence time Δt can be determined by calculating the FWHM duration of the self-coherence function $\Gamma_{11}(\tau)$ given in Eq. 3.57, which leads to

$$\Delta t = \frac{4 \ln 2}{\pi \Delta \nu}. \quad (3.69)$$

The corresponding coherence length is $c \cdot \Delta t$. Because of the backscattering configuration used in partial coherence interferometry, which implies that each path within the interferometer and the object under study is passed twice, we define the *round-trip coherence length* l_c as

$$l_c = \frac{c \cdot \Delta t}{2} = \frac{2 \ln 2}{\pi} \frac{\bar{\lambda}_0^2}{\Delta \lambda_0}. \quad (3.70)$$

3.4 Partial Coherence Interferometry

3.4.1 Basic Principles of Partial Coherence Interferometry

In the standard interferometric length measurement technique light of long coherence length is guided via a beam splitter cube (BSC) onto a fixed reference mirror and a measurement mirror (*Michelson interferometer*, see Fig. 3.3). The measurement mirror is moved over the

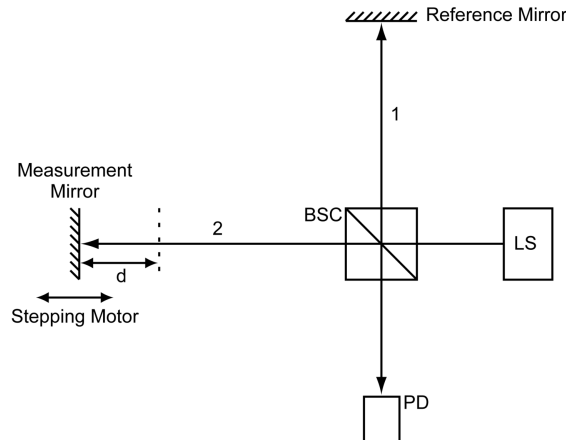


Figure 3.3: Interferometric length measurement using a coherent light source: d , distance to be measured; BSC, beam splitter cube; LS, coherent light source; PD, photodetector.

distance d to be measured. The distance d is obtained from the number of fringes N which pass the photodetector:

$$d = N \cdot \frac{\lambda}{2}. \quad (3.71)$$

However, since the measurement mirror cannot be moved across living structures, e.g., the eye, in medical applications this technique cannot be used. To overcome this problem, a technique called *partial coherence interferometry* has been introduced [18–21, 66].

In PCI light of high spatial coherence, but low temporal coherence, is used to obtain so-called *optical A-scans*, which are one-dimensional representations of the remitted light intensity

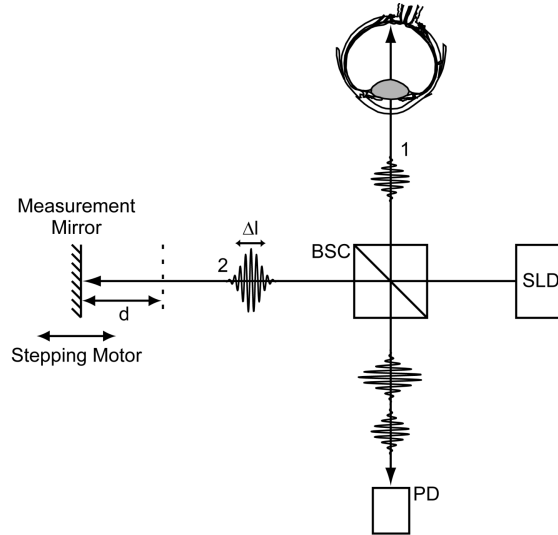


Figure 3.4: Partial coherence interferometer: d , position of the measurement mirror; BSC, beam splitter cube; SLD, superluminescent diode; PD, photodetector. Interference occurs if the position of the measurement mirror matches the position of a light remitting site within the object.

versus tissue penetration depth. Usually, an SLD is used for illumination of the object (see Fig. 3.4). The emitted light beam is split by a beam splitter cube into two components. One component is guided onto a measurement mirror, which is usually mounted on a stepping motor, while the other component is used for illumination of the object. This beam is reflected at light remitting sites within the object. The two beams returning from the measurement mirror and the object are recombined at the interferometer exit. According to Eq. 3.45, interferences will occur when the optical path lengths of the two beams are equal within the coherence length.

For calculation of the oscillating part $O(\tau)$ of the intensity, we introduce the *response function* $h(t)$ as the amplitude reflectivity of the sample, where t is related to the axial position z by the speed of light. The Fourier transform

$$H(\nu) = \text{FT}\{h(t)\} \quad (3.72)$$

is called the *transfer function* of the sample. The light disturbance $V_s(t)$ generated by the sample is

$$V_s(t) = \int_{-\infty}^{\infty} V(t')h(t-t') dt' = V(t) * h(t), \quad (3.73)$$

where $V(t)$ is the probe beam signal and the asterisk stands for convolution. According to Eq. 3.40, the oscillating part of the signal intensity at the interferometer exit is given by the real part of the mutual coherence function of the beam from the sample arm and the beam from the reference arm:

$$O(\tau) = 2 \text{Re}\{\langle V_s^*(t) \cdot V_r(t+\tau) \rangle\} = 2\Gamma_{sr}^{(r)}(\tau). \quad (3.74)$$

It follows from Eqs. 3.73 and 3.74 that the mutual coherence function $\Gamma_{sr}(\tau)$ is the convolution of the self-coherence function of the light source and the response function of the sample:

$$\Gamma_{sr}(\tau) = \Gamma_{11}(\tau) * h(\tau). \quad (3.75)$$

Thus, the oscillating part $O(\tau)$ can be expressed as

$$O(\tau) = 2 \operatorname{Re}\{\Gamma_{11}(\tau) * h(\tau)\} = 2 \operatorname{Re}\{\operatorname{FT}^{-1}\{S(\nu) \cdot H(\nu)\}\}, \quad (3.76)$$

where $S(\nu)$ is the power spectrum of the light source. If the sample consists of a plane mirror, $O(\tau)$ simplifies to $2\Gamma_{11}^{(r)}(\tau)$. It can be seen that the function $\Gamma_{11}^{(r)}(\tau)$ plays the role of a depth point-spread function. For a Gaussian spectrum we obtain

$$\Gamma_{11}^{(r)}(\tau) \propto \exp\left[-4 \ln 2 \left(\frac{z}{l_c}\right)^2\right] \cos\left(\frac{4\pi}{\lambda_0} z\right), \quad (3.77)$$

where $z = c \cdot \tau / 2$. The PCI signal represents the depth distribution of sample amplitude reflectivities convolved with the depth point spread function. Thus, the axial resolution of a PCI system is of the order of the round-trip coherence length l_c . The normalized point-spread function of a light source with a Gaussian spectrum and its real envelope are plotted in Fig. 3.5.

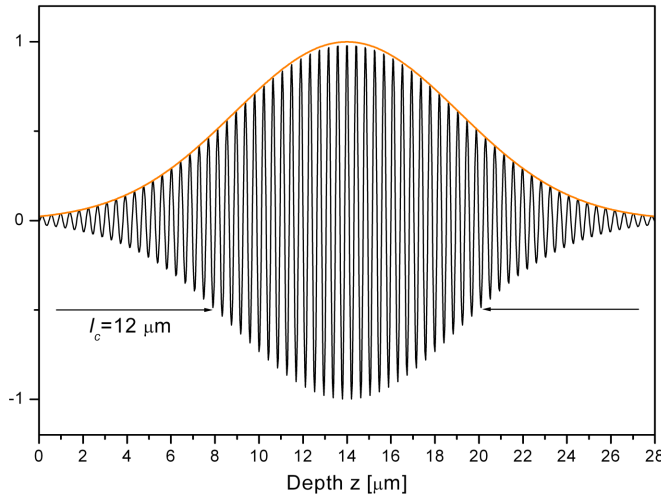


Figure 3.5: PCI depth point-spread function (black curve) and its real envelope (orange curve) for a light source with a Gaussian spectrum, a central wavelength λ_0 of 840 nm and a round-trip coherence length l_c of 12 μm .

The signal at the photodetector (PD), which is proportional to the intensity at the interferometer exit, is band-pass filtered, rectified, and low-pass filtered (see subsection 3.4.3). Hence, the resulting output signal is the envelope of the oscillating part of the intensity at the photodetector.

It follows that PCI can be used to measure optical distances within a (semi-) transparent object with an uncertainty equal to the round-trip coherence length l_c . Applications of this technique to measure the axial length in human eyes *in vivo* were reported by Fercher and Roth [22] and Fercher, Mengedocht, and Werner [23]. However, during the time needed to shift the reference mirror the measurement is sensitive to movements of the object under study. This becomes a major problem when measuring larger distances in living structures (e.g., longitudinal eye motions when measuring the axial eye length). To overcome this problem either a very fast moving reference mirror or the dual beam PCI technique has to be used [20, 21, 67, 68].

3.4.2 Dual Beam Partial Coherence Interferometry

In this technique the light beam of an SLD enters an external Michelson interferometer with unequal arm lengths (Fig. 3.6), which splits the beam into two coaxial components with a path length difference of twice the arm length difference d between the measurement and the reference mirror. This dual beam is directed onto the eye and reflected at the various sites,

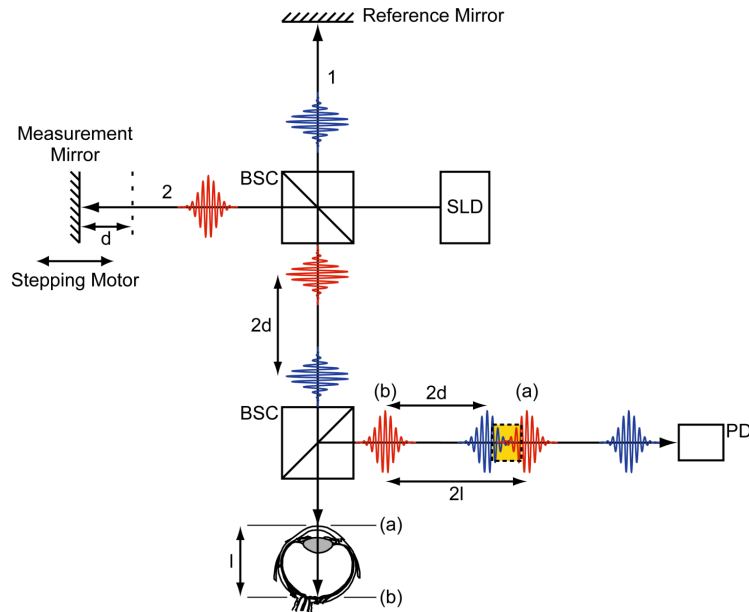


Figure 3.6: Dual beam partial coherence interferometer: d , arm length difference between measurement and reference mirror; l , eye length; BSC, beam splitter cube; SLD, superluminescent diode; PD, photodetector. Interference occurs if the arm length difference between measurement and reference mirror matches the axial eye length (see yellow rectangle).

which form boundaries separating regions of different refractive indices in the eye (see table 2.1). The predominant reflections occur at the anterior side of the cornea and at several retinal and choroidal layers, in particular the ILM, the RPE, and Bruch's membrane. Hence, each beam component is further split into subcomponents reflected at these interfaces. These reflected beams are then superimposed on the PD. If the optical distance between two ocular surfaces equals the arm length difference d , an interference signal is observed at the PD. This can be explained by taking a closer look at the time at which the various subcomponents of the beam reach the PD (Fig. 3.6): The light beam of the SLD is split up by the BSC into the components \mathbf{E}_1 and \mathbf{E}_2 . Both components are again split up at the reflecting sites of the eye, e.g., at the front side of the cornea (a) and the RPE (b), into the subcomponents $\mathbf{E}_1^{(a)}$, $\mathbf{E}_1^{(b)}$ and $\mathbf{E}_2^{(a)}$, $\mathbf{E}_2^{(b)}$, respectively. If the optical length of the eye matches the arm length difference d the two subcomponents $\mathbf{E}_2^{(a)}$ and $\mathbf{E}_1^{(b)}$ reach the PD without any time delay and will interfere. As can easily be seen, a longitudinal movement of the eye has no impact on the match between the interferometer arm length difference and the path lengths between the reflecting interfaces.

To measure intraocular distances, the measurement mirror of the Michelson interferometer is moved at constant speed. At any time the arm length difference d equals an optical distance within the eye, the respective subcomponents of the beam will interfere, leading to an interference signal at the PD. The real envelope of this signal is recorded as a function of d by a PC. Signal curves recorded in this way are called *optical A-scans*. From the

positions of the signal peaks in an A-scan, the respective optical distances within the eye can be determined directly. For calculation of the geometric distances, the optical distances have to be divided by the group refractive index n_g of the respective (intraocular) medium.

As in PCI, the resolution of this technique is of the order of l_c (FWHM of the signal peaks). However, the precision, i.e., the repeatability to which the positions of the signal peak maxima can be determined, and, thus, the precision to which intraocular distances can be measured, is usually better than the width of the signal peaks. Applications of the dual beam PCI technique *in vivo* have been reported for the measurement of distances in the anterior eye [69–72], the posterior eye [20, 67], and for the measurement of the axial eye length [73, 74]. This technique also forms the basis of the commercially available IOL master (Zeiss, Jena, Germany) for the measurement of the axial eye length.

3.4.3 Laser Doppler Partial Coherence Interferometry

Various noise sources, primarily speckle noise and $1/f$ noise, contribute to the interference signal in dual beam PCI. In order to achieve shot-noise limited detection the cross-correlation term of the interferometer signal is separated from the dc component by an optical heterodyne technique (i.e., the mixing of two frequencies). For this purpose one of the interferometer beams is used with a different frequency to produce a carrier frequency of the interference signal. Hence, the contributions of the various noise sources can be minimized by band-pass filtering.

The most straightforward way of realizing a heterodyne technique in optics is to use the Doppler effect. One of the interferometer mirrors is moved along the interferometer arm during data acquisition at constant speed v ; the same mirror simultaneously performs the depth scan. This movement produces a Doppler shift Δf of the light frequency of the beam. Since the path in the respective interferometer arm is passed twice, the beam leaving the Michelson interferometer has a Doppler shift corresponding to a velocity $2v$. Thus, the Doppler shift of the light frequency is given by:

$$\Delta f = 2f_0 \frac{v}{c} = 2 \frac{v}{\lambda_0}. \quad (3.78)$$

The intensity of the observed interference pattern, generated by the superimposed (shifted and non-shifted) beams, is modulated by Δf (heterodyne beat frequency). Thus, the corresponding signal from the PD is band-pass filtered with Δf as central frequency. Then the signal is rectified and low-pass filtered. Hence the output signal of the filter is the envelope of the oscillating part of the intensity at the PD.

3.4.4 Optical Coherence Tomography

The techniques of PCI and dual beam PCI form the basis of time domain optical coherence tomography (TD-OCT), a method of generating 2-dimensional images (referred to as *B-scans*) of (semi-) transparent objects out of a series of A-scans. In OCT, a scanning mirror is used to shift the probe beam to different lateral (transversal) positions of the object under study. In the conventional (i.e., longitudinal) scanning scheme, the position of the lateral scanning mirror is held constant during a single A-scan, and the B-scan is produced by recording a series of A-scans at various angles of the scanning mirror (see Fig. 3.7). In the transversal scanning scheme the probe beam is moved by the scanning mirror over the

lateral scanning range while holding the measurement mirror of the Michelson interferometer at the same longitudinal position. When using an x-y-scanning mirror, a series of en face scans (also called *C-scans*) can be recorded over a range of axial positions, resulting in a 3-dimensional data set of a selected region of the object under study [75]. While the

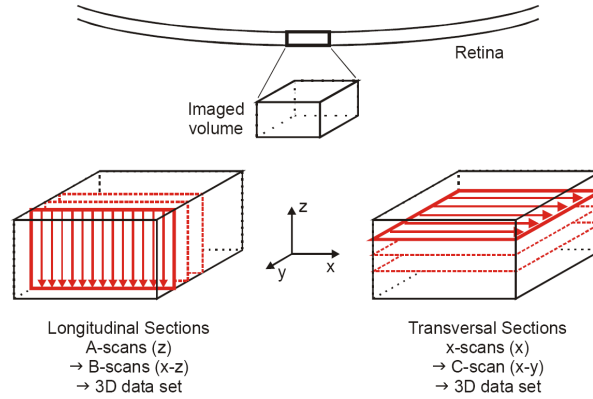


Figure 3.7: Comparison of conventional longitudinal scan pattern (*left*) and transversal scan pattern (*right*) [76].

conventional scanning pattern has the advantage of providing a carrier frequency for the interferometric signal, it also has a considerable disadvantage: it is not well adapted to the geometry of samples usually imaged with OCT. These samples have a much larger transversal extension (several mm) than achievable imaging depth (a few 100 μm), which means that for a 2- or 3-dimensional data set very large numbers of A-scans have to be recorded. For every A-scan the corresponding mirror has to be accelerated and decelerated, thus limiting the achievable imaging speed by (mechanical) inertia problems. For this reason, in recent systems the transversal scanning scheme in combination with an acousto optic modulator (AOM) for providing a carrier frequency for the interference signal is in use [76].

Fourier Domain Optical Coherence Tomography

In Fourier domain optical coherence tomography (FD-OCT) (also referred to as *frequency domain optical coherence tomography*) the probe is – similar to PCI – positioned in one arm of a Michelson interferometer and illuminated by an SLD. However, no mechanical depth scan is performed in FD-OCT. Instead, the light which exits the interferometer is dispersed by a spectrometer and its spectral distribution is recorded via a CCD line camera. Since the oscillating part of the intensity at the interferometer exit is a convolution of the illuminating beam with the light remitting structure of the sample (see Eqs. 3.74 and 3.75), and because of the Fourier transform relation between the spectrum of a light wave and its path-difference dependent degree of coherence (Wiener-Khintchine theorem, see section 3.2), the depth structure can be obtained by a Fourier transform of the measured spectrum. When using an x-y-scanning mirror, 2- or 3-dimensional data sets of an object can be generated by this method. FD-OCT has the advantages of shorter acquisition times (no longitudinal mechanical scanning required) and a higher signal to noise ratio (SNR) compared to TD-OCT. However, FD-OCT lacks the ability of dynamic focusing, which is required for OCT microscopy and various other applications. Recently, FD-OCT systems have been developed for the measurement of blood flow velocities in human retinal vessels by comparing the phase values of consecutively recorded A-scans [54, 77]. An example of a cross sectional image of a human macula recorded with ultrahigh-resolution FD-OCT is given in Fig. 3.8.

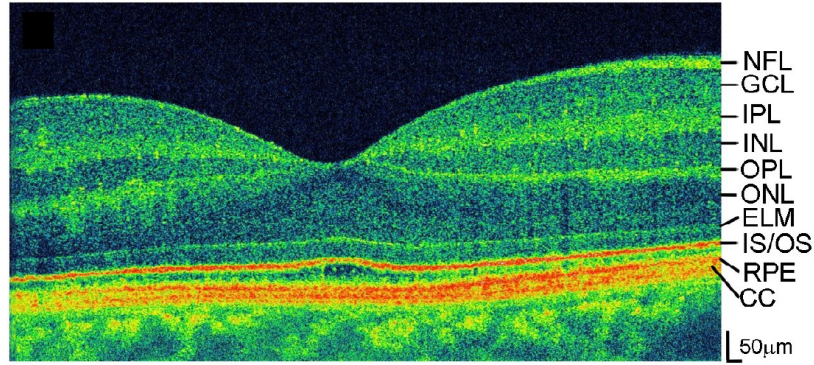


Figure 3.8: Ultrahigh-resolution FD-OCT image of human macula [78]. NFL, retinal nerve fiber layer; GCL, ganglion cell layer; IPL, inner plexiform layer; INL, inner nuclear layer; OPL, outer plexiform layer; ONL, outer nuclear layer; ELM, external limiting membrane; IS, inner segments; OS, outer segments; RPE, retinal pigment epithelium; CC, choriocapillaris.

3.5 Measurement of Ocular Fundus Pulsations

Several ocular diseases are associated with alterations in choroidal blood flow, such as age-related macular degeneration, glaucoma and diabetic retinopathy. Whereas the blood flow in retinal vessels can be measured by LDV (see section 2.4.4), choroidal blood vessels are very difficult to access since they are located behind the outer retina. Different techniques were proposed to gain insight into choroidal blood flow based on angiography [8], LDF [9], pneumotometry [10], and color Doppler imaging of the posterior ciliary arteries [11]. A method first described by Fercher [12] for the laser interferometric assessment of the pulsatile portion of the choroidal blood flow is presented in this section.

3.5.1 The Fundus Pulsation Interferometer

In this technique the eye is illuminated by a collimated laser beam of long coherence length [13]. At the anterior side of the eye four reflections corresponding to the four Purkinje images occur. These images originate from the light beams reflected at the outer (anterior) and the inner (posterior) surface of the cornea and the lens, respectively. The reflection from the front surface of the cornea is the most prominent. At the posterior pole of the eye the predominant reflection originates most likely from the RPE or Bruch's membrane. The wave originating from the front surface of the cornea is close to spherical, while the wave reflected from the fundus is plane. These two waves generate concentric circular interference fringes, similar to Newton's fringes, with a maximum of the contrast at approximately 30-40 mm in front of the eye, depending on the test subject [5]. However, only the interferogram resulting from the strongest reflection of the posterior pole of the eye is observable by this technique. Whereas other interferogram systems may also arise from other retinal interfaces, they are not visible.

Distance variations between the cornea and the retina lead to a change in interference order $\Delta N(t)$ and, therefore, can be determined by counting the fringes moving inward and outward through a fixed point. The change in optical distance $\Delta L(t)$ can then be calculated by

$$\Delta L(t) = \Delta N(t) \frac{\lambda}{2}, \quad (3.79)$$

where λ is the wavelength of the light source. The maximum distance change during the cardiac cycle is called fundus pulsation amplitude (FPA).

The plane of optimal contrast is imaged by a lens onto a LCCD, which is positioned in the center of the interference fringes. Each readout of the LCCD is captured by a PC and plotted along the time axis, resulting in a so-called *synthetic interferogram* covering information on the time course of changes in corneo-retinal distance. By counting the fringes moving inward and outward, the change of interference order $\Delta N(t)$ can be drawn as a function of time resulting in a contraction-dilatation graph (see Fig. 3.9).

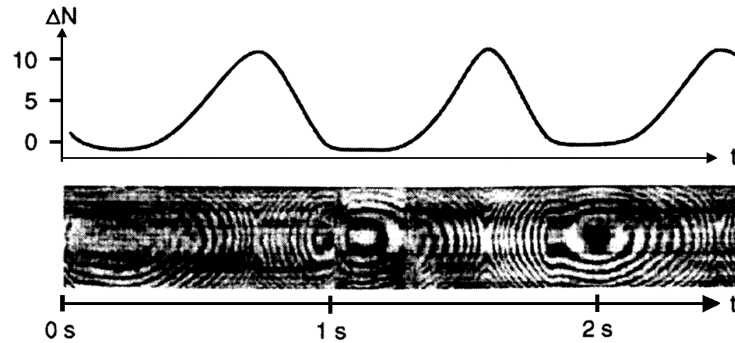


Figure 3.9: Synthetic interferogram consisting of consecutive readouts of an LCCD placed in the center of the interference fringes and the respective contraction-dilatation graph. Each change in interference order corresponds to a change in optical distance of $\lambda/2$.

The interference fringes generated by the light reflected from the cornea and the retina cannot be recorded using a point detector and a normal fringe counting technique. First, local irregularities in the interference fringes due to speckle phenomena from the retina hamper the use of this method. Moreover, the interference pattern can be disturbed by saccades (rapid eye movements) that last 20-50 ms, which cannot easily be identified using a point detector. Therefore an LCCD is used for the time-resolved detection of the interference fringes.

A sketch of the system presented by Schmetterer in [13] is depicted in Fig. 3.10. In this

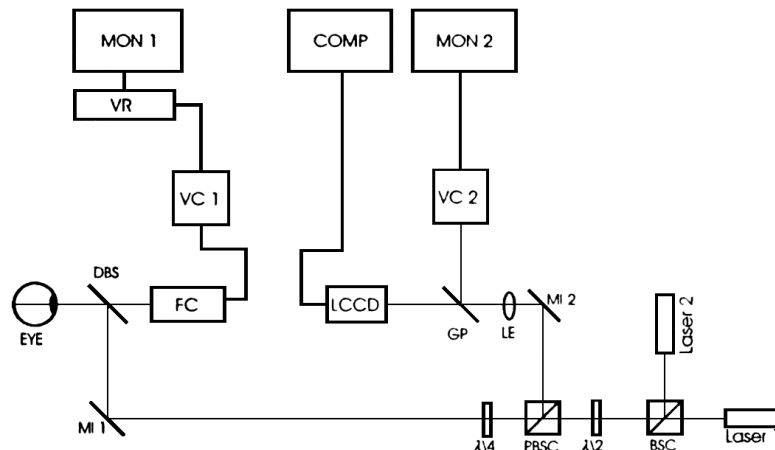


Figure 3.10: Optical scheme of the pulsation interferometer and its coupling to the fundus camera: BSC, beam splitter cube; $\lambda/2$ and $\lambda/4$, half- and quarter-wave plates; PBSC, polarizing beam splitter cube; MI 1 and MI 2, mirrors; DBS, dichroitic beam splitter; FC, fundus camera; VC 1 and VC 2, video cameras; VR, video recorder; MON 1 and MON 2, video monitors; LE, lens; GP, glass plate; LCCD, linear CCD array.

system a long coherent laser diode with a wavelength of 783 nm is used for the measurement

(Laser 1). The second laser diode (Laser 2), which emits visible light at a wavelength of 670 nm, is used for the adjustment of the instrument relative to the patient's eye so that the beam enters the eye at the center of the pupil. The two laser beams are combined by a BSC. The polarizing beam splitter cube (PBSC) is used in combination with a half-wave plate ($\lambda/2$) and a quarter-wave plate ($\lambda/4$) to reduce losses in transmitted and reflected light, respectively. The light is directed via a dichroitic beam splitter (DBS) mounted in the front of the objective of a fundus camera (FC) onto the patient's eye. The DBS is predominantly reflecting for infrared light (more than 95% at 783 nm) and highly transmitting for the white light of the FC. Using this setup, a small portion (less than 5%) of the measurement light reflected from the cornea and the retina passes into the FC, which allows for an online inspection of the point of incidence of the laser beam at the retina with a high-IR-sensitivity camera (VC 1). The image of the fundus is recorded with a video recorder (VR) to control the point of incidence during the measurement. The light reflected by the DBS is guided via the PBSC toward the detection unit, consisting of the LCCD and a video camera (VC 2). This setup enables for the measurement of ocular fundus pulsations at pre-selected transversal positions of the retina (see section 2.5).

3.5.2 Low Coherence Tissue Interferometry

The fundus pulsation interferometer described in the previous section allows only for the observation of the strongest reflecting retinal layer. However, for several applications, e.g., the study of macular edema or the observation of eye elongation during myopia development, it is required to measure other retinal or choroidal layers [79].

In order to allow for measurements of time-resolved distance changes between the front surface of the cornea and pre-selected retinal or choroidal layers the following approach is employed. LCTI comprises a dual beam PCI system for the measurement of axial eye length. In the detection arm an additional beam splitter is introduced and part of the light is directed towards a CCD array, whereas the other part of the light is directed towards the APD for the measurement of intraocular distances. This allows for the real-time assessment of tissue pulsations as long as the optical distances between the two interferometer arms and the optical distance between the two ocular surfaces are within the coherence length of the light source. Hence, the corresponding layer is pre-selected by the position of the mirrors within the Michelson interferometer.

The measurement process comprises two steps: First, an eye length measurement is performed on the test subject. The peak positions (corresponding to intraocular layers) of the signal curve are determined automatically by a search algorithm, and are displayed on the front panel of the graphical programming interface LabView, starting with the strongest reflecting layer. By selecting any of the peaks, the stepper motor is driven to that position. In the second step, the flip mirror is turned out of the optical path, and the plane ≈ 30 mm in front of the eye is imaged onto the LCCD. The signal from the LCCD is recorded by a PC and displayed in LabView. Since the relative movement between the retinal layers and the cornea is smaller than the coherence length time-resolved recording is possible. The optical setup of the LCTI system is described in detail in chapter 4.

Chapter 4

Optical Setup

In this chapter the optical setup of the LCTI system is described. The system components and specifications as well as the digital filtering of the captured data are explained. Furthermore, laser safety is discussed in terms of the maximum power of laser light applicable to the human eye.

4.1 Overview

The optical setup of the LCTI system is depicted in Fig. 4.1. As light source an SLD from Superlum, Russia with a central wavelength λ_0 of 840 nm and an FWHM bandwidth $\Delta\lambda_0$ of 26.8 nm, resulting in a round-trip coherence length l_c of 11.6 μm (in air, see Eq. 3.70), was used. The beam diameter of the system, which is determined by the focal length of the used fiber collimator (HPUCO-23-850-S-6.2AS, OZ Optics) and the numerical aperture of the connected fiber (SM800-5.6-125, Thorlabs) (see chapter 5), was calculated to be 0.98 mm. For optimizing the polarization to reduce losses in the PBSC, the fiber polarization controller FPC030 from Thorlabs was used in the entrance path, and, on the path to and from the sample, the polarization of the beam was rotated by 90° by a quarter-wave plate.

The typical FPA, e.g., the maximum distance change between cornea and retina, is in the order of 2-6 μm , which is considerably below the coherence length l_c of the light source. Hence, the changes in the interference pattern caused by ocular fundus pulsation are visible as long as the stepper motor is in a position corresponding to an intraocular layer of the subject's eye. The plane ≈ 30 mm in front of the cornea is imaged via two lenses L1 and L2 onto the APD and the CCD camera ($f_1 = 30$ mm and $f_2 = 80$ mm). By using this setup L1 is positioned as close to the origin of the interference pattern as possible so that the losses due to the divergent corneal reflection are minimized.

For the length measurement, the stepper motor is moved at a constant velocity v of 2.88 mm/s, resulting in a Doppler shift Δf of 6840 Hz (see Eq. 3.78). The signal from the APD is filtered electronically by a bandpass filter with a central frequency matching Δf . For readout of the signal, the data acquisition card PCI-6034E from National Instruments was used. After data acquisition the signal is digitally filtered in LabView. The sensitivity of the system for the length measurement was measured to be 87 dB. For the observation of fundus pulsations a CCD line-camera (Sony ILX551, 2048 pixels, 14x14 μm pixel size, 8 bit resolution) was used. Via a pellicle (8R/92T), small part of the light was guided onto a video camera (VC). Once

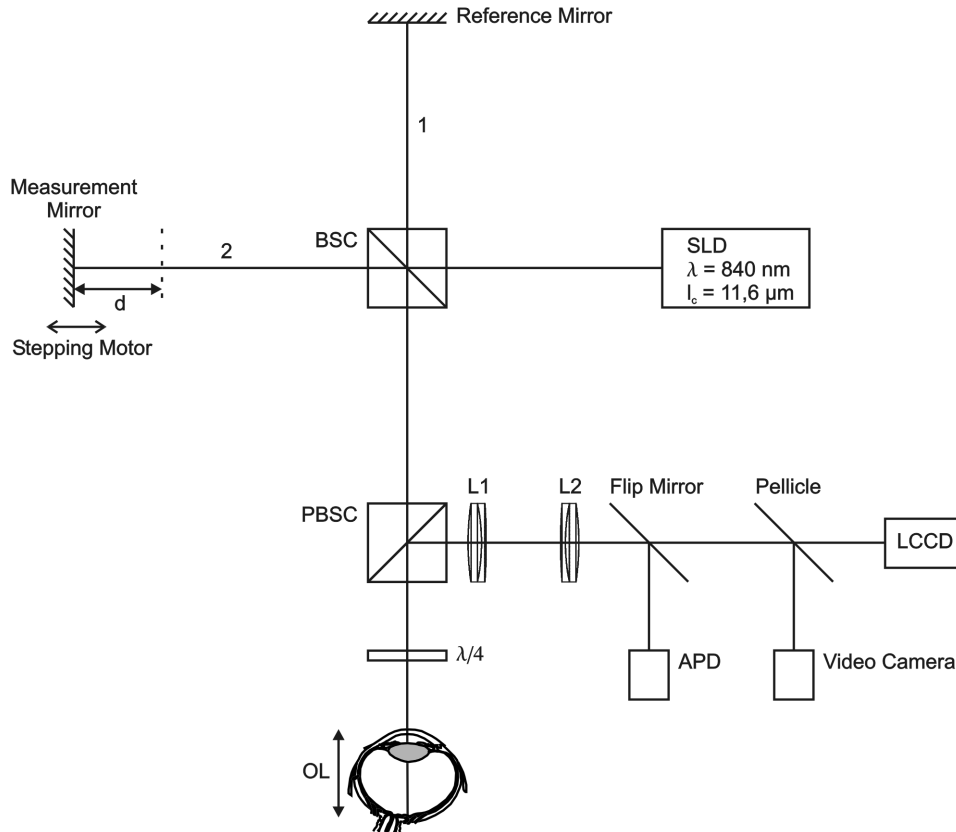


Figure 4.1: Optical setup of the LCTI system. SLD, superluminescent diode; BSC, beam splitter cube; PBSC, polarizing beam splitter cube; APD, avalanche photo diode; LCCD, linear CCD array. Depth ranging is provided by a scanning mirror. After positioning the measurement mirror according to the depth of an intraocular layer, the interference pattern is observed via a video camera and recorded over time by a linear CCD camera, resulting in a synthetic interferogram.

the subject was correctly positioned - so that the interference fringes could be observed on the video monitor - the signal was recorded with the linear CCD array operated at a line readout rate of 300-700 Hz.

For online inspection of the fundus pulsations in LabView, a background subtraction for elimination of internal reflections and static interference patterns from the subject's eye was performed. For the calculation of the background intensity a moving average $MA(m)$ was calculated for each pixel position m using the recursive formula

$$MA(m) = \frac{I(m) + MA_{n-1}(m) \cdot (N - 1)}{N}, \quad (4.1)$$

where $I(m)$ is the current intensity of the respective pixel. For N values between 500 and 700 have been chosen. The advantage of this method is the effective removal of static and almost static background signals at a relatively low computational effort, leading to no significant delay in online inspection.

Pictures of the optical setup of the LCTI system and the detection unit are given in Figs. 4.2 and 4.3.

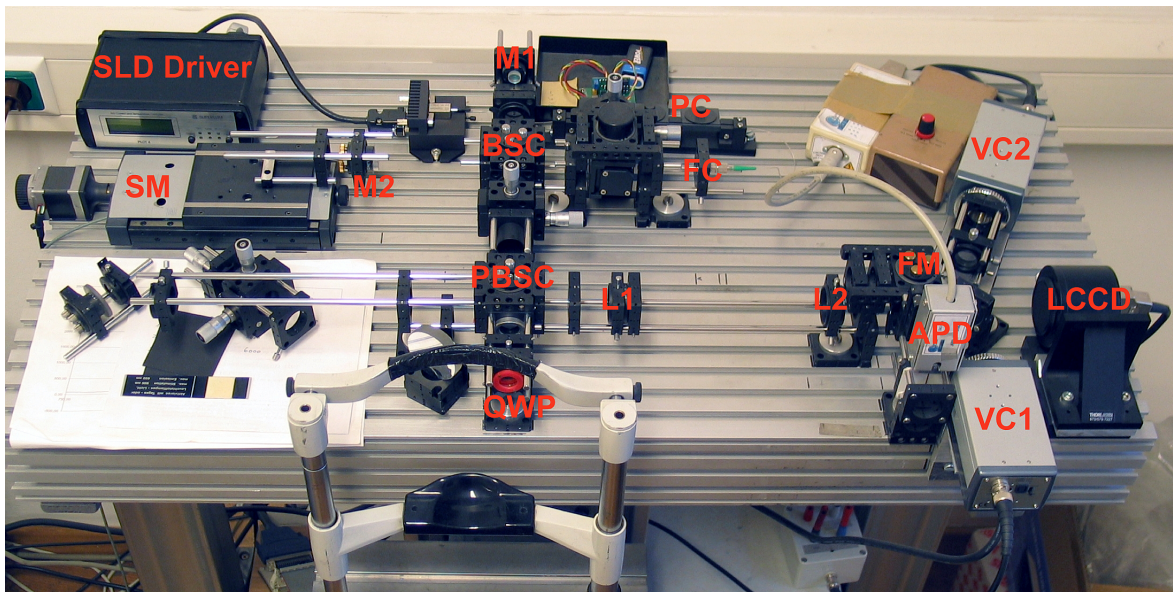


Figure 4.2: LCTI system including Michelson interferometer for interferometric length measurement and fundus pulsation interferometer. SM, stepping motor; M2 and M1, mirrors; BSC, beam splitter cube; PC, polarization controller; FC, fiber collimator; PBSC, polarizing beam splitter cube; QWP, quarter-wave plate; L1 and L2, lenses; FM, flip mirror; APD, avalanche photo diode; VC1 and VC2, video cameras; LCCD, linear CCD array.

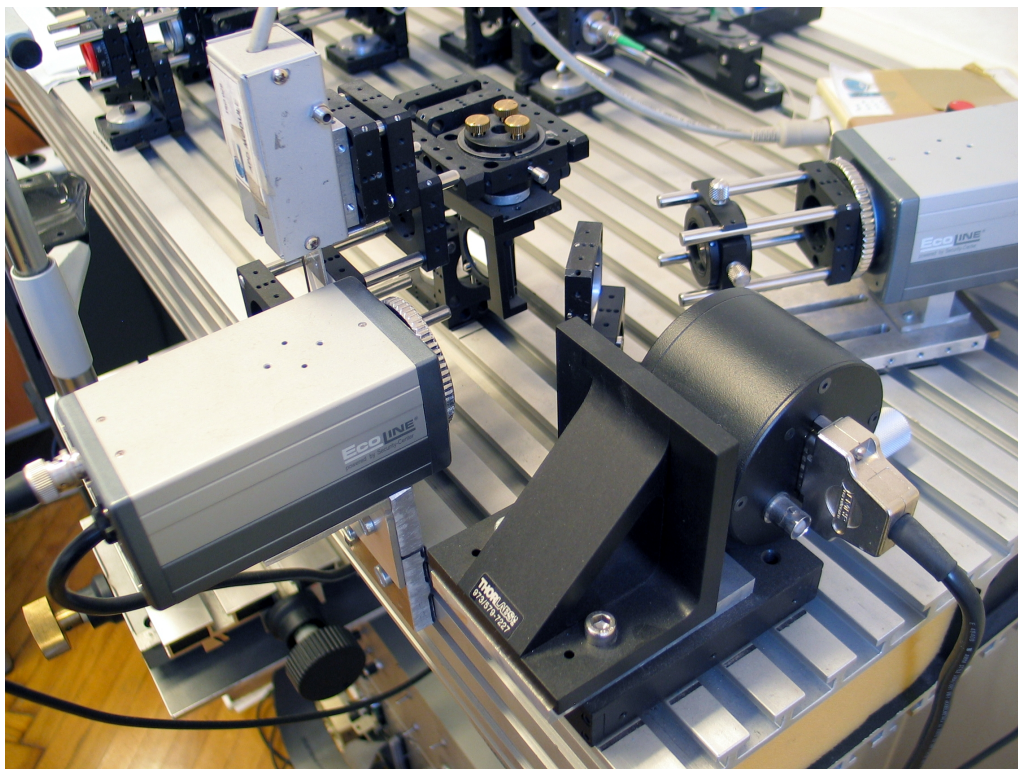


Figure 4.3: Detection unit of the LCTI system including APD module, LCCD camera, flip mirror, pellicle and video cameras for the observation of the plane of the APD fiber and the interference fringes, respectively.

4.2 Digital Filtering

As mentioned before, the signal from the APD is filtered electronically by a bandpass filter with a central frequency equaling f_D and read out via a data acquisition card. An additional filtering step is performed in LabView. For this purpose, first a fast Fourier transform (FFT) is performed on the acquired signal. A certain frequency range, that is determined by the bandwidth of the light source $\Delta\lambda_0$ and the Doppler shift f_D , is selected from the Fourier-transformed signal and an inverse FFT is applied. Using this method increases the SNR by approximately 3 dB (see Fig. 4.4).

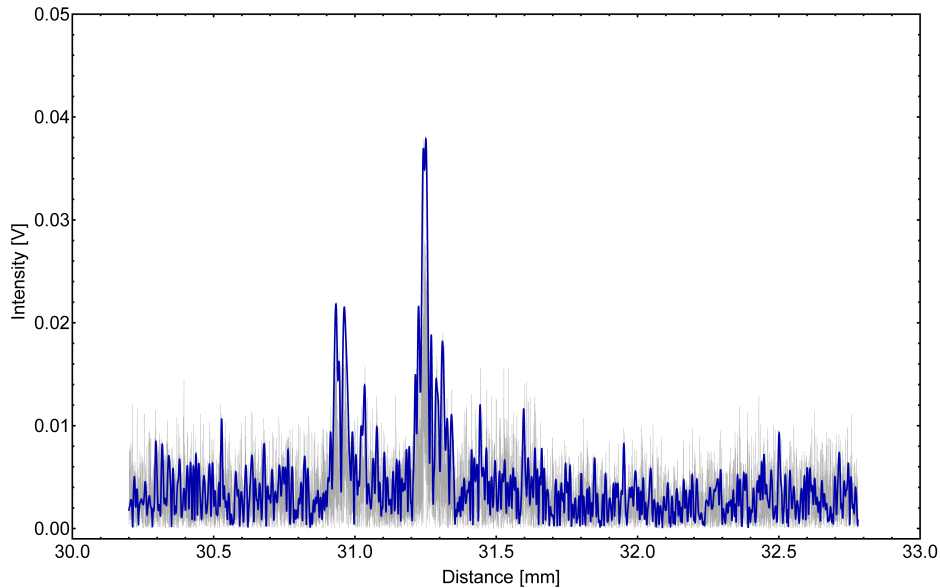


Figure 4.4: A-scan with digital filtering (blue) and without digital filtering (gray) recorded from a healthy subject at 11° to the axis of vision.

4.3 Laser Safety

The use of lasers or similar light sources (e.g., the SLDs used in the PCI or LCTI setups) always involves the risk of eye injury, since even small amounts of laser light can lead to permanent retinal damage. To control this risk, various specifications have been issued, for example ANSI Z136.1 [80]. These specifications define several 'classes' of lasers, depending on their power and wavelength λ , ranging from Class 1 (no risk of eye damage) to Class 4 (high risk of skin burn, eye damage, and ignition of combustible materials). Compared to light from other sources, laser light usually has a small divergence angle, which – in combination with the focusing mechanism of the eye – means that it can be concentrated into an extremely small spot on the retina, leading to a high risk of *thermal damage* (burn). However, lasers of moderate and high powers can even be hazardous to the eye when they have a larger divergence angle, e.g., when they are reflected diffusely.

Visible and near infrared laser radiation (400-1400 nm) can cause heating and, thereby, thermal damage of the retina, while laser radiation with wavelengths less than 400 nm and greater than 1400 nm is largely absorbed by the cornea and lens, leading to cataracts or burn injuries. Since the protective 'blink reflex' reaction is only triggered by visible light, the use of infrared lasers is particularly risky. Besides thermal damage, laser radiation with short wavelengths

Table 4.1: Pathological effects of laser light

wavelength	pathological effects
< 315 nm	corneal burn
315-400 nm	clouding of the eye lens (cataract)
400-1400 nm	photochemical damage to the retina, thermal burn
> 1400 nm	corneal burn, cataract

can also cause *photochemical damage* (destructive chemical reactions in tissue triggered by light). Photochemical damages can accumulate if the eye is exposed to the radiation over a longer time. Table 4.1 shows the pathological effects of laser radiation in different wavelength ranges.

The maximum permissible exposure (MPE) is the highest power of a laser beam at a certain wavelength λ , exposure duration t and spot size on the retina r that is considered safe (no risk of damage). However, since a precise measurement of the beam properties on the retina is impossible, its characteristics at the cornea are used to set the limits for the MPE. Assuming a maximum pupil diameter of 7mm and, furthermore, that the incident beam covers the whole pupil, assures that even in the 'worst case' (i.e., smallest spot size on the retina) the maximum power is not exceeded.

According to the specifications for the safe use of lasers issued by the American National Standards Institute (ANSI Z136.1 [80]) the MPE is given by

$$\text{MPE} = C_A \times 10^{-3}, \quad (4.2)$$

with

$$C_A = 10^{2(\lambda-0.700)}, \quad (4.3)$$

where λ is the central wavelength of the light source in μm . A central wavelength $\lambda = 840 \text{ nm}$ and an aperture area of 38.48 mm^2 leads to an MPE of $733 \mu\text{W}$ for exposure durations longer than 10 sec. In the current setup the energy delivery to the sample is $\approx 500\text{-}600 \mu\text{W}$, which is substantially below the MPE. Although the output power of the SLD is much higher ($\approx 7\text{-}8 \text{ mW}$), only a small portion of the light reaches the eye. This is mainly due to the losses in the optical isolator, the fiber couplers, and the BSC.

Chapter 5

Application of DOE

In LCTI and dual beam PCI the interference pattern generated by light beams reflected at the front surface of the cornea and the retina is measured. The wave originating from the cornea is spherical, which leads to a loss of signal on the way to the detector. Matching the divergencies of the waves reflected from the cornea and the retina by a *diffractive optical element (DOE)* enables for collecting as much light as possible and for improving signal to noise ratio and sensitivity [67, 68]. The DOE, also referred to as *Fresnel lens*, focuses one part of the light onto the cornea while the other part remains unchanged and is focused by the optical system of the eye onto the retina.

In this chapter, the interference pattern as well as the resulting fringe contrast and spacing will be calculated for an LCTI system with DOE. Advantages and disadvantages of the use of a DOE will be discussed.

5.1 Gullstrand's Eye Model

The calculations in this chapter are based on Gullstrand's eye model [24]. In this model, the eye is imagined as a number of spherical surfaces with different curvatures and distances as well as media of different refractive indices between these surfaces. The properties of the ocular components according to the Gullstrand eye are given in table 5.1. Together with ray transfer matrix analysis (see next section), this model allows for determination of the imaging properties of the eye.

Table 5.1: Properties of the ocular components in Gullstrand's eye model

interface	radius R [mm]	distance d [mm]	refractive index n
anterior cornea	7.8	0.55	1.3771
posterior cornea	6.5	3.05	1.3774
anterior lens	10.2	4	1.42
posterior lens	-6	16.59655	1.336
retina	-13.4		

5.2 Calculation of Fringe Contrast and Spacing with DOE

5.2.1 Ray Transfer Matrix Analysis

The contrast and spacing of the observed interference fringes in a dual beam PCI system with built-in DOE was calculated using *ray transfer matrix analysis*, which is based upon the *paraxial approximation* of geometric optics. This approximation holds true for rays that make small angles (α) to the optical axis of the system and lie close to this axis. This allows for the following approximations (when expressing α in radians) for calculation of the beam's path:

$$\sin(\alpha) \approx \alpha, \quad \cos(\alpha) \approx 1 \quad \text{and} \quad \tan(\alpha) \approx \alpha. \quad (5.1)$$

In ray transfer matrix analysis the optical system is described by a matrix. The light path through the system is then calculated by multiplying this matrix with the vector representing the light ray. Two planes – referred to as *input* and *output* planes – are defined, each orthogonal to the optical axis of the system. The (positive) optical axis is usually defined as running from left to right. A light ray entering the system and crossing the input plane in a distance x_1 from the optical axis at an angle α_1 is represented by the vector:

$$\begin{pmatrix} x_1 \\ \alpha_1 \end{pmatrix}. \quad (5.2)$$

The vector in the output plane can be calculated by multiplying the incident vector by the matrix \mathbf{M} representing the system:

$$\begin{pmatrix} x_2 \\ \alpha_2 \end{pmatrix} = \mathbf{M} \cdot \begin{pmatrix} x_1 \\ \alpha_1 \end{pmatrix} = \begin{pmatrix} A & B \\ C & D \end{pmatrix} \cdot \begin{pmatrix} x_1 \\ \alpha_1 \end{pmatrix}. \quad (5.3)$$

An example of propagation in free space over a distance d is given in Fig. 5.1 (x_n is positive when the ray lies above the optical axis z). The parameters of the ray in the output plane,

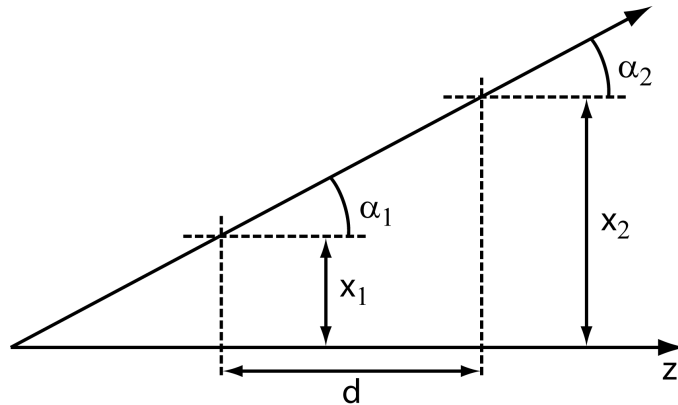


Figure 5.1: Translation of a beam in ray transfer matrix analysis.

x_2 and α_2 , can be calculated in paraxial approximation by:

$$\begin{aligned} x_2 &= x_1 + \alpha_1 d \\ \alpha_2 &= \alpha_1. \end{aligned} \quad (5.4)$$

Thus, the transfer matrix for propagation in free space or in a medium of constant refractive index can be expressed as:

$$\mathbf{M} = \begin{pmatrix} 1 & d \\ 0 & 1 \end{pmatrix}. \quad (5.5)$$

Table 5.2: Ray transfer matrices of main optical elements

matrix	abbreviation	element
$\begin{pmatrix} 1 & d \\ 0 & 1 \end{pmatrix}$	$\mathbf{M}_T(d)$	propagation in a medium of constant refractive index d , distance
$\begin{pmatrix} 1 & 0 \\ 0 & \frac{n_1}{n_2} \end{pmatrix}$	$\mathbf{M}_R(n_1, n_2)$	refraction at plane interface n_1 , refractive index of first medium n_2 , refractive index of second medium
$\begin{pmatrix} 1 & 0 \\ 0 & 1 \end{pmatrix}$	$\mathbb{1}_2$	reflection by a plane mirror Identity matrix
$\begin{pmatrix} 1 & 0 \\ -\frac{1}{f} & 1 \end{pmatrix}$	$\mathbf{M}_L(f)$	refraction by a thin lens f , focal length
$\begin{pmatrix} 1 & 0 \\ -\frac{2}{R} & 1 \end{pmatrix}$	$\mathbf{M}_M(R)$	reflection by a curved mirror R , radius of curvature ($R > 0$ for concave)
$\begin{pmatrix} 1 & 0 \\ \frac{n_1-n_2}{R \cdot n_2} & \frac{n_1}{n_2} \end{pmatrix}$	$\mathbf{M}_I(R, n_1, n_2)$	refraction at a curved interface R , radius of curvature ($R > 0$ for convex) n_1 , refractive index of first medium n_2 , refractive index of second medium

A series of optical elements is realized by multiplication of the respective matrices. Therefore, the transfer matrix \mathbf{M}_s of a system consisting of n elements can be calculated by:

$$\mathbf{M}_s = \mathbf{M}_n \cdot \mathbf{M}_{n-1} \cdot \dots \cdot \mathbf{M}_3 \cdot \mathbf{M}_2 \cdot \mathbf{M}_1. \quad (5.6)$$

The beam is always considered to be running along the positive optical axis (from left to right). Hence, a reflection of the light beam is implemented by changing the angle of the ray to the optical axis and multiplying the optical elements of the return path in the reverse order.

The ray transfer matrices of important optical elements are given in table 5.2.

5.2.2 Fringe Contrast

A light ray entering a DOE is partially refracted, another part is transmitted without any change of the ray. Hence, six beam components contribute to the measured interference pattern in a dual beam PCI system with built-in DOE:

1. \mathbf{E}_1 , the beam component that is refracted by the DOE, reflected by the cornea, and refracted again by the DOE on the return path. \mathbf{E}_1 can be approximated by a spherical wave, except when the distance d between the DOE and the anterior surface of the cornea equals the focal length f of the DOE or when d equals $f - R$, where R is the radius of curvature of the cornea. In these cases, \mathbf{E}_1 can be approximated by a plane wave. This is explained in detail in the next paragraph.
2. \mathbf{E}_2 , the beam component that is transmitted by the DOE, refracted by the eye and reflected by the retina, and on the way back again refracted by the cornea and transmitted by the DOE. \mathbf{E}_2 is a plane wave, similar as in dual beam PCI when no DOE is applied.

3. \mathbf{E}_3 , the beam component that is first refracted by the DOE, reflected by the cornea, and transmitted by the DOE on the way back. It can be approximated by a spherical wave.
4. \mathbf{E}_4 , the beam component that first passes the DOE unaltered, is refracted by the eye, reflected by the retina, and on the return path refracted by the eye and the DOE. Since this beam part is focused by the DOE in a plane that lies within the area where the contrast will be calculated, an approximation of \mathbf{E}_4 by a spherical wave would cause an infinite expression. Thus, \mathbf{E}_4 is approximated by a Gaussian beam of the form:

$$E_{4,x}(\rho, z) = A_0 \frac{w_0}{w(z)} e^{-(\rho/w(z))^2} e^{-ik\rho^2/2R(z)} e^{-i(kz-\eta(z))}, \quad E_{4,y}(\rho, z) = 0, \quad (5.7)$$

where ρ is the distance from the central axis (propagation direction) and z the corresponding coordinate (cylindrical coordinates). The *spot size* or *beam width* $w(z)$ is given by:

$$w(z) = w_0 \sqrt{1 + \left(\frac{z}{z_0}\right)^2}, \quad (5.8)$$

where z_0 is the *Rayleigh length*, which is the distance along the z -axis from the smallest beam diameter to the place where the area of the cross section of the beam doubles. The Rayleigh length determines the size of the near field of a Gaussian beam and becomes smaller when the beam is more focused. It is related to the *beam waist* w_0 by:

$$w_0 = \sqrt{\frac{z_0 \lambda}{\pi}}. \quad (5.9)$$

The *radius of curvature* $R(z)$ of the wave-fronts comprising the beam is related to the Rayleigh length by:

$$R(z) = z\{1 + (z_0/z)^2\}. \quad (5.10)$$

$\eta(z)$ is the *Gouy phase* (also called *longitudinal phase delay*) of the beam:

$$\eta(z) = \arctan z/z_0. \quad (5.11)$$

As the interference pattern will be calculated in a region close to the z -axis, and the wave-fronts of the Gaussian beam are orthogonal to this axis, the component $E_{4,z}(\rho, z)$ will be neglected in the following ($E_{4,z}(\rho, z) \approx 0$).

5. \mathbf{E}_5 and \mathbf{E}_6 , the parts that are transmitted by the DOE, reflected by the cornea and either refracted (\mathbf{E}_5) or transmitted (\mathbf{E}_6) on the return path.

From the beam components that are refracted by the DOE, only the part that is reflected by the cornea plays a role in the fringe pattern, since the other part is not focused on the retina and, thus, the backreflection is very weak compared to the other beam parts.

The DOE that was applied in this work had a focal length f of 70 mm and refracted about 40 per cent of the light. These values are used in the calculations in this chapter. The radius of curvature of the cornea R was taken as 7.8 mm, according to Gullstrand's eye model.

The beam entering the DOE is running parallel to the optical axis (z -axis) and, thus, can be described by:

$$\mathbf{x}_1 = \begin{pmatrix} x_1 \\ 0 \end{pmatrix}. \quad (5.12)$$

A refraction by the DOE can be described by multiplication of the beam with the corresponding ray transfer matrix $\mathbf{M}_L(f)$:

$$\mathbf{M}_L(f) \cdot \mathbf{x}_1 = \begin{pmatrix} 1 & 0 \\ -\frac{1}{f} & 1 \end{pmatrix} \cdot \begin{pmatrix} x_1 \\ 0 \end{pmatrix}. \quad (5.13)$$

The part of the beam associated to \mathbf{E}_1 , which is the component that is refracted by the DOE, reflected by the cornea, and refracted again by the DOE, can therefore be expressed as:

$$\mathbf{x}'_1 = \mathbf{M}_L(f) \cdot \mathbf{M}_T(d) \cdot \mathbf{M}_M(R) \cdot \mathbf{M}_T(d) \cdot \mathbf{M}_L(f) \cdot \mathbf{x}_1. \quad (5.14)$$

This leads to:

$$\mathbf{x}'_1 = \frac{1}{fR} \begin{pmatrix} (fR + 2d(f - R - d))x \\ 2(d - f)(d - f + R)x/f \end{pmatrix}. \quad (5.15)$$

At a position p in respect to the DOE the beam can be described by:

$$\mathbf{x}''_1 = \begin{pmatrix} x''_1 \\ \alpha''_1 \end{pmatrix} = \mathbf{M}_T(p) \cdot \mathbf{x}'_1. \quad (5.16)$$

The position p' where the beam \mathbf{x}''_1 crosses the z -axis can be found by solving the equation $x''_1 = 0$, leading to:

$$p' = \frac{f}{2} \left(1 + \frac{d}{d-f} + \frac{f}{d-f+R} \right). \quad (5.17)$$

p' is independent of x_1 (i.e., the distance of the incident beam from the z -axis), because of the focusing of the beam by the DOE. The intersection point p_1 in respect to the cornea is given by $p_1 = p' + d$, and forms the origin of the spherical wave used to approximate \mathbf{E}_1 . In Fig. 5.2, p_1 is plotted for values of d between 40 and 90 mm in front of the cornea. As can

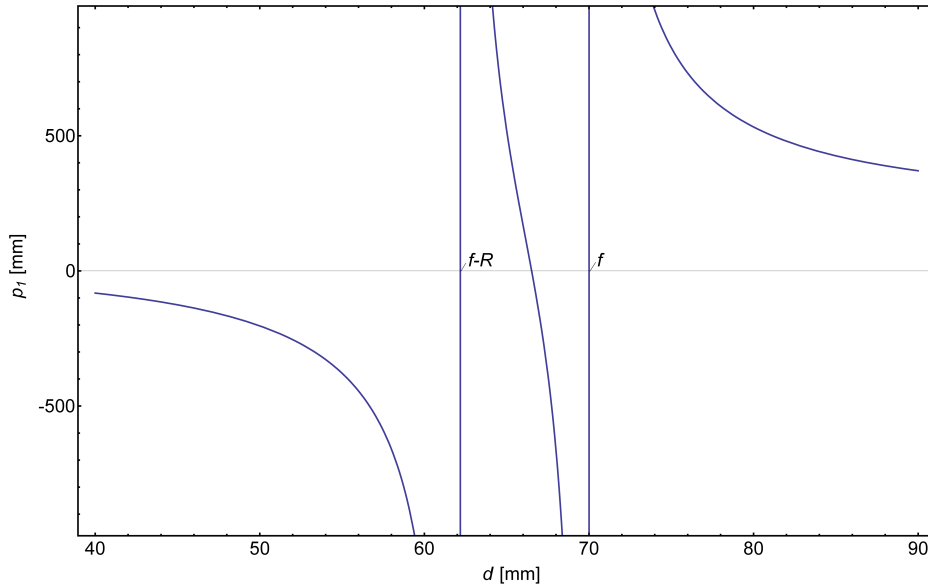


Figure 5.2: Origin of the spherical wave \mathbf{E}_1 for distances d between 40 and 90 mm.

be seen, p_1 becomes infinite for $d = f$ and $d = f - R$, which is in accordance with the fact that in these cases \mathbf{E}_1 is a plane wave running parallel to the optical axis. However, since the interference pattern is not observable when the two main waves \mathbf{E}_1 and \mathbf{E}_2 are plane, only the case $d < f - R$ will be examined in the following calculations, i.e., the case in which the DOE lies closer to the anterior surface of the cornea than $f - R$. Thus, \mathbf{E}_1 can be written as:

$$E_{1,x}(r') = A_1 \frac{r'(0, 0, 0)}{r'(x, y, z)} e^{ikr'(x, y, z)}, \quad E_{1,y}(r') = 0 \quad (5.18)$$

with

$$r'(x, y, z) = \sqrt{x^2 + y^2 + (z - p_1)^2}. \quad (5.19)$$

The amplitude A_1 is determined by the reflection coefficient of the cornea and the fraction of the light that is refracted by the DOE. Close to the z -axis it can be assumed $E_{1,z}(r') \approx 0$, since the wave-fronts are perpendicular to this axis.

\mathbf{E}_2 is a plane wave and can be written as:

$$E_{2,x}(z) = A_2 e^{ikz}, \quad E_{2,y}(z) = 0, \quad E_{2,z}(z) = 0. \quad (5.20)$$

A_2 depends on the reflection coefficient of the retina and the fraction of the light that is transmitted by the DOE.

The part of the beam associated to \mathbf{E}_3 , which is the component that is refracted by the DOE, reflected by the cornea, and transmitted by the DOE on the return path, can be written as:

$$\mathbf{x}'_3 = \mathbf{M}_T(d) \cdot \mathbf{M}_M(R) \cdot \mathbf{M}_T(d) \cdot \mathbf{M}_L(f) \cdot \mathbf{x}_3. \quad (5.21)$$

The origin p_3 of the spherical wave \mathbf{E}_3 is found in the same way as for \mathbf{E}_1 , leading to:

$$p_3 = \frac{-2d^2 + 2d(f - R) + fR}{2d - 2f + R}. \quad (5.22)$$

\mathbf{E}_3 is written in the same manner as \mathbf{E}_1 , replacing p_1 by p_3 .

\mathbf{E}_4 represents the beam component that is first transmitted by the DOE, reflected by the posterior pole of the eye, and refracted by the DOE on the way back. Hence, this component is a plane wave until it reaches the DOE on the return path, where it is then focused into a distance f . The point of intersection with the optical axis is given by $p_4 = f + d$. p_4 lies within the region where the fringe contrast will be calculated. Thus, a description of \mathbf{E}_4 by a spherical wave would lead to an infinite intensity. To avoid this infinity a Gaussian beam is used to describe \mathbf{E}_4 . The beam waist $w_{0,4}$ of \mathbf{E}_4 is determined by the wavelength, the focal length of the DOE and the beam waist $w_{0,0}$ of the incident beam (see D. Meschede, *Optik, Licht und Laser*, p. 57):

$$w_{0,4} \approx \frac{\lambda f}{\pi w_{0,0}} = 0.019 \text{ mm} \quad (5.23)$$

with $\lambda = 840 \text{ nm}$, $f = 70 \text{ mm}$, and $w_{0,0} \approx 1 \text{ mm}$ (see next paragraph). The remaining parameters of the beam are described in Eqs. 5.8 to 5.11.

The beam waist $w_{0,0}$, i.e., the diameter of the incident beam where the intensity drops to $1/e^2$ (≈ 13.5 per cent) compared to the intensity at the center, is given by (see also Fig. 5.3):

$$w_{0,0} = 2 \cdot f \cdot \text{NA}, \quad (5.24)$$

where f is the focal length of the used fiber collimator and NA is the numerical aperture of the fiber. The definition of NA is based on a drop of a factor $1/e^2$ of the center intensity. In the current setup the fiber collimator HPUCO-23-850-S-6.2AS (OZ Optics) with a focal length f of 6.2 mm is connected to the single-mode fiber SM800-5.6-125 (Thorlabs) with a numerical aperture NA of 0.12 (product data sheet, based on drop to 1 percent), which corresponds to an NA of 0.0791 based on a drop to 13.5 per cent. This leads to a beam waist $w_{0,0}$ of 0.98 mm.

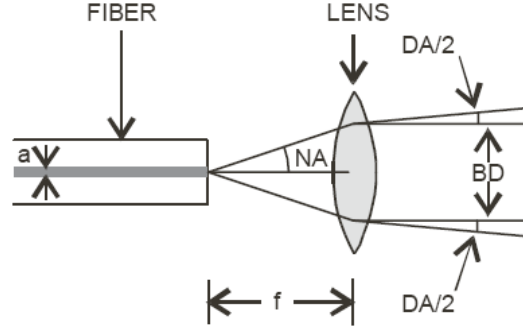


Figure 5.3: Principle of a fiber collimator: a, core diameter of the fiber; NA, numerical aperture; f, focal length of the lens; DA, divergence angle; BD, beam diameter (from: OZ Optics).

The part of the beam associated to \mathbf{E}_5 , which is the component that is transmitted by the DOE, reflected by the cornea, and refracted by the DOE on the return path, can be written as:

$$\mathbf{x}'_5 = \mathbf{M}_L(f) \cdot \mathbf{M}_T(d) \cdot \mathbf{M}_M(R) \cdot \mathbf{M}_T(d) \cdot \mathbf{x}_5. \quad (5.25)$$

The origin p_5 of the spherical wave \mathbf{E}_5 is found in the same way as for \mathbf{E}_1 , leading to:

$$p_5 = \frac{f(2d + R)}{2d - 2f + R}. \quad (5.26)$$

\mathbf{E}_6 is approximated by a spherical wave with its origin at $p_6 = -R$.

The intensity of the generated interference pattern is given by:

$$I(x, y, z) \propto |E_{1,x}(x, y, z) + \dots + E_{6,x}(x, y, z)|^2. \quad (5.27)$$

The amplitudes A_1, \dots, A_6 depend on the fraction of the light that is refracted $r_d = \sqrt{0.4}$ or transmitted $t_d = \sqrt{0.6}$ by the DOE and the reflection coefficient of the cornea ρ_c and the retina ρ_r , respectively:

$$A_1 = r_d^2 \rho_c, \quad A_2 = t_d^2 \rho_r, \quad A_3 = r_d t_d \rho_c, \quad A_4 = t_d r_d \rho_r, \quad A_5 = t_d r_d \rho_c, \quad A_6 = t_d^2 \rho_c. \quad (5.28)$$

The ratio of the reflection coefficient of the cornea and the reflection coefficient of the retina was assumed to be $\rho_c/\rho_r = 6$. A plot of the intensity $I(x, y, z)$ for $z = 20$ mm and for values of x between -0.60 and 0.60 mm is given in Fig. 5.4 (solid line). The distance d of the DOE with respect to the cornea was assumed to be 45 mm. The dashed line in Fig. 5.4 represents the intensity of the static interference pattern caused by the beam components originating from the cornea ($\mathbf{E}_1, \mathbf{E}_3, \mathbf{E}_5$, and \mathbf{E}_6). For comparison, the interference pattern in a system without DOE is shown (blue dotted line).

It can be seen from Fig. 5.4 that the beam parts stemming from the cornea form an interference pattern that has almost the same intensity as the interferences between retinal and corneal beam components. Therefore, the static interferences (i.e., contributions to the observed intensity pattern that do not depend on the distance between cornea and retina) are predominant in the system with DOE. This does not hamper the eye length measurement due to the bandpass filter incorporated in the system. The observation of fundus pulsations, however, becomes very difficult when applying a DOE, since even very small eye movements lead to changes of the observed 'background' intensity on the linear CCD camera.

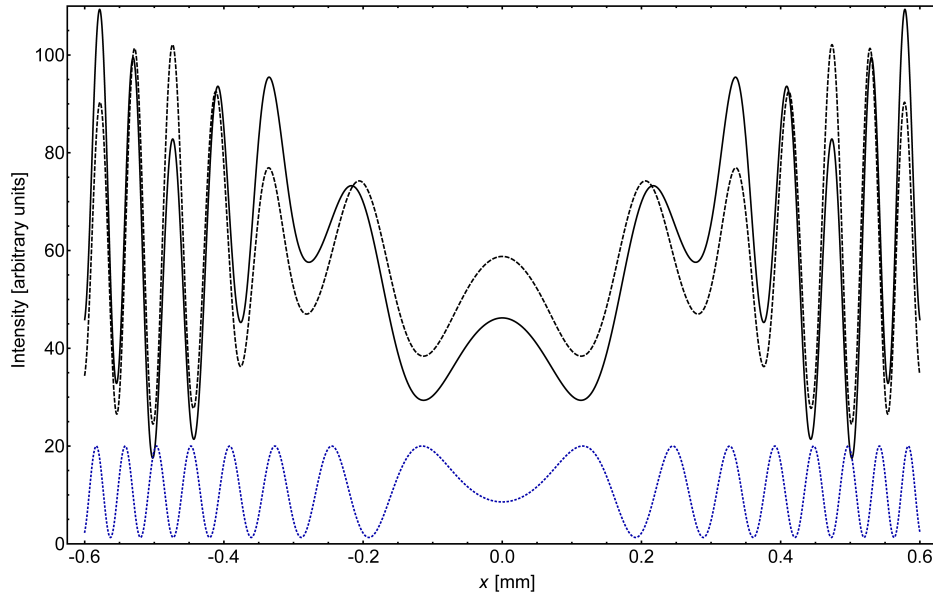


Figure 5.4: Interference pattern in a system with DOE (solid line) and static interference pattern of the beams originating from the cornea (dashed line). For comparison, interference pattern in a system without DOE (blue dotted line).

The contrast of the interference pattern was calculated for distances from the cornea z from 0 to 60 mm (see Fig. 5.5). For determination of contrast at a certain position z , the intensity $I(x, y, z)$ was calculated for values of x starting from -6 to 6 mm in steps of 10^{-2} mm. Then the extremes I_{max} and I_{min} were determined and the contrast was calculated using Eq. 6.3. For comparison, also the contrast in a system without DOE is shown in Fig. 5.5 (blue dotted line). It can be seen that the contrast in a system with DOE is (almost) independent of the distance from the cornea z , while in a system without DOE the contrast has its maximum at $z = 39$ mm and drops for larger and smaller values of z .

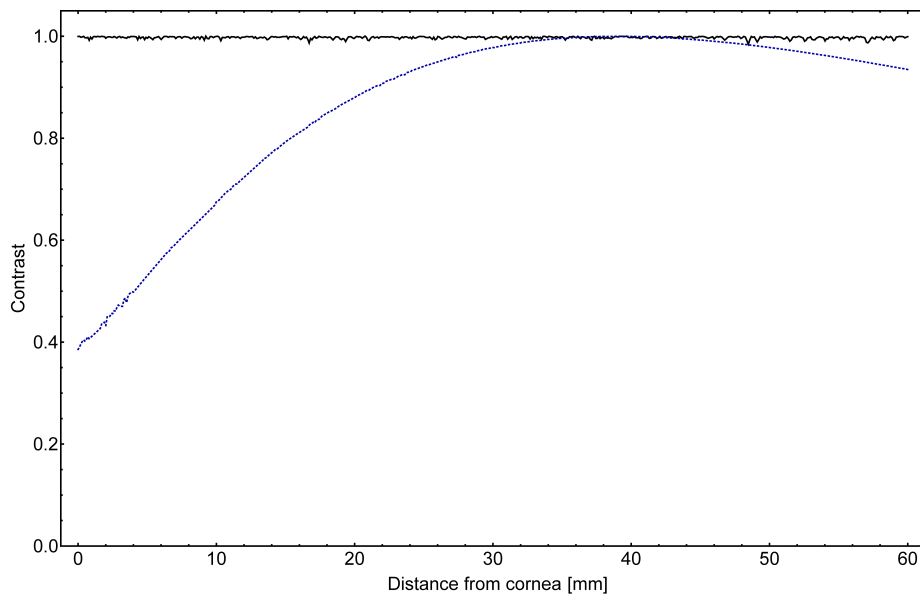


Figure 5.5: Interference contrast in a system with DOE (solid line) and without DOE (blue dotted line).

5.2.3 Fringe Spacing

To obtain the distances between adjacent fringes, first the interference pattern was calculated for a given distance from the cornea z . In a second step, the maxima of this pattern were automatically determined by a search algorithm and the differences in the positions of the maxima were calculated. The distance between the first (innermost) and the second maximum was called s_{12} , the distance between the second and the third maximum s_{23} , etc. In Fig. 5.6 the functions s_{12}, \dots, s_{45} are shown for values of z from 0 to 60 mm. For comparison, fringe

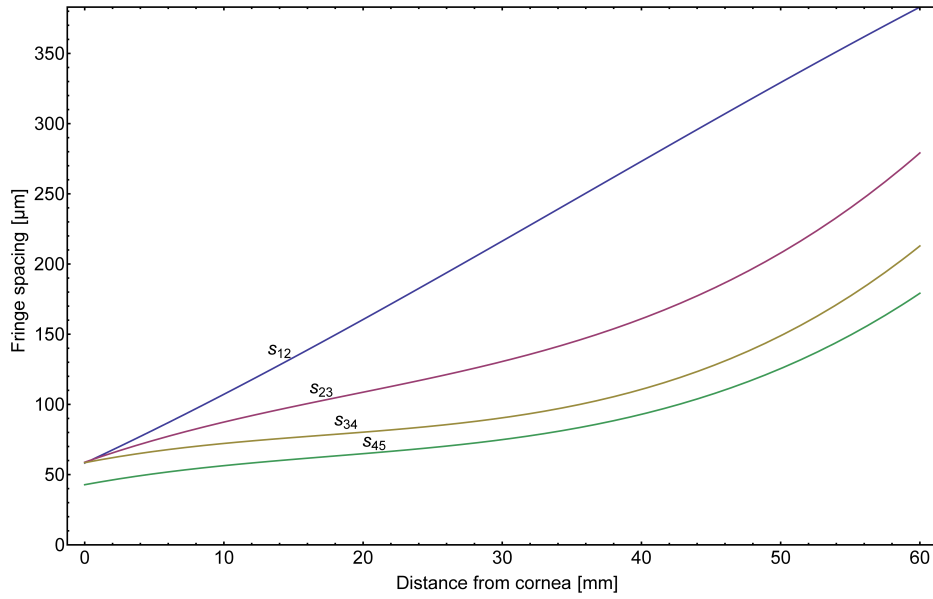


Figure 5.6: Fringe spacing in a system with DOE.

spacing in a system without DOE is shown in Fig. 5.7. In both cases, the spacing between the

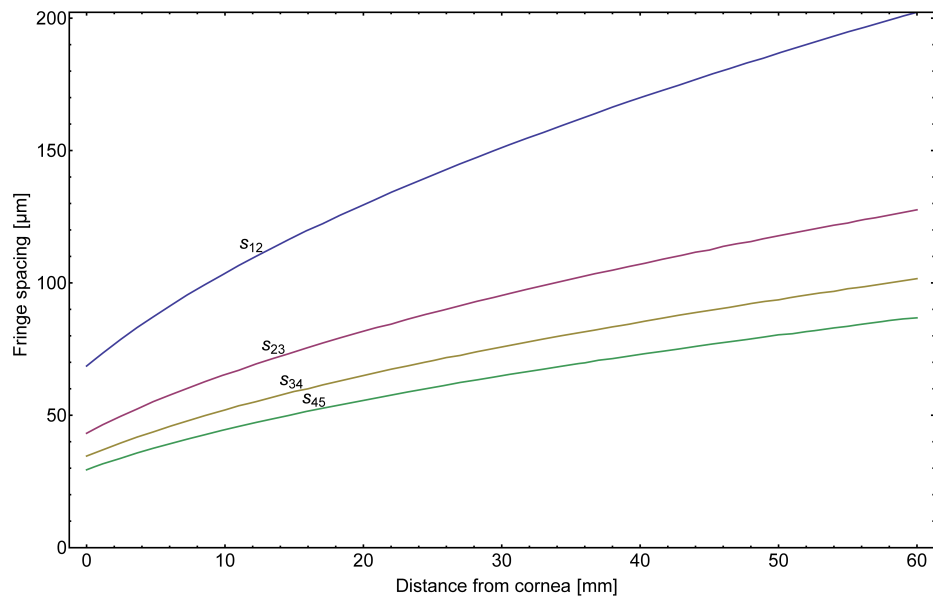


Figure 5.7: Fringe spacing in a system without DOE.

inner fringes is larger than between the outer fringes and increases with the distance from the cornea z . However, for the setup under study fringe spacing is generally larger when using a DOE.

5.3 Measurements with DOE

In the LCTI setup the DOE was mounted 40-50 mm before the cornea and length measurements were performed on a healthy subject (see Fig. 5.8). In comparison to the LCTI setup

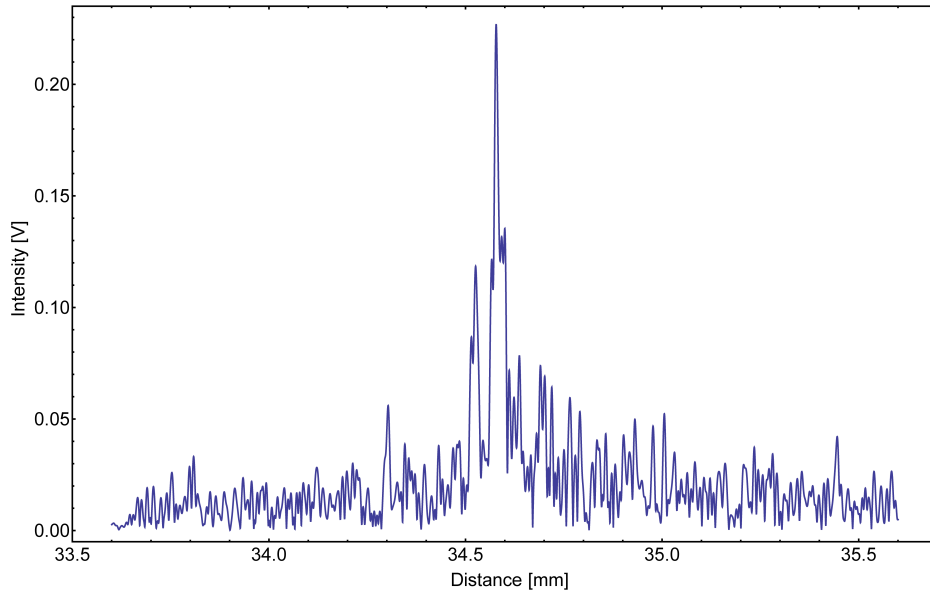


Figure 5.8: A-scan with DOE obtained from a healthy subject.

without DOE (for example see Fig. 4.4), an increase in SNR was observed. However, due to the static pattern generated by the DOE, and, furthermore, the extreme sensitivity of the system to (inevitable) lateral movements of the eye because of the focusing onto the cornea, fundus pulsations were found to be very difficult to assess. For this reason, the *in vivo* measurements presented in chapter 7 were performed without using a DOE. Instead, the SNR of the length measurement was improved by averaging ten consecutive A-scans.

Chapter 6

Fringe Contrast

In this chapter, the fringe contrast of the LCTI system (without the use of a DOE) is calculated. Also, the influence of the coherence length on the contrast of the interference pattern is investigated.

6.1 Influence of Distance from Cornea

For calculation of fringe contrast, the radius of curvature of the cornea was taken as 7.8 mm, according to Gullstrand's eye model [24]. Furthermore, the wave reflected at the anterior corneal surface was assumed to be spherical, and the wave reflected at the retina and refracted by the lens and the cornea to be plane. For the following calculation, the distance from the cornea was called d_z (where z is the optical axis) with $d_z = 0$ at the front surface of the cornea, and the distances from the optical axis in x and y directions were called d_x and d_y , respectively. Since both waves can be assumed to be linearly polarized in the same direction, the intensity I is proportional to:

$$I(d_x, d_y, d_z) \propto \left| Ae^{ikd_z} + \frac{0.0078}{r} Be^{ikr} \right|^2, \quad (6.1)$$

with

$$r(d_x, d_y, d_z) = \sqrt{d_x^2 + d_y^2 + (d_z + 0.0078)^2}, \quad \text{and} \quad k(\lambda) = \frac{2\pi}{\lambda}, \quad (6.2)$$

where $\lambda = 840 \cdot 10^{-9}$ m. For computation of contrast at a certain position d_z , the intensity was calculated at positions of d_x starting from -1 to 1 mm in steps of 10^{-3} mm, and the extremes I_{max} and I_{min} were determined. The contrast C is then calculated by:

$$C = \frac{I_{max} - I_{min}}{I_{max} + I_{min}}. \quad (6.3)$$

In Fig. 6.1, C is plotted for values of d_z from 0 to 60 mm and for values of B/A (reflection coefficient of the cornea in relation to the reflection coefficient of the retina) from 3 to 6. The maximum values of C occurred at 15.6 mm ($B/A = 3$), 23.4 mm ($B/A = 4$), 31.2 mm ($B/A = 5$), and 39.0 mm ($B/A = 6$), respectively. Experimental results show the maximum contrast between 30 to 40 mm in front of the eye [13], which suggests a ratio B/A between 5

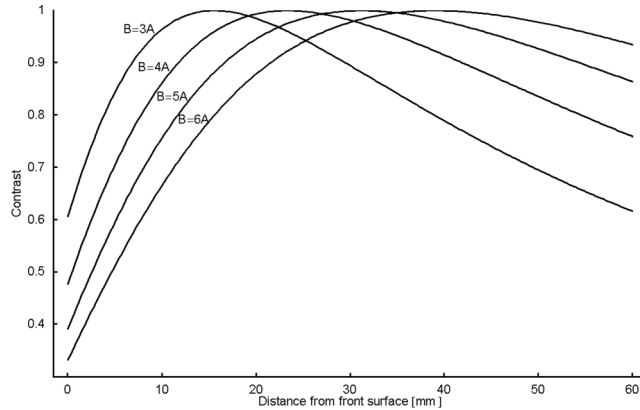


Figure 6.1: Contrast of the fringe system plotted against the distance from the front surface of the cornea and for values of B/A from 3 to 6. A and B , reflection coefficients of the retina and the cornea, respectively.

and 6. For validation of this value, B/A was calculated using the formula for the reflection coefficient $r_{reflect}$ for normal incidence:

$$r_{reflect} = \frac{n_1 - n_2}{n_1 + n_2}, \quad (6.4)$$

where n_1 and n_2 are the refractive indices of the first and second medium, respectively. The refractive index of the tear film was taken as $n_t = 1.336 - 1.357$ [25], of the vitreous as $n_v = 1.336$ [24], and of the retina as $n_r = 1.4$ [26]. Values of B/A between 6.15 and 6.48 were obtained, in good agreement with the previous calculations.

6.2 Influence of Partial Coherence

When using light of short coherence length, one has to take into account that the fringe contrast also strongly depends on the path length difference of the two reflected beams. The maximum contrast can be observed when this difference matches exactly the optical length of the eye. To study the situation of a slight mismatch in the path length, the interference pattern of an artificial eye was observed for different positions of the stepper motor. This artificial eye consisted of a lens ($f=30$ mm) representing the cornea and a Teflon disk located in the focal plane of the lens representing the retina. For this experiment, the stepper motor was positioned so that the path length difference between the two interferometer arms was 150 steps ($37.5 \mu\text{m}$) smaller than the length of the artificial eye. While observing the interference pattern and measuring the contrast, the stepper motor was moved stepwise to a path length difference $37.5 \mu\text{m}$ greater than the length of the artificial eye. The use of Eq. 6.3 for estimation of contrast would overemphasize the influence of single pixels at the two intensity extremes. Thus, in practice it is more useful to take the standard deviation of each line scan as a measure of contrast, which has the advantage of reducing the impact of the readout noise. The synthetic interferogram recorded during these measurements and the contrast curve calculated from this dataset are given in Figs. 6.2 and 6.3, respectively. As can be seen in Fig. 6.2, at closer distances of the moving reference mirror the highest intensities occur in the peripheral regions of the fringe system, while at greater distances the maximum intensities are located in the central region. An explanation for this phenomenon can be found by taking a closer look at the interference between plane and spherical wave fronts

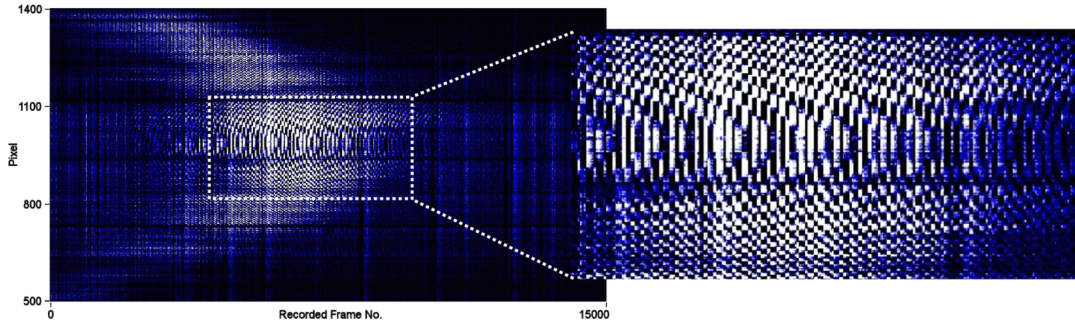


Figure 6.2: Synthetic interferogram recorded from an artificial eye while moving the measurement mirror over a range of $75 \mu\text{m}$ around the optical length of the sample.

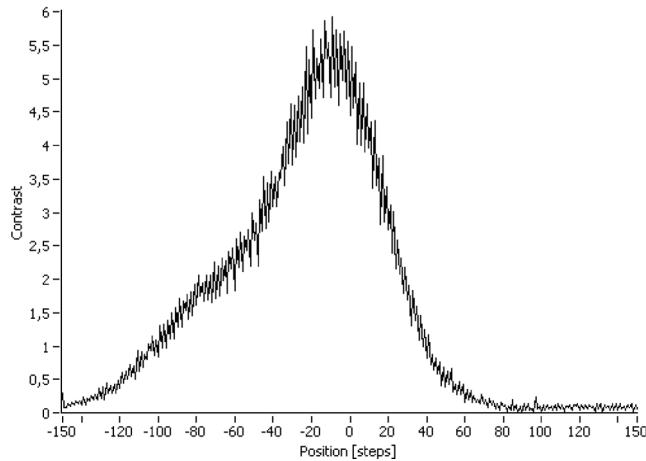


Figure 6.3: Fringe contrast of an artificial eye plotted against the position of the measurement mirror.

(Fig. 6.4). Two reflections of the incident beams generate the interference pattern: the beam coming from the moving mirror is reflected at the anterior surface of the lens representing the cornea and produces a spherical wave, while the beam coming from the fixed mirror is reflected at the Teflon disk representing the retina. The other reflections do not generate visible interference patterns, because the path length difference is not within the coherence length of the light source. If the path length difference between the two mirrors is smaller than the optical length of the eye, the corneal reflection reaches the detection plane earlier than the retinal reflection. In this case, the maximum interference contrast is observed in the outer regions of the synthetic interferogram, which becomes clear when considering that the wave fronts emitted at the same time interfere in the peripheral parts of the fringe system (Fig. 6.4(a)). As the path length difference decreases the maximum contrast is shifted toward the center of the fringe system (Fig. 6.4(b)). At smaller path length differences, interference fringes can be observed over a wide region in the synthetic interferogram including the center, leading to an increase in contrast. Pixels with constant low intensities, however, reduce the contrast as calculated from the interpixel standard deviation. Thus, the contrast curve in Fig. 6.3 is asymmetric and its maximum is shifted from the point where the two path lengths are identical by about -10 steps. When the pathway difference matches exactly the length of the eye, the maximum contrast occurs at the center of the fringe system. For obvious reasons if the distance is increased even more, the signal on the CCD is going to zero and the contrast curve drops. The distance range of the stepper motor, in which a signal can be observed in the center of the synthetic interferogram, which corresponds to the maximal observable FPA, is approximately $18 \mu\text{m}$. This range is significantly larger than typical FPA

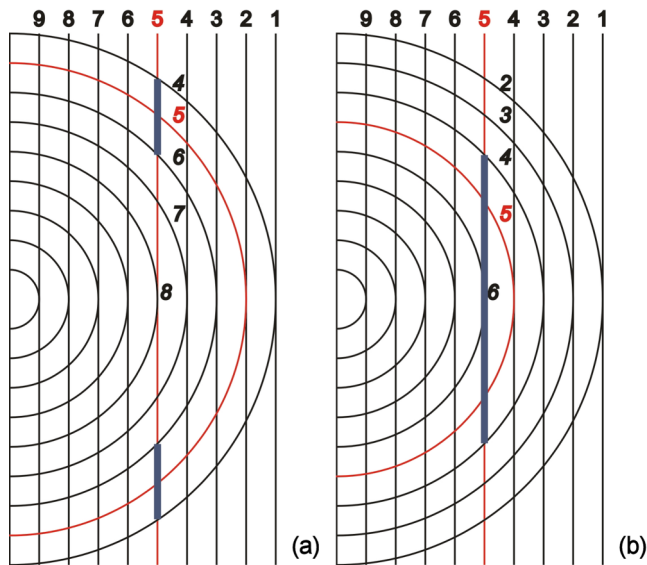


Figure 6.4: Graphical illustration of the localization of the interference contrast. See text for explanation.

values (2 to 6 μm) [5, 13].

In theory, this method would allow for quantification of the eye length, but the current acquisition time is too long for *in vivo* application. This, however, could be easily enhanced by a hardware synchronization of the CCD and the stepper motor.

Chapter 7

In vivo Measurements

7.1 Measurements at 0° and 7°

The first measurements were performed at an angle of 0° with respect to the vision axis. Two peaks, the first one at 31.20 mm (with respect to equal interferometer arm length) probably corresponding to the RPE or Bruch's membrane, the other at 31.25 mm to choroidal structures (Fig. 7.1), were chosen for measurement of fundus pulsations. These peaks were easily

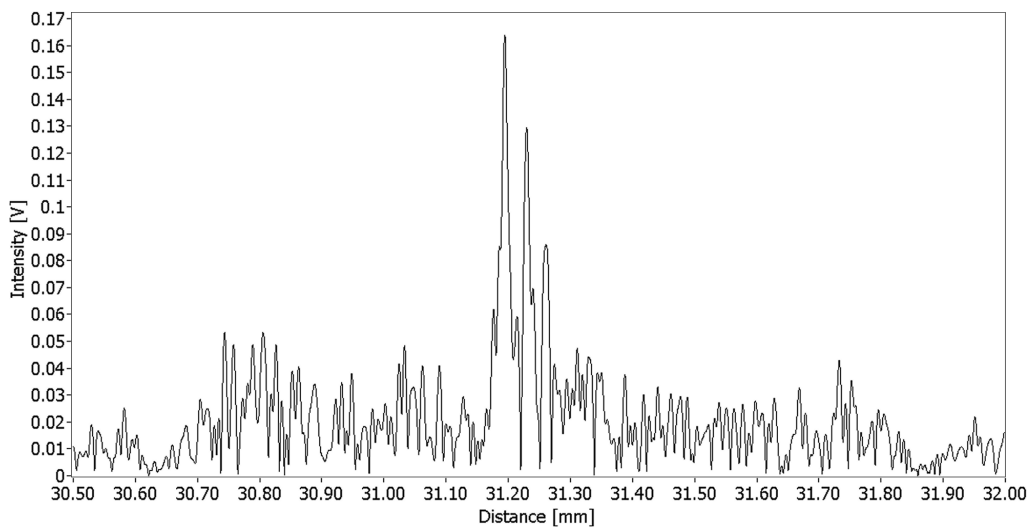


Figure 7.1: Optical A-scan of the posterior segment of a human eye recorded *in vivo* from a healthy volunteer at an angle of 0° to the vision axis. The signal peaks indicate the (optical) positions of reflecting interfaces.

reproducible in almost all length measurements, while the ILM is in most cases not observable at 0° . The synthetic interferograms were recorded at the corresponding stepper motor positions (Figs. 7.2 and 7.3) at a frequency of 600 Hz. The images representing fundus pulsation data were enhanced by the algorithms explained in chapter 8; the last thresholding step was performed without binarization. The average length of a pulse period was approximately 1.08 s, and the average fundus pulsation amplitude was $1.7 \mu\text{m}$.

Schmetterer and Wolzt have shown that the time course of the fundus pulsation is in very good agreement with the time course of the integrated velocity curve in the posterior ciliary arteries [5]. Hence, assuming a nonpulsatile venous outflow, the duration in which the distance

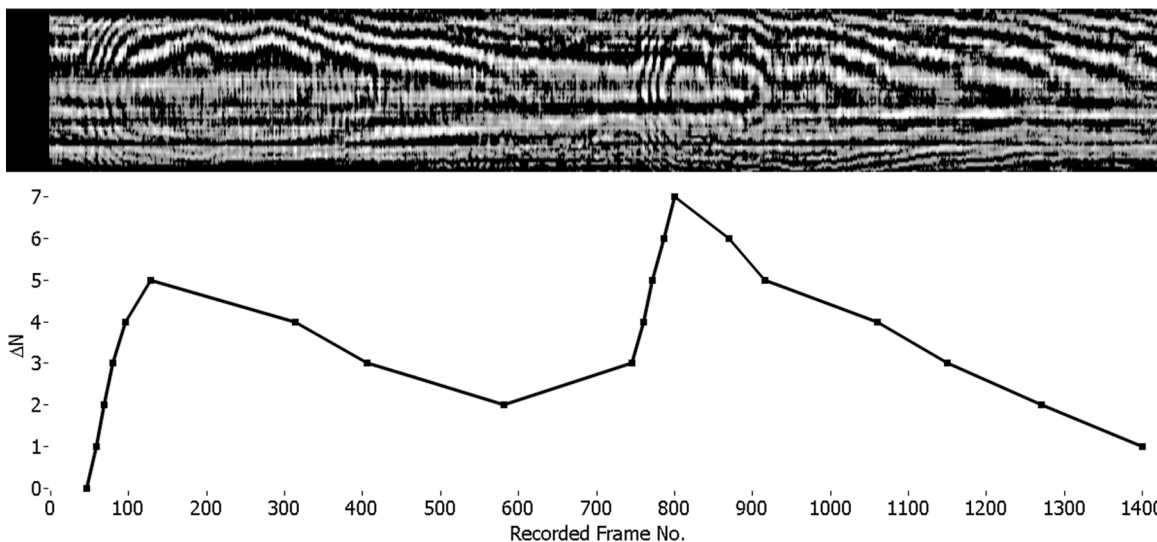


Figure 7.2: Synthetic interferogram recorded *in vivo* at a frequency of 600 Hz and at an angle of 0° to the vision axis from a healthy volunteer over two pulse periods at an axial position of 31.20 mm and contraction-dilatation graph (time course of the distance between cornea and the respective layer).

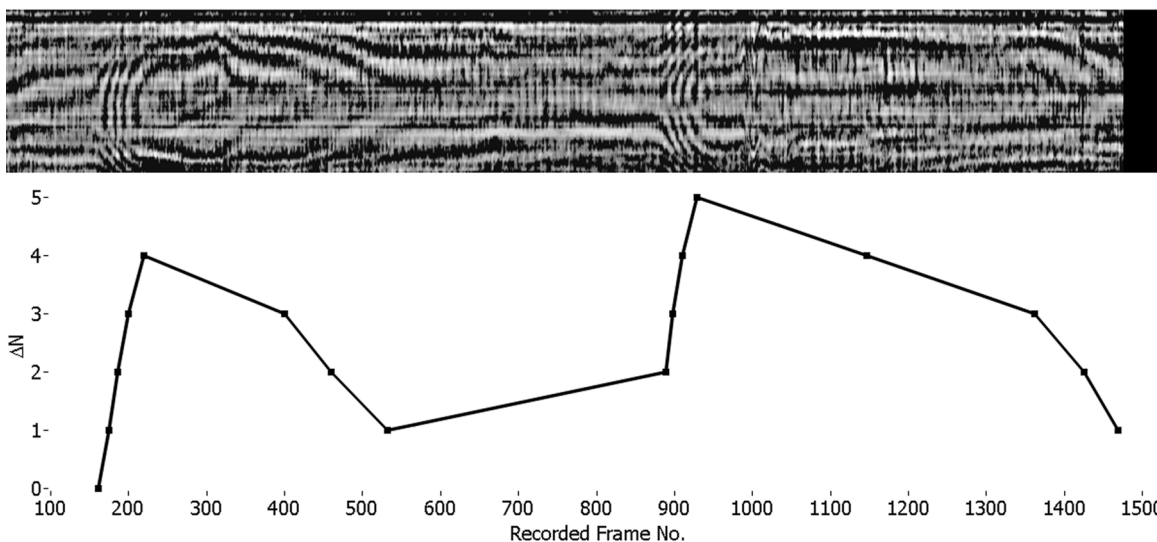


Figure 7.3: Synthetic interferogram recorded *in vivo* at a frequency of 600 Hz and at an angle of 0° to the vision axis from a healthy volunteer over two pulse periods at an axial position of 31.25 mm and contraction-dilatation graph.

between the anterior corneal surface and the posterior pole of the eye decreases corresponds to the duration of choroidal engorgement during the cardiac cycle. By averaging over the presented pulse periods, a value of 133 ms was obtained for the described process.

For the second measurements an angle of 7° nasal to the vision axis was chosen and, for better identification of retinal structures, ten consecutive A-scans were averaged (Fig. 7.4). The observed signal peaks can be assigned to the retinal layers in the following way [21]. Peak

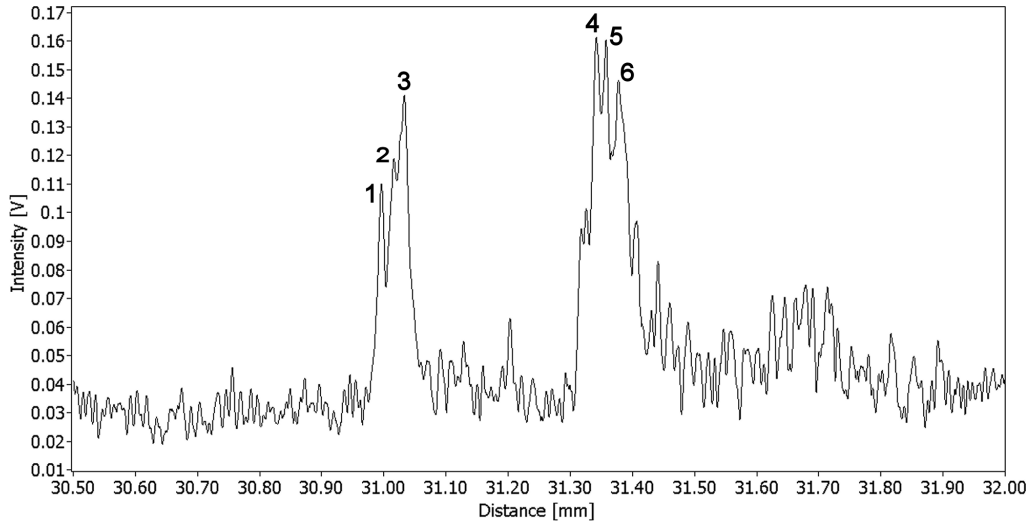


Figure 7.4: Optical A-scan of the posterior segment of a human eye recorded *in vivo* from a healthy volunteer at an angle of $\approx 7^\circ$ nasal to the vision axis. The signal peaks indicate the (optical) positions of reflecting interfaces.

1 (31.00 mm) is most probably caused by light reflected at the ILM, and peak 4 (31.34 mm) by a reflection at the RPE or Bruch’s membrane. Peak 3 can presumably be assigned to the retinal nerve fiber layer, and peaks 5 and 6 to choroidal structures. The fundus pulsation was measured at stepper motor positions corresponding to peaks 1 and 4 (Figs. 7.5 and 7.6). The average length of a pulse period was found to be 0.95 s, and the average FPA was $2 \mu\text{m}$.

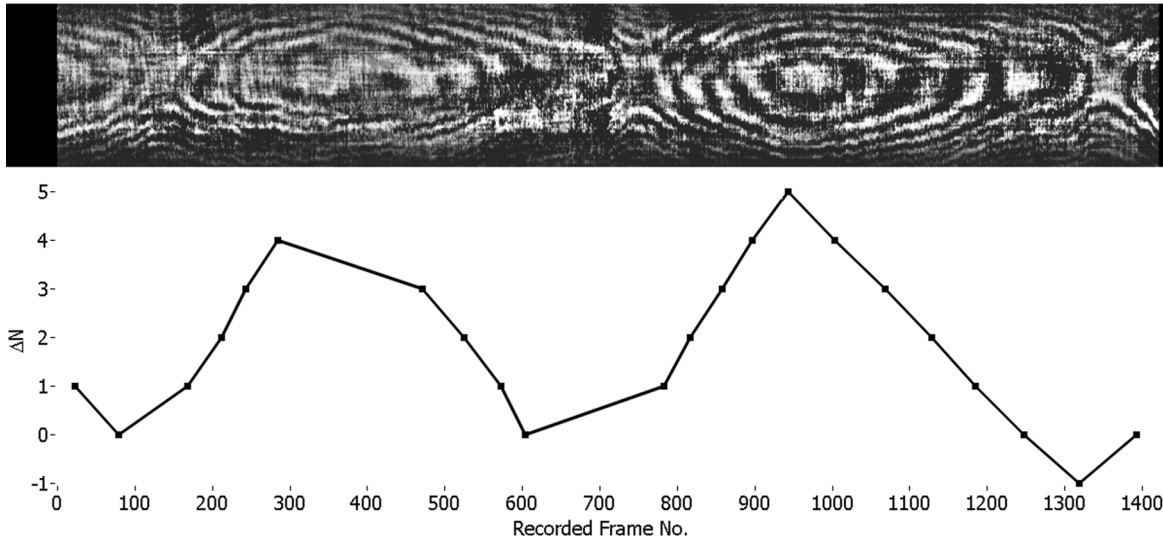


Figure 7.5: Synthetic interferogram recorded *in vivo* at a frequency of 600 Hz and at an angle of $\approx 7^\circ$ nasal to the vision axis from a healthy volunteer over two pulse periods at an axial position of 31.00 mm and contraction-dilatation graph.

The duration of choroidal engorgement was 350 ms for this subject.

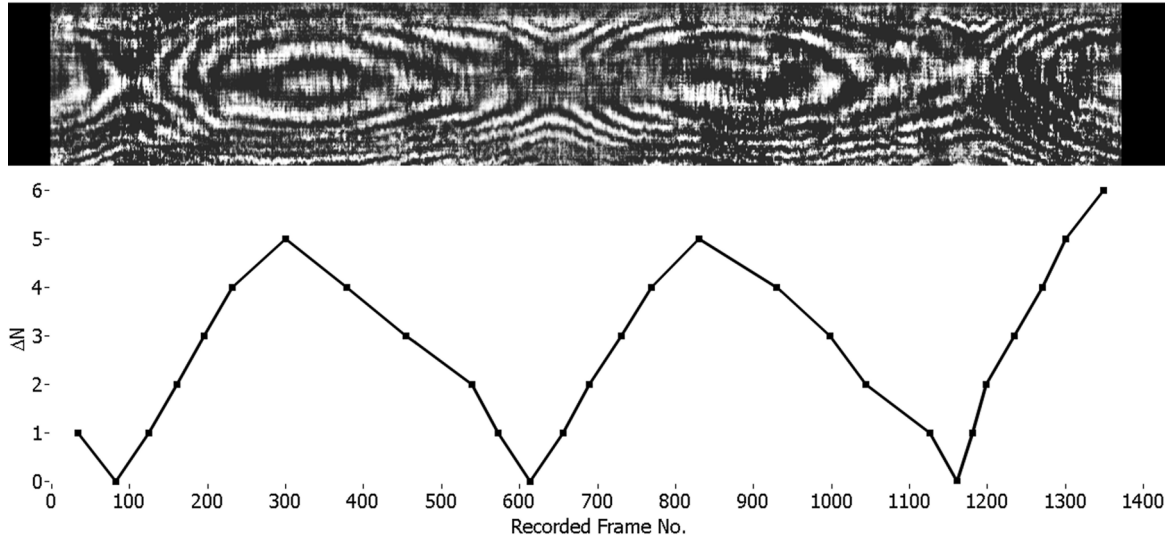


Figure 7.6: Synthetic interferogram recorded *in vivo* at a frequency of 600 Hz and at an angle of $\approx 7^\circ$ nasal to the vision axis from a healthy volunteer over two pulse periods at an axial position of 31.34 mm and contraction-dilatation graph.

Fundus pulsations occurred only at positions that were related to signal peaks in the length measurements, and disappeared when moving the stepper motor out of the coherence gate. As expected for healthy subjects, at both angles of vision only minor differences in the FPA of the (neighboring) retinal layers were found.

7.2 Measurements from -2° to 19°

Comprehensive FPA measurements were performed on a young healthy subject at horizontal angles ranging from -2° temporal to 19° nasal to the axis of vision, i.e., in a region ranging from slightly temporal of the macula to slightly nasal of the ONH. The pulse periods were found to be quite long, which can be addressed to endurance sports regularly performed by this subject.

The FPAs and the choroidal engorgement times t_1 and deflation times t_2 were calculated at each measurement site (selected peak position at a certain angle) as average over 8–10 pulse periods. Results are given in table 10.1 in the appendix. The average FPA over all measurements is $4.6 \mu\text{m}$ and the average engorgement and deflation times are 700 ms and 419 ms, respectively. The averages of the standard deviations were found to be $0.37 \mu\text{m}$ for the FPA, 91 ms for t_1 and 57 ms for t_2 . Errors in the measurement of FPA are induced by blinking or eye movements, that reduce image quality and may cause individual fringes to be missed or counted twice. t_1 and t_2 are influenced by uncertainties in the determination of the 'turning point' of the pulse amplitude, and by irregularities in the pulse length.

At angles ranging from -2° to 12° choroidal engorgement times were found to be longer than choroidal deflation times. However, in the proximity of the ONH (14° to 19°) this relation becomes inverted. The mechanism underlying this phenomenon is not fully understood. It could firstly be attributed to the difference in the vascular network in the ONH region (e.g., larger vessel diameters). Secondly, differences in the biomechanic properties of the respective tissue areas can lead to different time courses of the fundus movement. Furthermore, the observed time course could be influenced by the pathway of the probe beam, which differs

between the measurement in the macula (beam entering in the center of the cornea) and the ONH (beam entering nasal of the center, where corneal pulsations are assumed to be smaller). Corneal pulsations are generally related to total volume change, while the FPA is (approximately) a point measure of volume change at the selected measurement site. However, the behavior of the time course of the fundus movement varies between different subjects.

For better visualization, the results of the FPA measurements from -2° temporal to 19° nasal are depicted in the chart in Fig. 7.7. FPA values measured in the macula and its surroundings

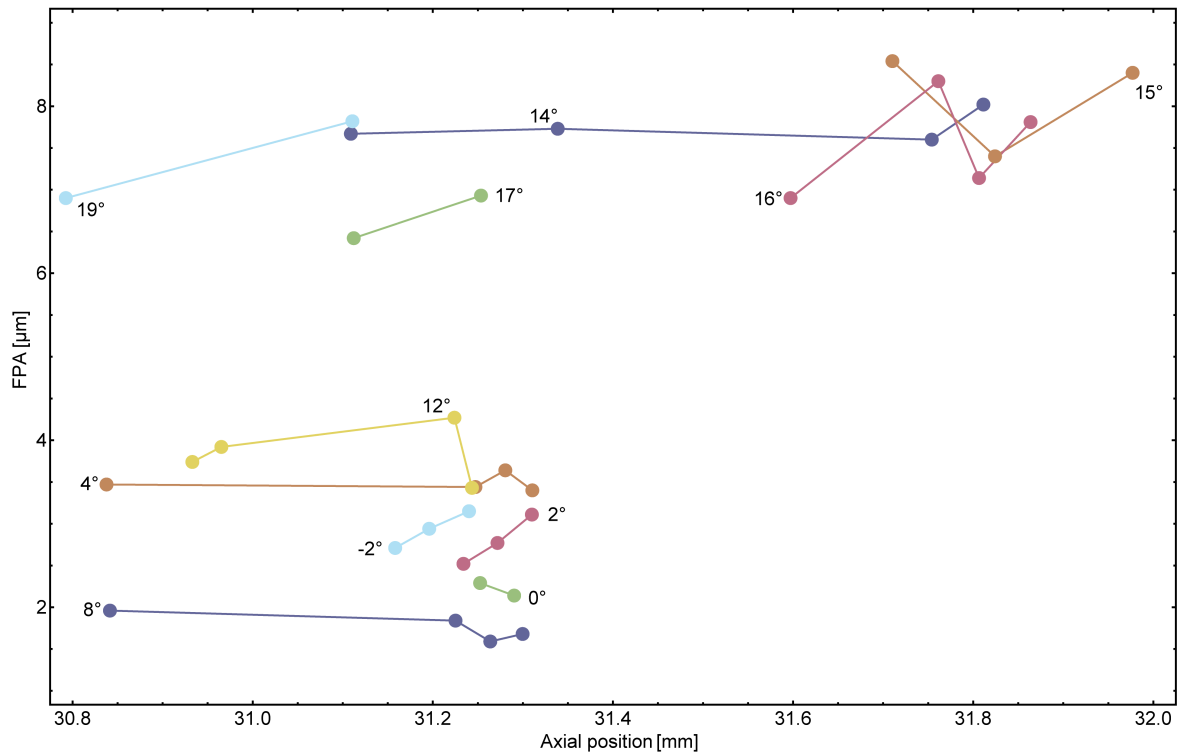


Figure 7.7: FPAs at horizontal angles ranging from -2° temporal to 19° nasal to the axis of vision obtained from a healthy young subject.

(1.59 - $4.27 \mu\text{m}$) differ significantly from those in the ONH region (6.42 - $8.54 \mu\text{m}$). Furthermore, in the proximity of the ONH (angles from 14° to 19°) the second-outermost layer exhibited smaller FPAs than the outermost layer, and at 14° to 16° the second-outermost layer had smaller FPAs than both its neighbors. In the macular region and surroundings a similar behavior was not found.

The axial peak positions observed at angles from -2° temporal to 19° nasal are shown in Fig. 7.8. The innermost layer can strongly be assumed to be the ILM. However, the assignment of other signal peaks to certain layers is difficult. The layer structure of the retina and its proximity is not continued in the ONH, where predominantly single reflective structures, but hardly any distinct layers, can be observed. This also can be seen in an FD-OCT image of the same subject (Fig. 7.9), where the positions of two measurement sites are indicated ((a) 4° and (b) 14° nasal). The respective LCTI A-scans at 4° and 14° are shown on the right hand side of Fig. 7.9. While in the proximity of the macula the retinal layers can clearly be distinguished in the FD-OCT image and the A-scan, in the optic cup only a broad hump together with some weakly backscattering structures can be observed in the A-scan. The overall structure of the FD-OCT image shown in Fig. 7.9 is, however, very similar to the results of the length measurements depicted in Fig. 7.8.

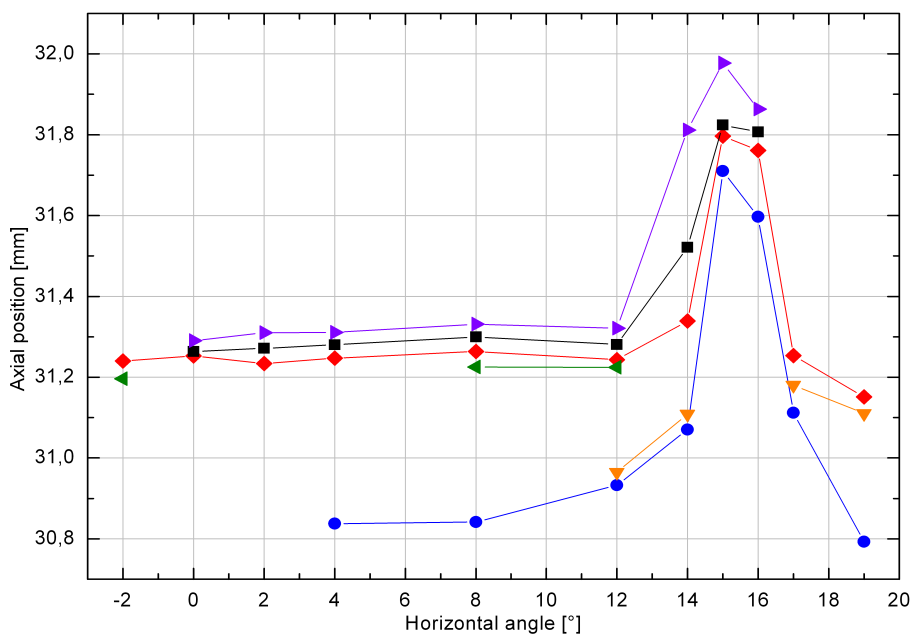


Figure 7.8: Axial peak positions at angles ranging from -2° temporal to 19° nasal to the axis of vision obtained from a healthy young subject.

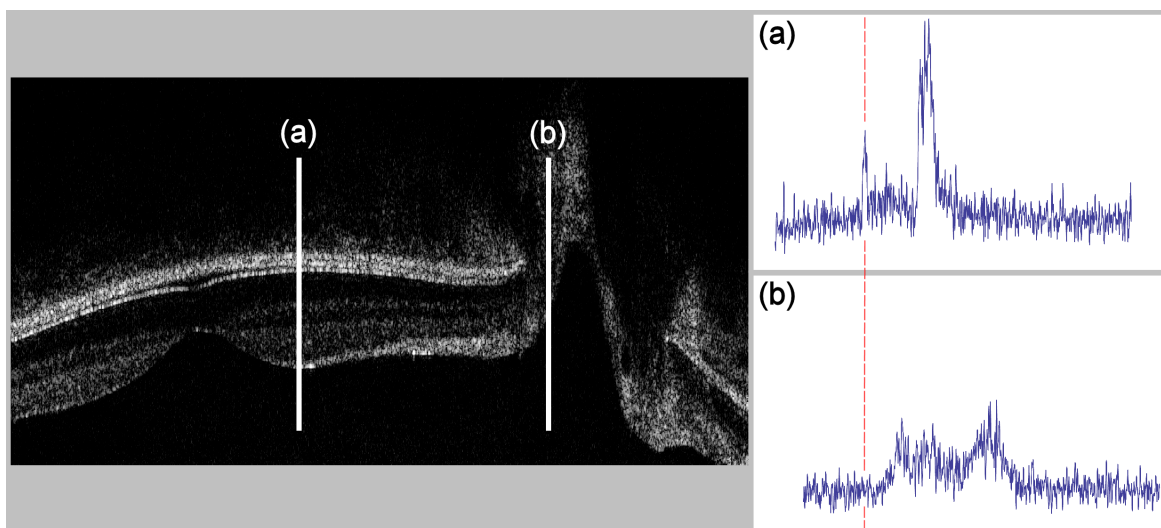


Figure 7.9: Tomogram of the subject's retina obtained by FD-OCT (left). LCTI A-scans from the same subject at positions (a) and (b) indicated by the white bars (right).

Chapter 8

Digital Image Enhancement

The algorithms used for enhancing the images recorded with LCTI and for removing local irregularities in intensity are explained in this chapter.

8.1 Introduction

In this section, the algorithms used to enhance the visual representation of the recorded synthetic interferograms are presented. The main purpose of the introduced methods is to achieve an equally distributed intensity, which allows for binarization, and thus, easier analysis of interference fringes.

8.1.1 Removal of Local Irregularities

The first step takes account of the different sensitivities of the CCD pixels as well as local irregularities of the interference patterns, which may originate from internal reflections of the system as well as static interference patterns from the subject's eye and speckle formation. Each horizontal line of the dataset (interferogram) consists of the signal recorded over time at the same pixel position. For each line, the minimum intensity value $I_{line,min}$ and the maximum intensity value $I_{line,max}$ are determined. Furthermore, the global maximum $I_{global,max}$ of the entire dataset is determined. Then, for every line the minimum is brought to 0 and the maximum to $I_{global,max}$ by applying the following formula to all data points:

$$I' = (I - I_{line,min}) \frac{I_{global,max}}{I_{line,max} - I_{line,min}}. \quad (8.1)$$

To reduce the temporal fluctuations of the signal intensity induced by movements of the patient's eye, a similar process is performed for all columns (replacing $I_{line,max}$ by $I_{col,max}$ and $I_{line,min}$ by $I_{col,min}$ in the previous formula) (see Fig. 8.1(b)).

8.1.2 Flat Fielding

The remaining inhomogeneities in the signal intensity are reduced by flat fielding [81]. This is achieved by division of the original data by a low-pass-filtered (blurred) version. The blurred

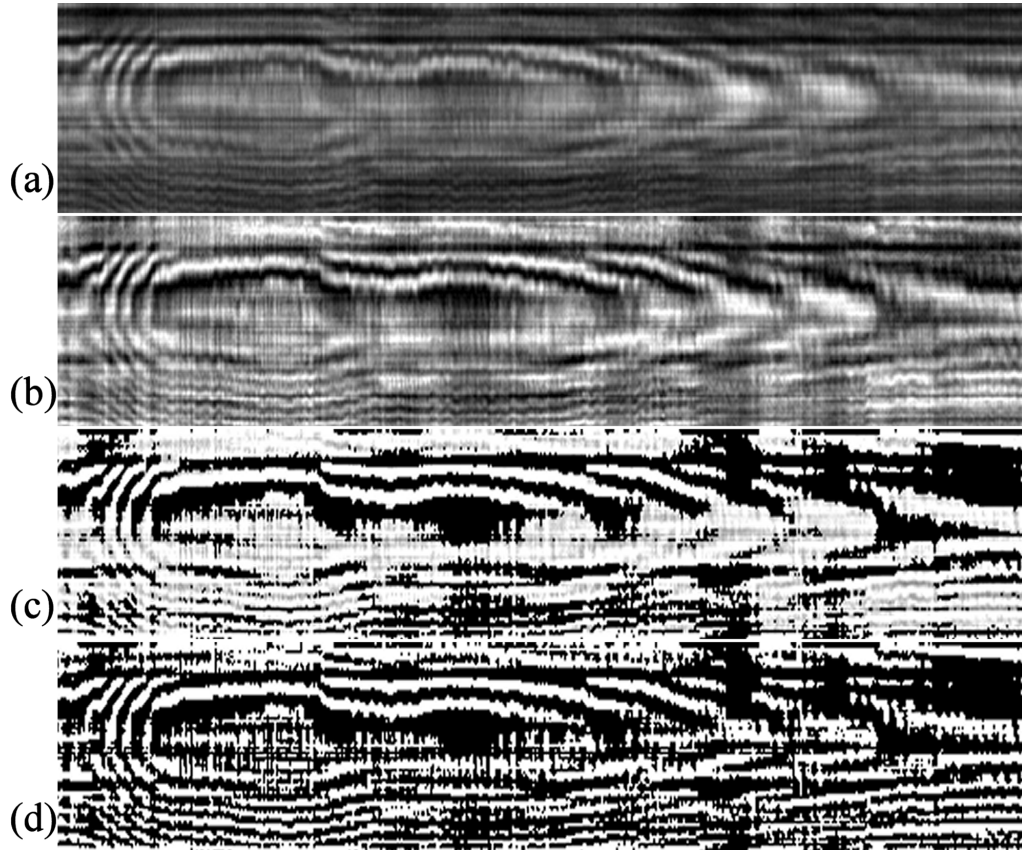


Figure 8.1: Steps of image enhancement.

image is created by convolution of the original data with an $k \times k$ kernel $(1/64[1 \dots 1]^T[1 \dots 1])$, which is equal to averaging over an 8×8 neighborhood). Before division, all data points of the original image with an intensity lower than 40 to 50 per cent of the maximum intensity are set to 0, while the values of the residual data points remain unchanged. Thus, it is avoided that low-illuminated areas of the image become overemphasized.

The result of flat fielding can be seen in Fig. 8.1(c). In the last processing step, a global threshold of 85 per cent with binarization is applied to the image (Fig. 8.1(d)).

8.2 Fast Background Subtraction for Online Inspection

The methods presented so far require a high computational effort and are, thus, only applicable to previously recorded images. However, as also described in chapter 4, a simple background subtraction can be used for the rough removal of local irregularities in the synthetic interferogram. The background intensity is calculated as moving average $MA(m)$ for each pixel position m using the recursive formula

$$MA(m) = \frac{I(m) + MA_{n-1}(m) \cdot (N - 1)}{N}, \quad (8.2)$$

where $I(m)$ is the current intensity of the respective pixel. This method requires only short computation times and leads to no delay in online inspection.

Chapter 9

Conclusion

In this work, a method called LCTI, which allows for the measurement of fundus pulsations at pre-selected layers of the ocular fundus, is presented. This is feasible as long as the distance of the respective layers can be resolved with the incorporated PCI system, and as long as the movement of the retinal layer does not largely exceed the coherence length of the light source. Using this approach, the author was able to study the relative movement between the front surface of the cornea and several pre-selected retinal layers. A series of FPA measurements was performed in several healthy subjects at different angles of vision and at different axial positions corresponding to reflecting intraocular interfaces. FPA charts were created for each subject to compare the FPAs in the neighboring retinal layers. Further measurements are required to gain insight into the movement of the various layers and to make clear if this movement is parallel. LCTI could also be used in clinical studies of ocular pathologies, e.g., in patients with macular edema, where a clear non-parallelism of the movement of the retinal layers is expected.

With some extension the applications of the LCTI system may be wide. In humans it may be difficult to measure the relative movement of the anterior surface of the cornea and the submacular sclera, because of the high blood volume within the choroid and the associated scattering and absorption. In experimental animals, however, a scleral peak can easily be observed [63]. Real-time measurement of distance changes between cornea and sclera may have two important applications. On the one hand it may be possible to measure real-time growth of axial eye length in myopia models. Although this would require quite long measurement times of several hours, such measurements seem feasible because the increase in axial eye length in one-year-old chicken is approximately $6\ \mu\text{m}$ per day [82], which should easily be detectable with the present LCTI providing a resolution of less than $0.4\ \mu\text{m}$ ($\lambda/2$).

On the other hand, LCTI may also be used to gain insight into pulsatile ocular blood flow. Schmetterer et al. have previously provided a mathematical model to relate fundus pulsation to POBF, but this model was based on conventional FPA measurements only. Nevertheless, this model showed POBF values that were close to data obtained by other techniques. Obviously, real-time measurement of corneo-scleral distance may provide a much more reliable measure to calculate ocular volume changes associated with pulsatile inflow of blood into ocular vessels.

One could argue that an FD-OCT system could be applied for the analysis of fundus pulsations, which would have the advantage of a higher sensitivity of the length measurement compared to the LCTI system and the ability of transversal scanning. However, the axial

resolution of FD-OCT systems is limited to the order of the coherence length, which is not sufficient for the (time-resolved) measurement of fundus pulsations. A phase-resolved measurement would only be possible for short time spans, since the phase information is destroyed by even very small movements of the eye. Furthermore, the phase noise would become problematic when adding up the phase information over a longer period of time. In current OCT systems, the phase difference between adjacent A-scans is utilized to gain information about the velocity of moving scatterers [54, 77]. However, due to the previously mentioned reasons it presently seems not feasible to obtain stable phase information *in vivo* over a longer time, especially when using a transversal scanner, which would make it necessary to compare the phase values of temporally separated A-scans. Furthermore, the amount of data generated by this method is too large to be recorded over a time of more than a few seconds. Recently, Singh et al. presented an approach to overcome the limited resolution of OCT by applying a Gaussian fit to the observed peaks [83]. However, eye movements remain a major problem of this setup and currently inhibit the observation of the relative movement between cornea and retina.

In conclusion the author presents a new technique capable of measuring distance changes between pre-selected ocular surfaces. Heart-rate-related distance changes between the cornea and different reflecting layers, including ILM and Bruch's membrane, are measured in healthy subjects. The applications of this technology may be, however, much wider, including the study of eye elongation in myopia models and the study of ocular blood flow by measuring pulse-related changes in ocular volume.

Appendix

Table 10.1: FPAs in the right eye of a healthy subject at angles from -2° to 19° : h angle, horizontal angle temporal (-) or nasal (+) to the vision axis; v angle, vertical angle; FPA, fundus pulsation amplitude; t_1 , duration of choroidal engorgement; t_2 , duration of choroidal deflation.

h angle [°]	v angle [°]	peak position [mm]	FPA [μm]	t_1 [ms]	t_2 [ms]
-2	0	31.1582	2.71	886	126
		31.1960	2.94	864	124
		31.2402	3.15	820	138
0	0	31.2525	2.29	838	124
		31.2903	2.14	892	116
	-2	31.1542	2.10	906	120
		31.1830	2.18	986	114
		31.2240	2.56	1012	130
	2	2	31.2265	3.70	814
31.2390			3.23	858	128
31.2840			4.01	874	176
2	0	31.2340	2.52	828	128
		31.2718	2.77	780	130
		31.3100	3.11	922	118
4	0	30.8377	3.47	847	122
		31.2473	3.44	924	116
		31.2805	3.64	890	118
		31.3105	3.40	830	116
8	0	30.8415	1.96	812	100
		31.2252	1.84	986	122
		31.2638	1.59	946	106
		31.2997	1.68	922	110
12	0	30.9330	3.74	790	438
		30.9652	3.92	976	260
		31.2240	4.27	732	486
		31.2435	3.43	774	458
14	0	31.1090	7.67	468	814
		31.3387	7.73	424	818
		31.7540	7.60	410	782
		31.8113	8.02	444	750

15	0	31.7103	8.54	446	806
		31.8242	7.40	416	740
		31.9770	8.40	440	756
16	0	31.5972	6.90	416	756
		31.7613	8.30	412	790
		31.8065	7.14	374	784
		31.8637	7.81	420	810
	8	30.8403	3.71	494	752
		31.1762	4.69	478	838
17	0	31.1122	6.42	460	928
		31.2535	6.93	318	846
19	0	30.7925	6.90	448	804
		31.1107	7.82	462	852

Publications and Conference Proceedings

1. Nikolaus Dragostinoff, René M. Werkmeister, Martin Gröschl and Leopold Schmetterer
Depth-resolved measurement of ocular fundus pulsations by low-coherence tissue interferometry
Journal of Biomedical Optics, Vol. **14**, Issue 5, pp. 054047 1–9 (September/October 2009)
2. René M. Werkmeister, Nikolaus Dragostinoff, Michael Pircher, Erich Götzinger, Christoph K. Hitzenberger, Rainer A. Leitgeb and Leopold Schmetterer
Bidirectional Doppler Fourier-domain optical coherence tomography for measurement of absolute flow velocities in human retinal vessels
Optics Letters, Volume **33**, Issue 24, pp. 2967–2969 (December 2008)
3. René M. Werkmeister, Nikolaus Dragostinoff, Michael Pircher, Erich Götzinger, Christoph K. Hitzenberger, Rainer A. Leitgeb and Leopold Schmetterer
Bidirectional Doppler Fourier-domain optical coherence tomography for measurement of absolute flow velocities in human retinal vessels
Virtual Journal for Biomedical Optics, Volume **4**, Issue 2 (February 2009)
4. René M. Werkmeister, Nikolaus Dragostinoff, Michael Pircher, Erich Götzinger, Christoph K. Hitzenberger, Rainer A. Leitgeb and Leopold Schmetterer
In vivo bi-directional Doppler Fourier-domain optical coherence tomography for measurement of absolute flow velocities
BIOS 2009, SPIE Proc. Vol. **7168-60**, San Jose, Ca (February 2009)
5. Nikolaus Dragostinoff, René M. Werkmeister and Leopold Schmetterer
Measurement of ocular fundus pulsations at pre-selected axial positions by low coherence tissue interferometry
ARVO 2010, Prog. No. **5021**, Ft. Lauderdale, Fl (May 2010)
6. René M. Werkmeister, Nikolaus Dragostinoff, Tilman Schmoll and Leopold Schmetterer
Measurement of absolute flow velocities by dual-beam bidirectional Fourier-domain optical coherence tomography
ARVO 2010, Prog. No. **5005**, Ft. Lauderdale, Fl (May 2010)

Bibliography

- [1] O. Findl, G. Rainer, S. Dallinger, G. Dorner, K. Polak, B. Kiss, M. Georgopoulos, C. Vass, and L. Schmetterer, "Assessment of optic disk blood flow in patients with open-angle glaucoma," *Am. J. Ophthalmol.* **130**, 589–596 (2000).
- [2] L. Schmetterer, A. Kruger, O. Findl, H. Breiteneder, H. G. Eichler, and M. Wolzt, "Topical fundus pulsation measurements in age-related macular degeneration," *Graefes Arch. Clin. Exp. Ophthalmol.* **236**, 160–163 (1998).
- [3] L. Schmetterer and M. Wolzt, "Ocular blood flow and associated functional deviations in diabetic retinopathy," *Diabetologia* **42**, 387–405 (1999).
- [4] K. Polak, E. Polska, A. Luksch, G. Dorner, G. Fuchsjager-Mayrl, O. Findl, H. G. Eichler, M. Wolzt, and L. Schmetterer, "Choroidal blood flow and arterial blood pressure," *Eye* **17**, 84–88 (2003).
- [5] L. Schmetterer and M. Wolzt, "Laser interferometric investigations of pulsatile choroidal blood flow: review and new results on the validity of the technique," *J. Biomed. Opt.* **3**, 246–252 (1998).
- [6] L. Schmetterer and G. Garhöfer, "How can blood flow be measured?" *Surv. Ophthalmol.* **52 Suppl 2**, S134–138 (2007).
- [7] A. Hommer, G. Fuchsjager-Mayrl, H. Resch, C. Vass, G. Garhofer, and L. Schmetterer, "Estimation of ocular rigidity based on measurement of pulse amplitude using pneumotometry and fundus pulse using laser interferometry in glaucoma," *Invest. Ophthalmol. Vis. Sci.* **49**, 4046–4050 (2008).
- [8] A. Harris, H. S. Chung, T. A. Ciulla, and L. Kagemann, "Progress in measurement of ocular blood flow and relevance to our understanding of glaucoma and age-related macular degeneration," *Prog. Retin. Eye Res.* **18**, 669–687 (1999).
- [9] C. E. Riva, S. D. Cranstoun, J. E. Grunwald, and B. L. Petrig, "Choroidal blood flow in the foveal region of the human ocular fundus," *Invest. Ophthalmol. Vis. Sci.* **35**, 4273–4281 (1994).
- [10] D. M. Silver and R. A. Farrell, "Validity of pulsatile ocular blood flow measurements," *Surv. Ophthalmol.* **38 Suppl**, S72–80 (1994).
- [11] W. E. Lieb, S. M. Cohen, D. A. Merton, J. A. Shields, D. G. Mitchell, and B. B. Goldberg, "Color Doppler imaging of the eye and orbit. Technique and normal vascular anatomy," *Arch. Ophthalmol.* **109**, 527–531 (1991).

- [12] A. F. Fercher, "In vivo measurement of fundus pulsations by laser interferometry," *IEEE J. Quantum Electron.* **20**, 1469–1471 (1984).
- [13] L. Schmetterer, F. Lexer, C. J. Unfried, H. Sattmann, and A. F. Fercher, "Topical measurement of fundus pulsations," *Opt. Eng.* **34**, 711–716 (1995).
- [14] A. Fercher, C. Hitzenberger, W. Drexler, L. Schmetterer, O. Findl, and H. Sattmann, "Optical Coherence Biometry in Ophthalmology," in *Recent Research Developments in Optics* (Research Signpost, 2002), Vol. 2, pp. 215–237.
- [15] B. Kiss, S. Dallinger, K. Polak, O. Findl, H. G. Eichler, and L. Schmetterer, "Ocular hemodynamics during isometric exercise," *Microvasc. Res.* **61**, 1–13 (2001).
- [16] L. Schmetterer, S. Dallinger, O. Findl, H. G. Eichler, and M. Wolzt, "A comparison between laser interferometric measurement of fundus pulsation and pneumotonometric measurement of pulsatile ocular blood flow. 1. Baseline considerations," *Eye* **14 (Pt 1)**, 39–45 (2000).
- [17] L. Schmetterer, S. Dallinger, O. Findl, H. G. Eichler, and M. Wolzt, "A comparison between laser interferometric measurement of fundus pulsation and pneumotonometric measurement of pulsatile ocular blood flow. 2. Effects of changes in pCO₂ and pO₂ and of isoproterenol," *Eye* **14 (Pt 1)**, 46–52 (2000).
- [18] C. K. Hitzenberger, "Optical measurement of the axial eye length by laser Doppler interferometry," *Invest. Ophthalmol. Vis. Sci.* **32**, 616–624 (1991).
- [19] C. K. Hitzenberger, "Measurement of corneal thickness by low-coherence interferometry," *Appl. Opt.* **31**, 6637–6642 (1992).
- [20] W. Drexler, C. K. Hitzenberger, H. Sattmann, and A. F. Fercher, "Measurement of the thickness of fundus layers by partial coherence tomography," *Opt. Eng.* **34**, 701–710 (1995).
- [21] C. K. Hitzenberger, W. Drexler, A. Baumgartner, F. Lexer, H. Sattmann, M. Esslinger, M. Kulhavy, and A. F. Fercher, "Optical measurement of intraocular distances: A comparison of methods," *Lasers Light Ophthalmol.* **8**, 85–95 (1997).
- [22] A. F. Fercher and E. Roth, "Ophthalmic laser interferometry," in *Proc. SPIE* **658**, 48–51 (1986).
- [23] A. F. Fercher, K. Mengedoht, and W. Werner, "Eye-length measurement by interferometry with partially coherent light," *Opt. Lett.* **13**, 186–188 (1988).
- [24] A. Gullstrand, "The dioptrics of the eye," in *Helmholtz's Treatise on Physiological Optics*, J. P. C. Southall, ed. (Optical Society of America, 1924), Vol. 1, pp. 351–352.
- [25] S. Patel, J. Marshall, and F. W. Fitzke 3rd, "Refractive index of the human corneal epithelium and stroma," *J. Refract. Surg.* **11**, 100–105 (1995).
- [26] M. G. Wirtitsch, E. Ergun, B. Hermann, A. Unterhuber, M. Stur, C. Scholda, H. Sattmann, T. H. Ko, J. G. Fujimoto, and W. Drexler, "Ultrahigh resolution optical coherence tomography in macular dystrophy," *Am. J. Ophthalmol.* **140**, 976–983 (2005).
- [27] L. Bergmann, C. Schaefer, and H. Niedrig, *Lehrbuch der Experimentalphysik, Bd.3, Optik* (Walter de Gruyter, Berlin, GER, 1993).

- [28] H. Sánchez-Tocino, A. Alvarez-Vidal, M. J. Maldonado, J. Moreno-Montañés, and A. García-Layana, “Retinal thickness study with optical coherence tomography in patients with diabetes,” *Invest. Ophthalmol. Vis. Sci.* **43**, 1588–1594 (2002).
- [29] M. Shahidi, Z. Wang, and R. Zelkha, “Quantitative thickness measurement of retinal layers imaged by optical coherence tomography,” *Am. J. Ophthalmol.* **139**, 1056–61 (2005).
- [30] K. Franze, J. Grosche, S. N. Skatchkov, S. Schinkinger, C. Foja, D. Schild, O. Uckermann, K. Travis, A. Reichenbach, and J. Guck, “Muller cells are living optical fibers in the vertebrate retina,” *Proc Natl Acad Sci USA* **104**, 8287–8292 (2007).
- [31] A. Harris, L. Kagemann, and G. A. Cioffi, “Assessment of human ocular hemodynamics,” *Surv Ophthalmol* **42**, 509–533 (1998).
- [32] S. Roh and J. J. Weiter, “Retinal and Choroidal Circulation,” in *Ophthalmology*, M. Yanoff, J. S. Duker, and J. J. Augsburger, eds. (Mosby, 2003), pp. 779–782, 2nd edn.
- [33] G. Fuchsjager-Mayrl, B. Wally, M. Georgopoulos, G. Rainer, K. Kircher, W. Buehl, T. Amoako-Mensah, H.-G. Eichler, C. Vass, and L. Schmetterer, “Ocular blood flow and systemic blood pressure in patients with primary open-angle glaucoma and ocular hypertension,” *Invest Ophthalmol Vis Sci* **45**, 834–839 (2004).
- [34] B. Pemp and L. Schmetterer, “Ocular blood flow in diabetes and age-related macular degeneration,” *Can. J. Ophthalmol.* **43**, 295–301 (2008).
- [35] B. Pemp, E. Polska, K. Karl, M. Lasta, A. Minichmayr, G. Garhofer, M. Wolzt, and L. Schmetterer, “Effects of Antioxidants (AREDS Medication) on Ocular Blood Flow and Endothelial Function in an Endotoxin-induced Model of Oxidative Stress in Humans,” *Invest. Ophthalmol. Vis. Sci.* **51**, 2–6 (2010).
- [36] E. Friedman, “A Hemodynamic Model of the Pathogenesis of Age-related Macular Degeneration,” *Am J Ophthalmol* **124**, 677–682 (1997).
- [37] E. Friedman, “The role of the Atherosclerotic Process in the Pathogenesis of Age-related Macular Degeneration,” *Am J Ophthalmol* **130**, 658–663 (2000).
- [38] E. Friedman, “Update of the Vascular Model of AMD,” *Br J Ophthalmol* **88**, 161–163 (2004).
- [39] E. Friedman, S. Krupsky, A. M. Lane, S. S. Oak, E. S. Friedman, K. Egan, and E. S. Gragoudas, “Ocular Blood flow Velocity in Age-related Macular Degeneration,” *Ophthalmology* **102**, 640–646 (1995).
- [40] M. Lorenzi, G. T. Feke, E. Cagliero, L. Pitler, D. A. Schaumberg, F. Berisha, D. M. Nathan, and J. W. McMeel, “Retinal haemodynamics in individuals with well-controlled type 1 diabetes,” *Diabetologia* **51**, 361–364 (2008).
- [41] J. E. Grunwald, J. DuPont, and C. E. Riva, “Retinal haemodynamics in patients with early diabetes mellitus,” *Br J Ophthalmol* **80**, 327–331 (1996).
- [42] L. Schmetterer, A. Salomon, A. Rheinberger, C. Unfried, F. Lexer, and M. Wolzt, “Fundus pulsation measurements in diabetic retinopathy,” *Graefes Arch Clin Exp Ophthalmol* **235**, 283–287 (1997).

- [43] O. Findl, S. Dallinger, B. Rami, K. Polak, E. Schober, A. Wedrich, E. Ries, H. G. Eichler, M. Wolzt, and L. Schmetterer, "Ocular haemodynamics and colour contrast sensitivity in patients with type 1 diabetes," *Br J Ophthalmol* **84**, 493–498 (2000).
- [44] H. R. Novotny and D. L. Alvis, "A method of photographing fluorescence in circulating blood in the human retina," *Circulation* **24**, 82–86 (1961).
- [45] R. Bonner and R. Nossal, "Principles of laser-Doppler flowmetry," in *Laser-Doppler Blood Flowmetry*, A. P. Shepherd, Jr. and P. Å. Öberg, eds. (Kluwer Academic Publishers, Boston, MA, 1990), chap. 2, pp. 17–65.
- [46] J. D. Briers and A. F. Fercher, "Retinal blood-flow visualization by means of laser speckle photography," *Invest Ophthalmol Vis Sci* **22**, 255–259 (1982).
- [47] M. E. Langham, R. A. Farrell, V. O'Brien, D. M. Silver, and P. Schilder, "Blood flow in the human eye," *Acta Ophthalmol Suppl* **191**, 9–13 (1989).
- [48] D. M. Silver, R. A. Farrell, M. E. Langham, V. O'Brien, and P. Schilder, "Estimation of pulsatile ocular blood flow from intraocular pressure," *Acta Ophthalmol Suppl* **191**, 25–29 (1989).
- [49] L. Schmetterer, M. Wolzt, A. Salomon, A. Rheinberger, C. Unfried, G. Zanaschka, and A. F. Fercher, "Effect of isoproterenol, phenylephrine, and sodium nitroprusside on fundus pulsations in healthy volunteers," *Br J Ophthalmol* **80**, 217–223 (1996).
- [50] S. Yazdanfar, A. M. Rollins, and J. A. Izatt, "In vivo imaging of human retinal flow dynamics by color Doppler optical coherence tomography," *Arch Ophthalmol* **121**, 235–239 (2003).
- [51] S. Yazdanfar, A. M. Rollins, and J. A. Izatt, "Imaging and velocimetry of the human retinal circulation with color Doppler optical coherence tomography," *Opt Lett* **25**, 1448–1450 (2000).
- [52] R. Leitgeb, L. Schmetterer, C. K. Hitzenberger, A. F. Fercher, F. Berisha, M. Wojtkowski, and T. Bajraszewski, "Real-time measurement of in vitro flow by Fourier-domain color Doppler optical coherence tomography," *Opt Lett* **29**, 171–173 (2004).
- [53] R. Leitgeb, L. Schmetterer, W. Drexler, A. Fercher, R. Zawadzki, and T. Bajraszewski, "Real-time assessment of retinal blood flow with ultrafast acquisition by color Doppler Fourier domain optical coherence tomography," *Opt Express* **11**, 3116–3121 (2003).
- [54] R. M. Werkmeister, N. Dragostinoff, M. Pircher, E. Götzinger, C. K. Hitzenberger, R. A. Leitgeb, and L. Schmetterer, "Bidirectional Doppler Fourier-domain optical coherence tomography for measurement of absolute flow velocities in human retinal vessels," *Opt. Lett.* **33**, 2967–2969 (2008).
- [55] C. E. Krakau, "Calculation of the pulsatile ocular blood flow," *Invest Ophthalmol Vis Sci* **33**, 2754–2756 (1992).
- [56] C. E. Krakau, "A model for pulsatile and steady ocular blood flow," *Graefes Arch. Clin. Exp. Ophthalmol.* **233**, 112–118 (1995).
- [57] J. S. Friedenwald, "Contribution to the theory and practice of tonometry," *Am J Ophthalmol* **20**, 985–1024 (1937).

- [58] I. A. Sigal, J. G. Flanagan, I. Tertinegg, and C. R. Ethier, "Predicted extension, compression and shearing of optic nerve head tissues," *Exp Eye Res* **85**, 312–322 (2007).
- [59] J. C. Downs, H. Yang, C. Girkin, L. Sakata, A. Bellezza, H. Thompson, and C. F. Burgoyne, "Three-dimensional histomorphometry of the normal and early glaucomatous monkey optic nerve head: neural canal and subarachnoid space architecture," *Invest Ophthalmol Vis Sci* **48**, 3195–3208 (2007).
- [60] T. A. Ciulla, A. Harris, L. Kagemann, R. P. Danis, L. M. Pratt, H. S. Chung, D. Weinberger, and H. J. Garzozzi, "Choroidal perfusion perturbations in non-neovascular age related macular degeneration," *Br J Ophthalmol* **86**, 209–213 (2002).
- [61] J. E. Grunwald, T. I. Metelitsina, J. C. Dupont, G.-S. Ying, and M. G. Maguire, "Reduced foveolar choroidal blood flow in eyes with increasing AMD severity," *Invest Ophthalmol Vis Sci* **46**, 1033–1038 (2005).
- [62] M. E. Langham, R. Grebe, S. Hopkins, S. Marcus, and M. Sebag, "Choroidal blood flow in diabetic retinopathy," *Exp Eye Res* **52**, 167–173 (1991).
- [63] G. F. Schmid, G. I. Papastergiou, D. L. Nickla, C. E. Riva, T. Lin, R. A. Stone, and A. M. Laties, "Validation of laser Doppler interferometric measurements in vivo of axial eye length and thickness of fundus layers in chicks," *Curr. Eye Res.* **15**, 691–696 (1996).
- [64] M. Born and E. Wolf, *Principles of Optics: Electromagnetic Theory of Propagation, Interference and Diffraction of Light (7th Edition)* (Cambridge University Press, Cambridge, UK, 1999).
- [65] A. F. Fercher and C. K. Hitzenberger, "Optical coherence tomography," in *Progress in Optics*, E. Wolf, ed. (Elsevier, Amsterdam, 2002), Vol. 44, chap. 4, pp. 215–302.
- [66] A. F. Fercher, C. K. Hitzenberger, and M. Juchem, "Measurement of intraocular optical distances using partially coherent laser light," *J. Mod. Opt.* **38**, 1327–1333 (1991).
- [67] A. Baumgartner, C. K. Hitzenberger, H. Sattmann, W. Drexler, and A. F. Fercher, "Signal and Resolution Enhancements in Dual Beam Optical Coherence Tomography of the Human Eye," *J. Biomed. Opt.* **3**, 45–54 (1998).
- [68] A. Baumgartner, C. K. Hitzenberger, E. Ergun, M. Stur, H. Sattmann, W. Drexler, and A. F. Fercher, "Resolution-improved dual-beam and standard optical coherence tomography: a comparison," *Graefes Arch. Clin. Exp. Ophthalmol.* **238**, 385–92 (2000).
- [69] C. K. Hitzenberger, A. Baumgartner, W. Drexler, and A. F. Fercher, "Interferometric measurement of corneal thickness with micrometer precision," *Am. J. Ophthalmol.* **118**, 468–476 (1994).
- [70] W. Drexler, A. Baumgartner, O. Findl, C. K. Hitzenberger, H. Sattmann, and A. F. Fercher, "Submicrometer precision biometry of the anterior segment of the human eye," *Invest. Ophthalmol. Vis. Sci.* **38**, 1304–1313 (1997).
- [71] W. Drexler, A. Baumgartner, O. Findl, C. K. Hitzenberger, and A. F. Fercher, "Biometric investigation of changes in the anterior eye segment during accommodation," *Vision Res.* **37**, 2789–2800 (1997).
- [72] O. Findl, W. Drexler, R. Menapace, C. K. Hitzenberger, and A. F. Fercher, "High precision biometry of pseudophakic eyes using partial coherence interferometry," *J. Cataract Refract. Surg.* **24**, 1087–1093 (1998).

- [73] C. K. Hitzenberger, W. Drexler, C. Dolezal, F. Skorpik, M. Juchem, A. F. Fercher, and H. D. Gnad, “Measurement of the axial length of cataract eyes by laser Doppler interferometry,” *Invest. Ophthalmol. Vis. Sci.* **34**, 1886–1893 (1993).
- [74] W. Drexler, O. Findl, R. Menapace, G. Rainer, C. Vass, C. K. Hitzenberger, and A. F. Fercher, “Partial coherence interferometry: a novel approach to biometry in cataract surgery,” *Am. J. Ophthalmol.* **126**, 524–534 (1998).
- [75] W. Drexler and J. G. Fujimoto, *Optical Coherence Tomography: Technology and Applications* (Springer, Berlin, GER, 2008).
- [76] C. Hitzenberger, P. Trost, P.-W. Lo, and Q. Zhou, “Three-dimensional imaging of the human retina by high-speed optical coherence tomography,” *Opt. Express* **11**, 2753–2761 (2003).
- [77] R. A. Leitgeb, L. Schmetterer, C. K. Hitzenberger, A. F. Fercher, F. Berisha, M. Wojtkowski, and T. Bajraszewski, “Real-time measurement of in vitro flow by Fourier-domain color Doppler optical coherence tomography,” *Opt. Lett.* **29**, 171–173 (2004).
- [78] M. Wojtkowski, V. Srinivasan, T. Ko, J. Fujimoto, A. Kowalczyk, and J. Duker, “Ultrahigh-resolution, high-speed, Fourier domain optical coherence tomography and methods for dispersion compensation,” *Opt. Express* **12**, 2404–2422 (2004).
- [79] N. Dragostinoff, R. M. Werkmeister, M. Gröschl, and L. Schmetterer, “Depth-resolved measurement of ocular fundus pulsations by low-coherence tissue interferometry,” *J. Biomed. Opt.* **14**, 054047 1–9 (2009).
- [80] American National Standards Institute and ANSI, American National Standard for the Safe Use of Lasers, *Safe Use of Lasers, ANSI Z136.1-2007* (Laser Institute of America, Orlando, FL, 2007).
- [81] M. Seul, L. O’Gorman, and M. J. Sammon, “Edge Enhancement and Flat Fielding,” in *Practical algorithms for image analysis* (Cambridge University Press, Cambridge, UK, 2000), chap. 3.3, pp. 75–79.
- [82] G. I. Papastergiou, G. F. Schmid, C. E. Riva, M. J. Mendel, R. A. Stone, and A. M. Latis, “Ocular axial length and choroidal thickness in newly hatched chicks and one-year-old chickens fluctuate in a diurnal pattern that is influenced by visual experience and intraocular pressure changes,” *Exp. Eye Res.* **66**, 195–205 (1998).
- [83] K. Singh, C. Dion, S. Costantino, M. Wajszilber, M. Lesk, and T. Ozaki, “Development of a novel instrument to measure the pulsatile movement of ocular tissues,” *Exp. Eye Res.* **91**, 63–68 (2010).

Abbreviations and Acronyms

AMD	age-related macular degeneration
APD	avalanche photo diode
AOM	acousto optic modulator
BSC	beam splitter cube
CCT	central corneal thickness
CDI	color Doppler imaging
DAC	data acquisition card
DBS	dichroitic beam splitter
DOE	diffractive optical element
DSPS	Doppler shift power spectrum
EDV	end diastolic velocity
ELM	external limiting membrane
FC	fundus camera
FD-OCT	Fourier domain optical coherence tomography
FFT	fast Fourier transform
FPA	fundus pulsation amplitude
FWHM	full width at half maximum
GCL	ganglion cell layer
GP	glass plate
ICG	indocyanine green
ILM	inner limiting membrane
INL	inner nuclear layer
IOP	intraocular pressure
IPL	inner plexiform layer

IS	inner segments
LCCD	linear CCD array
LCTI	low coherence tissue interferometry
LDF	laser Doppler flowmetry
LDV	laser Doppler velocimetry
LE	lens
MFV	mean flow velocity
MI	mirror
MON	video monitor
MPE	maximum permissible exposure
NTG	normal tension glaucoma
OCT	optical coherence tomography
OHT	ocular hypertension
ONH	optic nerve head
ONL	outer nuclear layer
OPL	outer plexiform layer
OS	outer segments
PA	pulse amplitude
PBSC	polarizing beam splitter cube
PC	personal computer
PCI	partial coherence interferometry
PD	photodetector
PDR	proliferative diabetic retinopathy
POAG	primary open angle glaucoma
POBF	pulsatile ocular blood flow
PSV	peak systolic velocity
RNFL	retinal nerve fiber layer
ROS	reactive oxygen species
RPE	retinal pigment epithelium
SLD	superluminescent diode
SLO	scanning laser ophthalmoscopy

- SNR** signal to noise ratio
- TD-OCT** time domain optical coherence tomography
- VC** video camera
- VEGF** vascular endothelial growth factor
- VR** video recorder

List of Figures

1.1	Interference fringes generated by reflections from cornea and retina	2
2.1	Cross section diagram of the human eye	6
2.2	Cross section diagram of the anterior segment of the human eye	6
2.3	Schematic diagram of the human eye with main retinal layers	7
2.4	Plan of retinal layers and nerve cells	7
2.5	The ophthalmic artery and its branches	9
2.6	Correlation between FPA and PA	17
2.7	Fundus pulsation amplitudes at different angles of vision	18
3.1	Interference experiment with polychromatic light	25
3.2	Intensity distribution of the Fourier components of a single wave train	30
3.3	Interferometric length measurement using a coherent light source	31
3.4	Partial coherence interferometer	32
3.5	PCI depth point-spread function and its real envelope	33
3.6	Dual beam partial coherence interferometer	34
3.7	Comparison of longitudinal and transversal scan pattern	36
3.8	Ultrahigh-resolution FD-OCT image of human macula	37
3.9	Synthetic interferogram and contraction-dilatation graph	38
3.10	Optical scheme of the pulsation interferometer	38
4.1	Optical setup of the LCTI system	41
4.2	LCTI system	42
4.3	Detection unit of the LCTI system	42
4.4	A-scan with and without digital filtering	43

5.1	Translation of a beam in ray transfer matrix analysis	46
5.2	Origin of the spherical wave \mathbf{E}_1	49
5.3	Principle of a fiber collimator	51
5.4	Interference pattern with DOE	52
5.5	Interference contrast with DOE	52
5.6	Fringe spacing with DOE	53
5.7	Fringe spacing without DOE	53
5.8	A-scan with DOE	54
6.1	Contrast of the fringe system plotted against the distance from the cornea . .	56
6.2	Synthetic interferogram recorded while moving the measurement mirror . . .	57
6.3	Fringe contrast plotted against the position of the measurement mirror . . .	57
6.4	Graphical illustration of the localization of the interference contrast	58
7.1	Optical A-scan at 0° to the axis of vision	59
7.2	Synthetic interferogram at 31.20 mm	60
7.3	Synthetic interferogram at 31.25 mm	60
7.4	Optical A-scan at $\approx 7^\circ$ nasal to the axis of vision	61
7.5	Synthetic interferogram at 31.00 mm	61
7.6	Synthetic interferogram at 31.34 mm	62
7.7	FPA's at angles ranging from -2° temporal to 19° nasal	63
7.8	Axial peak positions at angles ranging from -2° temporal to 19° nasal	64
7.9	Tomogram of the subject's retina obtained by FD-OCT	64
8.1	Steps of image enhancement	66

List of Tables

2.1	Refractive indices of transparent parts of the eye	7
4.1	Pathological effects of laser light	44
5.1	Properties of the ocular components in Gullstrand's eye model	45
5.2	Ray transfer matrices of main optical elements	47
10.1	FPA's in the right eye of a healthy subject at angles from -2° to 19°	69

Curriculum Vitæ

Nikolaus Dragostinoff

Contact

Medical University of Vienna
Center for Medical Physics and Biomedical Engineering
Währinger Strasse 13
1090 Vienna
AUSTRIA

Phone: +43 1 4277 60726
Fax: +43 1 4277 9607

nikolaus.dragostinoff@meduniwien.ac.at

Personal data

Date of birth: October 8th, 1977
Citizenship: Austria
Marital status: Single

Education

1984 – 1988 Volksschule Sta. Christiana, Vienna
Elementary school

1988 – 1996 Gymnasium des Kollegiums Kalksburg, Vienna
High school

June 14th, 1996 general qualification for university entrance, A-level equivalent

Studies

Oct. 1996 – May 2003 Vienna University of Technology
Field of study: Technical Physics

May 7th, 2003 graduation: Dipl.-Ing. (equiv. MSc) Technical Physics

since July 2004 Doctoral thesis in biomedical optics
at the Medical University of Vienna
Ph.D. studies at the Vienna University of Technology

Language Courses

Aug. 1997 four-week language course at EF International Language School
Boston, USA

July 1999 – Aug. 1999 eight-week language course at EF International Language School
Toronto, CDN

Internships

Sept. 1997 four-week summer job at Post & Telekom Austria
Vienna, Austria

Aug. 1998 four-week internship at IGM Steigerwald Strahltechnik
Puchheim, Germany

July 2000 – Aug. 2000 eight-week internship at Siemens PSE
Vienna, Austria

July 2001 – Aug. 2001 eight-week internship at Siemens PSE
Vienna, Austria

Alternative Military Service

June 2003 – May 2004 ambulance man at Samariterbund Wien
Vienna, Austria

Employment

since Sept. 2004 research associate at the Medical University of Vienna
Vienna, Austria

Memberships

2010 student member, Association for Research in Vision and
Ophthalmology (ARVO)

Additional Qualifications

computer skills

MS Windows, MS Office, LabVIEW 2009, C/C++, Visual Studio

languages

German (native speaker)

English (fluent in writing and speaking)

driving license

class B

September 2010